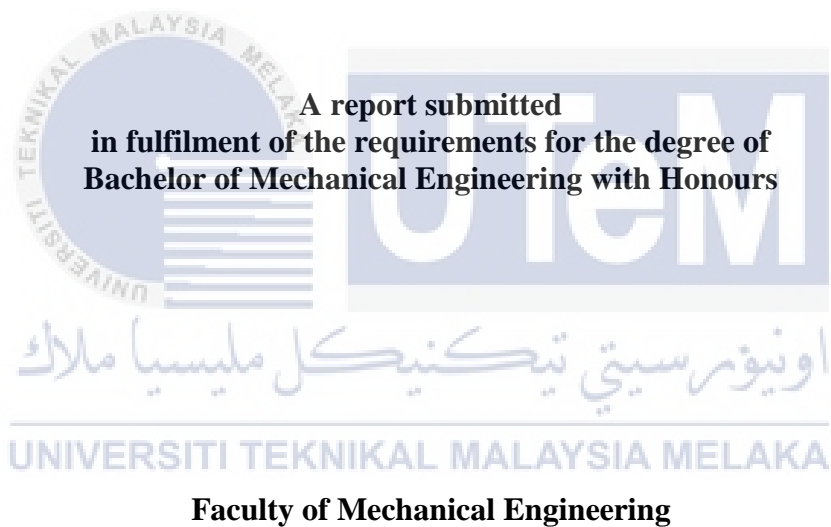


**INFLUENCE OF ROOF SHAPE ON THE NATURAL VENTILATION
POTENTIAL OF A BUILDING**

GOH-ZHONGYU



UNIVERSITI TEKNIKAL MALAYSIA MELAKA

2018

DECLARATION

I declare that this report entitled “Influence of Roof Shape on the Natural Ventilation Potential of a Building” is the result of my own research except as cited in the references. The thesis has not been accepted for any degree and is not concurrently submitted in candidature of any other degree.



Signature : _____
Name : GOH-ZHONGYU
Date : _____

اونيورسيتي تيكنيكل مليسيا ملاك

UNIVERSITI TEKNIKAL MALAYSIA MELAKA

SUPERVISOR'S DECLARATION

I hereby declare that I have read this project report and in my opinion this report is sufficient in terms of scope and quality for the award of the degree of Bachelor of Mechanical Engineering with Honours.



Signature : _____
Supervisor : DR. CHENG SEE YUAN
Date : _____

اونيورسيتي تيكنيكل مليسيا ملاك

UNIVERSITI TEKNIKAL MALAYSIA MELAKA

DEDICATION

To my beloved mother and father



ACKNOWLEDGEMENTS

The success and final outcome of this thesis was the result from a lot of guidance and assistance from many individuals and parties. I am extremely fortunate to have them all along the execution of the project work.

First and foremost, I would like to express my sincere acknowledgement to my supervisor, Dr. Cheng See Yuan from the Faculty of Mechanical Engineering, Universiti Teknikal Malaysia Melaka (UTeM) for his unparalleled teachings and support towards the completion of this thesis.

Besides, I would like to thank Dr. Fudhail Bin Abdul Munir, Computational Fluid Dynamics lecturer from the Faculty of Mechanical Engineering for his assistance in the CFD simulation works. Furthermore, I owe my profound gratitude to my peers who took interest on my project work and helped me in solving some critical CFD simulation problems.

Special thanks to my parents and sibling for their undivided moral support. Without them, this thesis would not have been possible to occur. Finally, I am thankful to all the people involved in this thesis and I am fortunate enough to get constant encouragement, support and guidance from them which helped me in successfully completing my thesis. Also, I would like to extend my sincere regards to all of them for their timely support.

ABSTRACT

The present study investigated the influence of different roof shapes on the natural ventilation potential of an isolated low-rise building by using Computational Fluid Dynamics (CFD). The Barrel Vault, Gable, Pyramid and Shed roof were chosen for the study. The Realizable $k-\varepsilon$ turbulent model was adopted in the CFD simulations. The wind which obeyed power law equation was set to approach the building model at eight different angles. The natural ventilation potential of the ground and the upper floors of the building model were studied separately with the assumption of no cross ventilation between both floors. The Shed roof shape was found out to be the highest performer in inducing natural ventilation, the Barrel Vault roof came in second, followed by the Gable roof and lastly, the Pyramid roof. It was proven that different roof shapes will have significant influence on the natural ventilation potential of a building.

ABSTRAK

Kajian ini mengkaji pengaruh bentuk bumbung yang berbeza kepada potensi pengudaraan semula jadi sesebuah bangunan dengan menggunakan Dinamik Bendalir Berkomputer. Bumbung “Barrel Vault”, “Gable”, “Pyramid” dan “Shed” telah dipilih sebagai bentuk kajian. Model bergelora “Realizable k- ϵ ” telah digunakan dalam simulasi Dinamik Bendalir Berkomputer. Angin yang berdasarkan formula “power law” telah ditetapkan untuk menuju ke bangunan modal dari lapan arah yang berbeza. Potensi pengudaraan semula jadi bagi aras bawah dan aras atas telah dikaji secara berasingan dengan andaian tiada pengudaraan salib antara kedua-dua aras. Bentuk bumbung “Shed” didapati mencapai potensi pengudaraan semula jadi yang tertinggi, bentuk bumbung “Barrel Vault” mencapai tempat kedua, diikuti bentuk bumbung “Gable” dan akhir sekali, bentuk bumbung “Pyramid”. Kajian ini telah membuktikan bahawa bentuk bumbung yang berbeza akan mempengaruhi potensi pengudaraan semula jadi sesebuah bangunan.

TABLE OF CONTENTS

	PAGE
SUPERVISOR’S DECLARATION	
TITLE	
DECLARATION	
DEDICATION	
ACKNOWLEDGEMENTS	i
ABSTRACT	ii
ABSTRAK	iii
TABLE OF CONTENTS	iv
LIST OF TABLES	viii
LIST OF FIGURES	ix
LIST OF APPENDICES	xiv
LIST OF ABBREVIATIONS	xv
LIST OF SYMBOLS	xvi
CHAPTER	
1. INTRODUCTION	1
1.1 Background	1
1.2 Problem Statement	4
1.3 Objectives	4
1.4 Scope of Project	4

2.	LITERATURE REVIEW	5
2.1	Natural Ventilation	5
2.2	Airflow	8
2.3	Airflow Pressure Distribution	9
2.4	Boundary Layer	10
2.5	Computational Fluid Dynamics	11
2.5.1	Geometry of the Building Models	11
2.5.2	Computational Domain	12
2.5.3	Meshing	12
2.5.4	Turbulent Models	13
2.5.5	Boundary Conditions	14
3.	METHODOLOGY	15
3.1	Introduction	15
3.2	Geometry of the Building Models	15
3.3	Computational Domain	18
3.4	Meshing	19
3.5	Turbulent Models	22
3.6	Boundary Conditions	22
3.7	Solution Methods and Monitors	24
3.8	Validation	25
3.8.1	Approaching Flow Vertical Wind Velocity Profile	25
	Comparison between CFD with Power Law	
	Implementation versus SFP Wind Tunnel Test	

3.8.2	Vertical Wind Velocity Profile Comparison between CFD Power Law and Non-Power Law Implementation in Different Turbulent Models versus SFP Wind Tunnel Test	27
3.9	Verification	29
3.9.1	Gird Independent Test	29
3.9.2	Turbulent Model Comparison	31
4.	RESULTS AND DISCUSSIONS	23
4.1	Wind Velocity Profile	33
4.2	Coefficient of Win Pressure Distribution around the Building Model	37
4.3	Difference in the Wind Pressure Coefficients between Opposing Facades	49
4.3.1	Difference in Wind Pressure Coefficient Data for All Roof Shapes in the Average Wind Approach Angle	51
4.3.2	Difference in Wind Pressure Coefficient Data for Barrel Vault Roof Shapes in the All Wind Approach Angles	54
4.3.3	Difference in Wind Pressure Coefficient Data for Gable Roof Shapes in the All Wind Approach Angles	56
4.3.4	Difference in Wind Pressure Coefficient Data for Pyramid Roof Shapes in the All Wind Approach Angles	58
4.3.5	Difference in Wind Pressure Coefficient Data for Shed Roof Shapes in the All Wind Approach Angles	60

5.	CONCLUSION AND RECOMMENDATION	63
5.1	Conclusion	63
5.2	Recommendations	63
	REFERENCES	64
	APPENDICES	70



LIST OF TABLES

TABLE	TITLE	PAGE
3.1	Face Sizing and Inflation Method Comparison	19
3.2	Grid Independent Test	29
3.2	Turbulent Model Comparison	32



LIST OF FIGURES

FIGURE	TITLE	PAGE
2.1	Temperature Driven Natural Ventilation (Source: Da Graca and Linden, 2016)	5
2.2	Streamlines Influenced by Roof Shape (Source: Tominaga et al, 2014)	8
2.3	Pressure Coefficient Distribution around Building Model (Source: Tominaga et al, 2014)	9
2.4	Laminar Flow (Left) and Turbulent Flow (Right) in an Enclosed Region. (Source: Ahepp, 2017)	11
2.5	Meshing for Building Model. (source: Cheng (2007))	13
2.6	Comparison of Streamwise Velocity, U_1 and Turbulent Kinetic Energy, k from Different Turbulent Model. (Source: Tominaga et al, 2014)	14
3.1	The Default 0° Wind Approach Angle Relative to the Building Model	16
3.2	The Building Model Dimensions of Barrel Vault Roof (Top Left), Gable Roof (Top Right), Pyramid Roof (Bottom Left) and Shed Roof (Bottom Right)	17
3.3	The Top View of the Building Model Facades Relative to the Wind Approach Angles	17

3.4	The Dimensions of the Computational Domain	18
3.5	Wind Velocity Profile Comparison between Different Mesh Settings and SFP Wind Tunnel Test (Tominaga et al, 2014)	20
3.6	The Computational Domain	20
3.7	The Grid Topology and Prismatic Layers	21
3.8	Power-Law Equation in UDF C Programming Code	23
3.9	The Approaching Wind Velocity Profile Comparison between CFD Simulation and SFP Wind Tunnel Test (Tominaga et al, 2014)	25
3.10	Standard k- ϵ Turbulent Model with Power Law and Non-Power Law Implementation versus SFP Wind Tunnel Test Velocity Profile	27
3.11	The Realizable k- ϵ Turbulent Model with Power Law and Non-Power Law Implementation versus SFP Wind Tunnel Test Velocity Profile	28
3.12	Pressure Difference between Windward and Leeward Building Façade versus Number of Element	30
3.13	Wind Velocity Profiles Comparison of CFD with Different Turbulent Models versus Actual Wind Tunnel Test	31
4.1	The Wind Velocity Profile of Each Roof Shapes on 0° Wind Approach Angle	35
4.2	The Wind Velocity Profile of Each Roof Shapes on 45° Wind Approach Angle	36

- 4.3 The Wind Pressure Distribution Contour around the Building 38
Model of Barrel Vault Roof (Top Left), Gable Roof (Top Right),
Pyramid Roof (Bottom Left) and Shed Roof (Bottom Right) under
0° Wind Approach Angle
- 4.4 The Wind Pressure Coefficient Distribution Contour on the North 39
Facade of Barrel Vault Roof (Top Left), Gable Roof (Top Right),
Pyramid Roof (Bottom Left) and Shed Roof (Bottom Right) under
0° Wind Approach Angle.
- 4.5 The Wind Pressure Coefficient Distribution Contour on the East 40
Facade of Barrel Vault Roof (Top Left), Gable Roof (Top Right),
Pyramid Roof (Bottom Left) and Shed Roof (Bottom Right) under
0° Wind Approach Angle.
- 4.6 The Wind Pressure Coefficient Distribution Contour on the South 41
Facade of Barrel Vault Roof (Top Left), Gable Roof (Top Right),
Pyramid Roof (Bottom Left) and Shed Roof (Bottom Right) under
0° Wind Approach Angle.
- 4.7 The Wind Pressure Coefficient Distribution Contour on the West 42
Facade of Barrel Vault Roof (Top Left), Gable Roof (Top Right),
Pyramid Roof (Bottom Left) and Shed Roof (Bottom Right) under
0° Wind Approach Angle.
- 4.8 The Wind Pressure Distribution Contour around the Building 43
Model of Barrel Vault Roof (Top Left), Gable Roof (Top Right),
Pyramid Roof (Bottom Left) and Shed Roof (Bottom Right) under
45° Wind Approach Angle

- 4.9 The Wind Pressure Coefficient Distribution Contour on the North 45
 Facade of Barrel Vault Roof (Top Left), Gable Roof (Top Right),
 Pyramid Roof (Bottom Left) and Shed Roof (Bottom Right) under
 45° Wind Approach Angle.
- 4.10 The Wind Pressure Coefficient Distribution Contour on the East 46
 Facade of Barrel Vault Roof (Top Left), Gable Roof (Top Right),
 Pyramid Roof (Bottom Left) and Shed Roof (Bottom Right) under
 45° Wind Approach Angle.
- 4.11 The Wind Pressure Coefficient Distribution Contour on the South 47
 Facade of Barrel Vault Roof (Top Left), Gable Roof (Top Right),
 Pyramid Roof (Bottom Left) and Shed Roof (Bottom Right) under
 45° Wind Approach Angle.
- 4.12 The Wind Pressure Coefficient Distribution Contour on the West 48
 Facade of Barrel Vault Roof (Top Left), Gable Roof (Top Right),
 Pyramid Roof (Bottom Left) and Shed Roof (Bottom Right) under
 45° Wind Approach Angle.
- 4.13 Difference in Wind Pressure Coefficients, C_{diff} against the 51
 Ground Floor Building Model Façades of Each Roof Shapes at the
 Average Wind Approach Angle
- 4.14 Difference in Wind Pressure Coefficients, C_{diff} against the Upper 52
 Floor Building Model Façades of Each Roof Shapes at the Average
 Wind Approach Angle.
- 4.15 Difference in Wind Pressure Coefficients, C_{diff} against All Wind 54
 Approach Angles at the Ground Floor Building Model Façades of
 the Barrel Vault Roof Shape

4.16	Difference in Wind Pressure Coefficients, C_{diff} against All Wind Approach Angles at the Upper Floor Building Model Façades of the Barrel Vault Roof Shape	55
4.17	Difference in Wind Pressure Coefficients, C_{diff} against All Wind Approach Angles at the Ground Floor Building Model Façades of the Gable Roof Shape	56
4.18	Difference in Wind Pressure Coefficients, C_{diff} against All Wind Approach Angles at the Upper Floor Building Model Façades of the Gable Roof Shape	57
4.19	Difference in Wind Pressure Coefficients, C_{diff} against All Wind Approach Angles at the Ground Floor Building Model Façades of the Pyramid Roof Shape	58
4.20	Difference in Wind Pressure Coefficients, C_{diff} against All Wind Approach Angles at the Upper Floor Building Model Façades of the Pyramid Roof Shape	59
4.21	Difference in Wind Pressure Coefficients, C_{diff} against All Wind Approach Angles at the Ground Floor Building Model Façades of the Shed Roof Shape	60
4.22	Difference in Wind Pressure Coefficients, C_{diff} against All Wind Approach Angles at the Upper Floor Building Model Façades of the Shed Roof Shape	61

LIST OF APPENDICES

APPENDIX	TITLE	PAGE
A	PSM Gantt Chart	58
B	Methodology Flowchart	60
C	Wind Velocity Profile	61
D	Difference in Coefficient of Wind Pressure	67



LIST OF ABBREVIATIONS

ANSI	American National Standards Institute
ASHRAE	American Society of Heating, Refrigerating and Air-Conditioning Engineers
CFD	Computational Fluid Dynamics
IAQ	Indoor Air Quality
RAM	Random Access Memory
RNG	Re-Normalisation Group
SBS	Sick Building Syndrome
SFP	Split Fibre Probe
SST	Shear Stress Transport
UDF	User-Defined Function

UNIVERSITI TEKNIKAL MALAYSIA MELAKA

LIST OF SYMBOLS

Q_{buoyancy}	=	Buoyancy ventilation rate
C_d	=	Discharge coefficient
A	=	Cross sectional area of the inlet that equals to the outlet
g	=	The acceleration due to gravity
h	=	Vertical distance between inlet and outlet midpoints
T_i	=	Average temperature of indoor air
T_o	=	Average temperature of outdoor air
$Q_{\text{ventilation}}$	=	wind driven ventilation rate
U_{wind}	=	wind speed at far-field
C_{p1}	=	coefficient of wind pressure drag at the upstream opening
C_{p2}	=	coefficient of wind pressure drag at the upstream opening
A_1	=	cross sectional area of the inlet
A_2	=	cross sectional area of the outlet
C_1	=	discharge coefficient at the inlet
C_2	=	discharge coefficient at the outlet
ΔP	=	Pressure drop across the openings
ρ	=	Air density
P	=	Pressure measured on the building surface
C_p	=	Pressure coefficient
U	=	Air velocity

Re	=	Reynolds number
u	=	Fluid velocity
L	=	Characteristic linear dimension
μ	=	Dynamic viscosity of the fluid
ν	=	Kinematic viscosity of the fluid
H_e	=	Building height
Hz	=	Hertz
k	=	Turbulent kinetic energy
ε	=	Epsilon
ω	=	Omega
U_1	=	Streamwise velocity
U_{H_e}	=	Air velocity at building height
W	=	Building width
k_s	=	Roughness height
C_s	=	Roughness constant
Z_0	=	Aerodynamic roughness length of the topography
$^\circ$	=	Degree
x/H_e	=	Ratio of unit length in x-axis against height of the building model
C_{diff}	=	Difference in Coefficient of Wind Pressure

CHAPTER 1

INTRODUCTION

1.1 BACKGROUND

Ventilation is a process of air circulation or exchange of air into and out of a space. In a tropical country like Malaysia, ventilation plays an important role in good indoor air quality (IAQ) of a building. Adequate air ventilation provide thermal comfort in a building and at the same time reduce the possibility of Sick Building Syndrome (SBS) among the residents (Norhidayah et al, 2013). According to an estimation by Spiru and Simona (2017), people in urban areas tend to spend up to 90% of their time in indoor environments especially work place. Hence, ventilation is crucial to ensure human wellbeing in a building.

There are essentially two types of ventilation: natural ventilation and mechanical ventilation. Natural ventilation usually involves wind while mechanical ventilation involves machines like fans and air conditioners. Mechanical ventilation systems force the air moves in the designated motion to provide ventilation or manipulating the temperature of air by certain degree. On the other hand, formation of natural ventilation relies heavily on air velocity and air flow pressure difference (Burnett et al, 2005). For cases where only insignificant indoor and outdoor temperature difference occur, air flow pressure difference determines the performance of natural ventilation (Cheng, 2007). As one of the aspects of building design, roof shape can create air flow pressure difference and thus affecting natural ventilation potential.

Despite the convenience of mechanical ventilation system functions, it occupies more than half of the annual energy consumption in a building at a rate of 100kWh per square meter of floor space (Bastide, 2006). Over reliance on mechanical ventilation on a global scale will cause enormous amount of burden towards the environment and energy suppliers (Omrani et al, 2017). According to Schulze and Eicker (2013), several studies showed natural ventilation was able to save 17% of energy consumption by mechanical ventilation in a targeted building at Meiji University, Tokyo.

Studies done by Kubota and Ahmad (2006) shows that application of natural ventilation could build up thermal comfort in tropical climate conditions while improving indoor air quality as it removes hot polluted air in a building. Natural ventilation approach on a building design proved to be a cost and operation effective solution for higher indoor environment comfort (Lei et al, 2017). The advantages of natural ventilation has grabbed attention of architects as the future of building design is more aggressive on environmental friendly and energy saving approach.

Estate developers tend to focus more on aesthetic rather than functionality in their housing design to attract buyers. Usually, the natural ventilation potential of a building is not in the primary consideration of the buyers as they unknowingly compromise by utilizing mechanical ventilation systems that are widely available in the market. This behaviour may lead to unbalanced approach on both aesthetic and functionality aspects during building design process which directly interrupts the air flow pressure difference around the building.

One of main factors found affecting the natural ventilation performance of a building in a study did by Aynsley (2007) was the building shape. The roof design has huge influence on air flow patterns around the building (Peren et al, 2015). Therefore, the intent of the project was to study the influence of roof shape on the natural ventilation potential on a building. The validation and verification of computational fluid dynamics (CFD) application were done by referring to a closely related work of Tominaga et al (2015). A few common roof shapes on typical low rise building were chosen as the target of investigation. Several vital parameters such as distribution of air pressure difference and air velocity on different roof shape designs were examined. The simulations were done on CFD capable software and data were extracted for further analysis on natural ventilation potential.



1.2 PROBLEM STATEMENT

It is well known that different bluff body shapes will create different flow properties around them. Considering that different roof shapes resemble bluff bodies of various forms, thus it would be interesting to examine how they affect the airflow and pressure distribution around buildings under a fixed flow condition. Understanding their influence could lead to a better building shape design in regard to the natural cross flow ventilation potential.

1.3 OBJECTIVES

The purposes of this project are:

1. To identify four common roof shapes and environmental conditions of a low rise building.
2. To perform Computational Fluid Dynamics (CFD) simulation on different roof shapes and wind approach angles for air pressure distribution and velocity data collection.
3. To provide an analysis on influence of roof shape on natural ventilation potential of a building.

1.4 SCOPE OF PROJECT

In this research project, the main focus is analysing the influence of roof shape on the natural ventilation potential of a building. Four common types of roof shape in Malaysia are selected for analysis. This project uses a two floors building as the testbed for different roof shape. The parameters for natural ventilation potential focuses on the difference in the coefficients of wind pressure between two opposing facades. The weather conditions are not included in this research.

CHAPTER 2

LITERATURE REVIEW

This chapter introduces the theories and scientific knowledge related to this research topic. Previous works related to the interest of this research were reviewed to obtain ideas and references for current work.

2.1 NATURAL VENTILATION

Natural ventilation is the flow of air into and out of a building due to pressure difference created by natural forces. There are two types of driving force for natural ventilation: wind and buoyancy (Da Graca and Linden, 2016). Buoyancy driven or in other words, stack driven natural ventilation is due to the temperature difference between different spaces within a building. Hot air tends to rise towards the upper part of the occupied space while cooler air stays below it. The hot air escapes from openings above and the cavity created is replaced by introduction of refresh cold air from inlet below. This natural phenomena creates an air flow within the space which it is called as ventilation and illustrated in Figure 2.1 below.

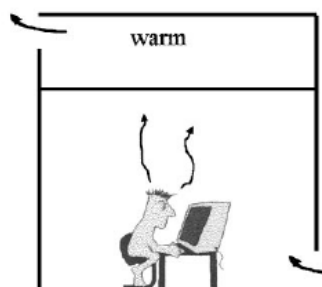


Figure 2.1: Temperature Driven Natural Ventilation (Source: Da Graca and Linden, 2016)

According to Walker (2016), the airflow caused by buoyancy effect is expressed as below:

$$Q_{\text{buoyancy}} = C_d \times A \times \sqrt{\frac{2gh(T_i - T_o)}{T_i}}$$

Where:

Q_{buoyancy} = buoyancy ventilation rate. (m^3/s)

C_d = discharge coefficient.

A = cross sectional area of the inlet that equals to the outlet. (m^2)

g = acceleration due to the gravity. (m/s^2)

h = vertical distance between inlet and outlet midpoints (m)

T_i = average temperature of indoor air (K).

T_o = average temperature of outdoor air (K)

The calculated result is the total volume of ventilation rate formed by the temperature buoyancy force. It indicates how much air is getting in and out of the building by this effect. However, buoyancy driven natural ventilation is not in the scope of this project except for wind driven natural ventilation.

On the other hand, wind driven natural ventilation is an air flow through a building due to the differential pressure between windward side and leeward side of the building. The exterior form of the building plays a more important role to create the pressure differences compared to the wind speed. By referring to Linden (1999), the airflow caused by wind is expressed as below:

$$Q_{\text{ventilation}} = U_{\text{wind}} \sqrt{\frac{C_{p1} - C_{p2}}{\frac{1}{A_1^2 \cdot C_1^2} + \frac{1}{A_2^2 \cdot C_2^2}}}$$

Where:

$Q_{\text{ventilation}}$	= wind driven ventilation rate (m^3/s)
U_{wind}	= wind speed at far-field (m/s)
C_{p1}	= coefficient of wind pressure drag at the upstream opening
C_{p2}	= coefficient of wind pressure drag at the upstream opening
A_1	= cross sectional area of the inlet (m^2)
A_2	= cross sectional area of the outlet (m^2)
C_1	= discharge coefficient at the inlet
C_2	= discharge coefficient at the outlet

$Q_{\text{ventilation}}$ represents the ventilation rate by wind for a building target. Discharge coefficient indicates the ratio of actual versus ideal mass flow rate of air at the discharge end of nozzle, or at this case, the openings.

The obtained ventilation rates could be compared with ASHRAE Standard 62.1. ASHRAE stands for American Society of Heating, Refrigerating and Air-Conditioning Engineers which focuses on indoor air quality, building managing systems, refrigeration system, efficiency and sustainability of the system. From ANSI/ASHRAE (2013), it categorises the air quality from Air Class 1 to 3 based on several key indicators like Occupancy Category (based on function of the space), Area Outdoor Air Rate, Human Outdoor Air Rate, Combined Outdoor Air Rate and Occupant Density. ANSI/ASHRAE Standard 62.1-2016 designates the minimum required ventilation rates for a building in order to provide an acceptable indoor air quality for its occupants (ASHRAE, 2016).

From the previous work of Afshin et al (2016), pressure coefficient were used to evaluate airflow rate and turbulence intensity which in turn represents natural ventilation performance of a building. Cheng (2007) studied the cross-ventilation of a building model by monitoring the wind pressure difference, ΔP in CFD simulations.

2.2 AIRFLOW

Air flow is the movement of air around a space which created by the differential in air pressure. Air usually flows from high pressure region to low pressure region. The degree of pressure differential determines the rate of air flow (Briney, 2017). The air flow is expressed by volume, cubic meter per second (m^3/s) or by mass, kilogram per second (kg/s). Previous simulation by Tominaga et al (2015) showed that comparison of streamwise velocity, U_1 across different roof pitches could induce different flow patterns around the building model. Studies done by Afshin et al (2016) indicated that different wind approach angles and wind speeds had effect on air flow rate around the building. Wind angle from 0° to 90° influenced an air flow rate difference as huge as $0.0032 \text{ m}^3/\text{s}$ on the windward and leeward side of the building model. The airflow patterns simulated by Tominaga et al (2015) is shown in Figure 2.2.

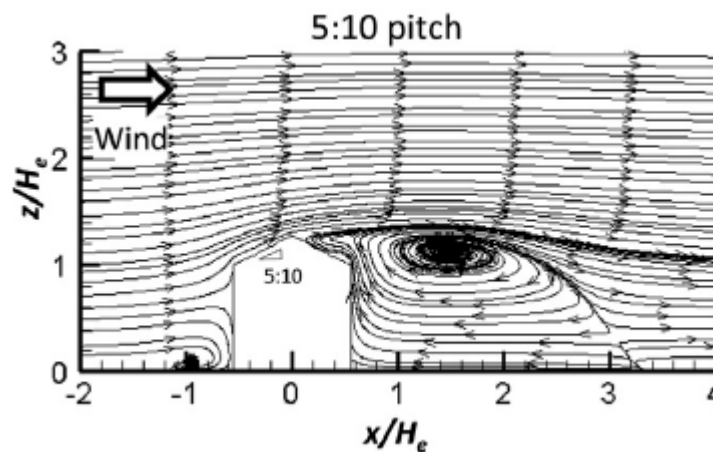


Figure 2.2: Streamlines Influenced by Roof Shape (Source: Tominaga et al, 2014)

2.3 AIRFLOW PRESSURE DISTRIBUTION

Air pressure of a specific space is the force exerted in every directions by the weight of the air above it (Tiwari, n.d.). The weight of the air in the given place within the atmosphere of Earth is called atmospheric pressure and usually expressed in the units of Pascals (Iasfunda, 2017). The airflow pressure distribution on the model surface can be represented by pressure coefficient, C_p (Reis et al, 2015). Based on Chu et al (2017), the pressure coefficient is the difference between pressure of the airflow and pressure on the external wall. Figure 2.3 shows pressure coefficient distribution around the building model by Tominaga et al (2015). From the previous work of Linden (1999), pressure measurements can be taken all over the surface of the building with pressure coefficient, C_p expressed in the formula below:

$$P = \frac{1}{2} \rho C_p U^2$$

Where:

P = pressure measured on the building surface

ρ = air density

C_p = pressure coefficient

U = air velocity

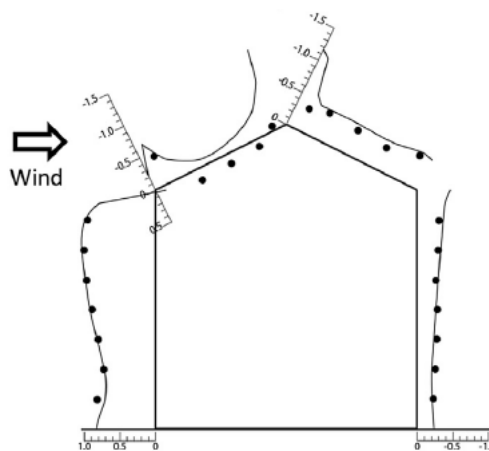


Figure 2.3: Pressure Coefficient Distribution around Building Model

(Source: Tominaga et al, 2014)

2.4 BOUNDARY LAYER

As a fluid flows through an object, the fluid close to the object is disturbed. This is the region where air velocity increases from zero to its maximum and according to Woodford (2017), it is called as boundary layer. In this project, boundary layer forms around the exterior surface of the house and surroundings when air flows through them. When the air flows over the contact surfaces, the closest air molecules attach to the surface and slow down the molecules above them (Nancy, 2015). It causes changes in velocity of airflow relative to the distance from the surface. The further away from the surface, the higher possibility for the air to maintain its maximum velocity.

The boundary layer conditions are able to be estimated by using Reynolds Number. Reynolds Number is the ratio of inertia forces versus the viscous forces of the fluid (Benson, 2009). It is a dimensionless parameter derived from Navier-Stokes equation. Reynolds Numbers is expressed as shown in equation below:

$$Re = \frac{\rho u L}{\mu} = \frac{u L}{\nu}$$

Where:

Re = Reynolds Number

ρ = fluid density (kg/m³)

u = fluid velocity (m/s)

L = characteristic linear dimension (m)

μ = dynamic viscosity of the fluid (kg/m·s)

ν = kinematic viscosity of the fluid (m²/s)

There are two types of fluid flow conditions in the boundary layer: laminar and turbulence (Lucas, 2014). Laminar flow is where the fluid particles move in parallel to each

other and the boundary walls without interfering each other's path while turbulent flow is contrast of laminar flow as shown in Figure 2.4 (Ahepp, 2017). According to Trinh (2010), laminar flow has a Reynolds Number of less than 2100 and turbulent flow starts from Reynolds Number of 4000 onwards while the region between 2100 and 4000 is the transition region (Bengtson and Stonecypher, 2010).

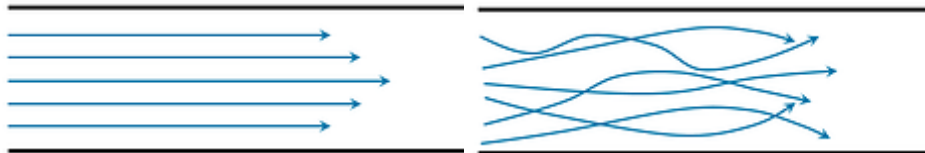


Figure 2.4: Laminar Flow (Left) and Turbulent Flow (Right) in an Enclosed Region.

(Source: Ahepp, 2017)

2.5 COMPUTATIONAL FLUID DYNAMICS

Computational Fluid Dynamics (CFD) is the prediction of flow features by computer algorithms based on a set of equations or simplified as solving the fluid dynamics problems by computer (Ramakrishna, 2011).

2.5.1 Geometry of the Building Models

The building model dimensions in Tominaga et al (2015) were inspired by the traditional Japanese architecture. The model, same as simulation model by Kralik, Konecna and Lavrincikova (2017) belonged to a low rise building type. From the previous work of Tominaga et al (2015), three different roof pitches were simulated to analyse the airflow around the gable-roof building model. On the other hand, research by Peren et al (2015) studied the cross-ventilation of a building by comparing four different roof geometry: straight, convex, concave and hybrid. The difference in roof geometry had a significant impact on the air velocity and pressure distribution around the building based on the observation of simulation result.

2.5.2 Computational Domain

According to Versteeg and Malalasekera (1995), computational domain is ought to cover adequate region around the building model to avoid distortion of inlet velocity profile and turbulent flow development. Small domain may cause severe blockage effect which contributes towards increased flow speed and reduced pressure on both the roof and leeward building façade (Oliveira and Younis, 2000). The recommended domain range by Oliveira and Younis (2000) was 5 building height, $5H_e$ at the upstream, 10 building height, $10H_e$ at the downstream and 4 building height, $4H_e$ on the either side of the building model. The recommended domain height was 5 building height, $5 H_e$ from the roof of building model (Cheng, 2007).

2.5.3 Meshing

Based on previous work by Cheng (2007), the region surrounding the building were applied finer elements to focus on the airflow and pressure distribution. Whereas the larger sized elements were applied on the regions far away from the building model to conserve computational resources and time as shown in Figure 2.5. From the previous simulations of Tominaga et al (2015) showed that there was only small difference of simulation results between the usage of fine and basic grids. Basic grid had a better balance in computational cost and accuracy. Besides, Cheng (2007) previous simulations showed that any meshing that exceeded 2 million number of elements had an exponential increase in processing duration for a computational power of 1.60GHz of processor and 1GB of RAM.

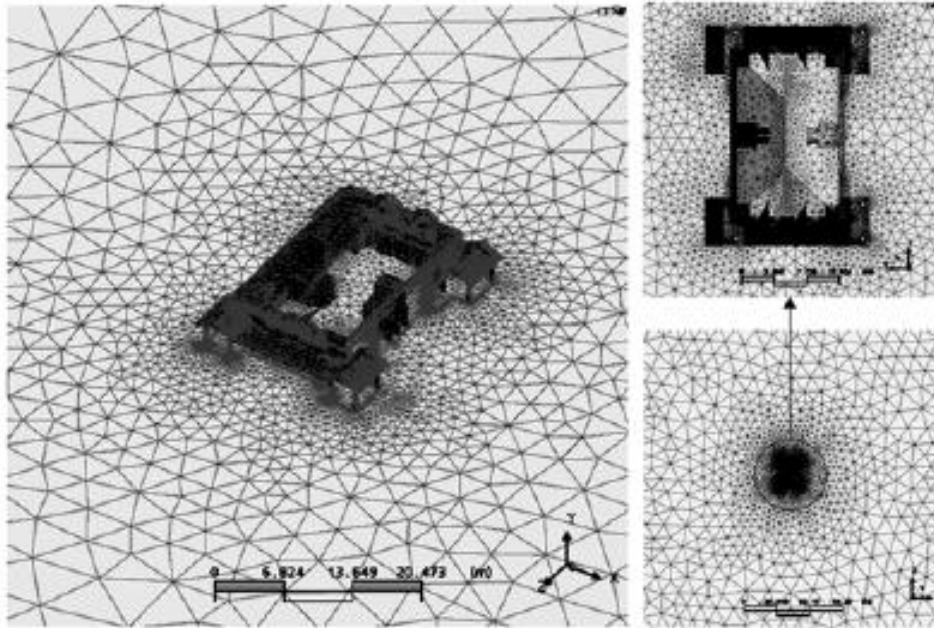


Figure 2.5: Meshing for Building Model. (source: Cheng (2007))

2.5.4 Turbulent Models

Simulation by Hoxey and Richards (1993) showed that standard $k - \varepsilon$ turbulence model struggled to simulate the flow separation on the roof of building model. Four turbulence model: standard $k - \varepsilon$, realizable $k - \varepsilon$, $k - \omega$ SST and RNG $k - \varepsilon$ used in Tominaga et al (2015) previous simulations revealed small differences in stream wise velocity results and the results satisfactorily matched the wind tunnel experiment results. Simulations in previous research by Tominaga et al (2015) showed that standard $k - \varepsilon$ and realizable $k - \varepsilon$ turbulence model overestimated turbulent kinetic energy values while $k - \omega$ SST and RNG $k - \varepsilon$ turbulence model predicts the closest value to the measured value obtained from the wind tunnel test. Overall simulations indicated RNG $k - \varepsilon$ turbulence model provided the highest performance among all turbulence models in simulations as shown in Figure 2.6.

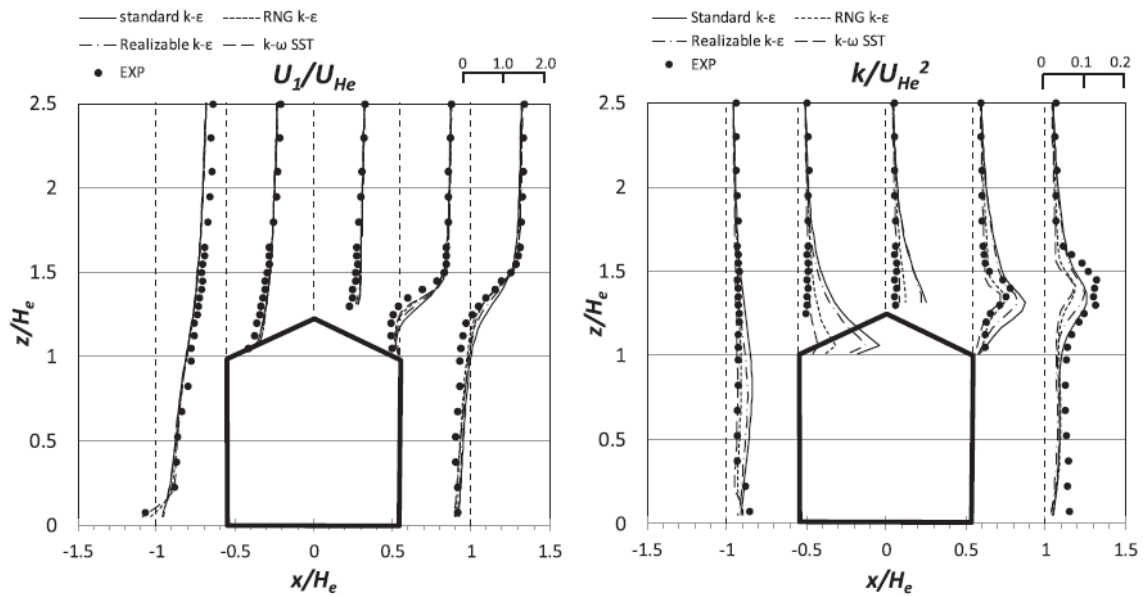


Figure 2.6: Comparison of Streamwise Velocity, U_1 and Turbulent Kinetic Energy, k from Different Turbulent Model. (Source: Tominaga et al, 2014)

2.5.5 Boundary Conditions

Air with density of 1.185 kg/m^3 and dynamic viscosity of $1.831 \times 10^{-5} \text{ kg/ms}$ with temperature of 25°C was defined as the fluid flow in the computational domain according to previous work by Cheng (2007). With reference of previous work by Kikumoto et al (2017), Power Law is suitable to model wind speed more than 6 m/s where it will converges to 0.25. The accuracy of Power Law decreases to 0.21 with the decrease in wind speed and average observation time intervals. The Power Law conclusion was made by comparing to actual wind profiles and turbulence statistics in Tokyo urban boundary layer for 7 months. Previous work of Tominaga et al (2015) stated that approaching airflow that has Power Law with exponent of 0.25 conform to a suburban terrain.

CHAPTER 3

METHODOLOGY

3.1 INTRODUCTION

This chapter explains the entire process of the project with an illustration of flowchart as shown in Figure B1 in Appendix B. The Computational Fluid Dynamics (CFD) software, ANSYS 16.0 FLUENT was used to perform all the planned simulations. The CFD setup, validation and verification are discussed in the succeeding sections. The simulation results obtained were then compared among different roof shapes and wind approach angles to analyse the natural ventilation potential of the building model.

3.2 GEOMETRY OF THE BUILDING MODELS

Four different roof shapes for a particular building model were investigated: gable, pyramidal, shed and concave due to the findings of roof geometry impact on building cross-ventilation performance by Peren et al (2015) stated in Section 2.5.1. The dimensions of model were referred from the work of Tominaga et al (2014). In Tominaga et al (2014), the targeted roof shape was gable type. The length, L and the width, W of the model were in the ratio of 1.1 versus the height of the model, H_e as shown in Figure 3.1. The height of the model, H_e was set identical at 6 meters for all types of roof shape. Three other roof shapes: barrel vault, pyramidal and shed used the same building model length, L , width, W and height, H_e with the roof dimension adjusted to provide the same cross sectional area when viewed from the north façade. Figure 3.2 shows the dimensions of building models for each roof shapes.

Based on the findings of wind approach angle influence on the airflow around a building by Afshin et al (2016) stated in Section 2.2, a total of eight different wind directions were planned for the simulation. The first wind direction is normal to the building north façade and referred as 0° , followed by wind direction at 45° , 90° , 135° , 180° , 225° , 270° and 315° . Figure 3.3 illustrates the wind approach angles relative to the building model facades. Since the wind was set to enter the computational domain at the inlet, the different wind approach angles was realized by rotating the building model on the Z axis. As an example, the building model was rotated on the Z axis by 45° for the 45° wind approach angle case. The degree of rotation was based on the angle of wind approach towards the building model.

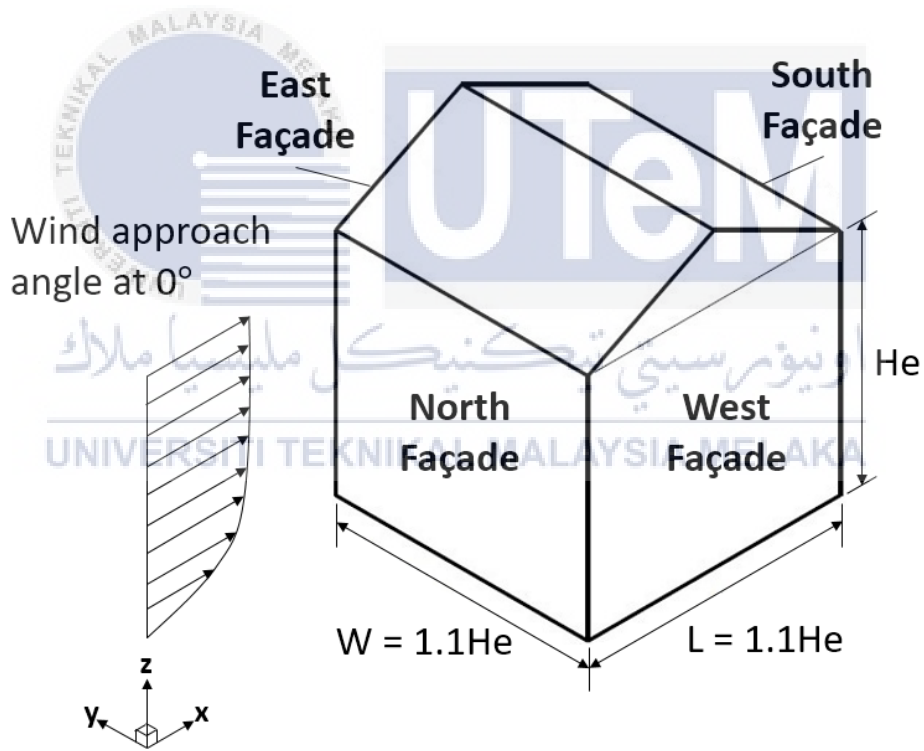


Figure 3.1: The Default 0° Wind Approach Angle Relative to the Building Model

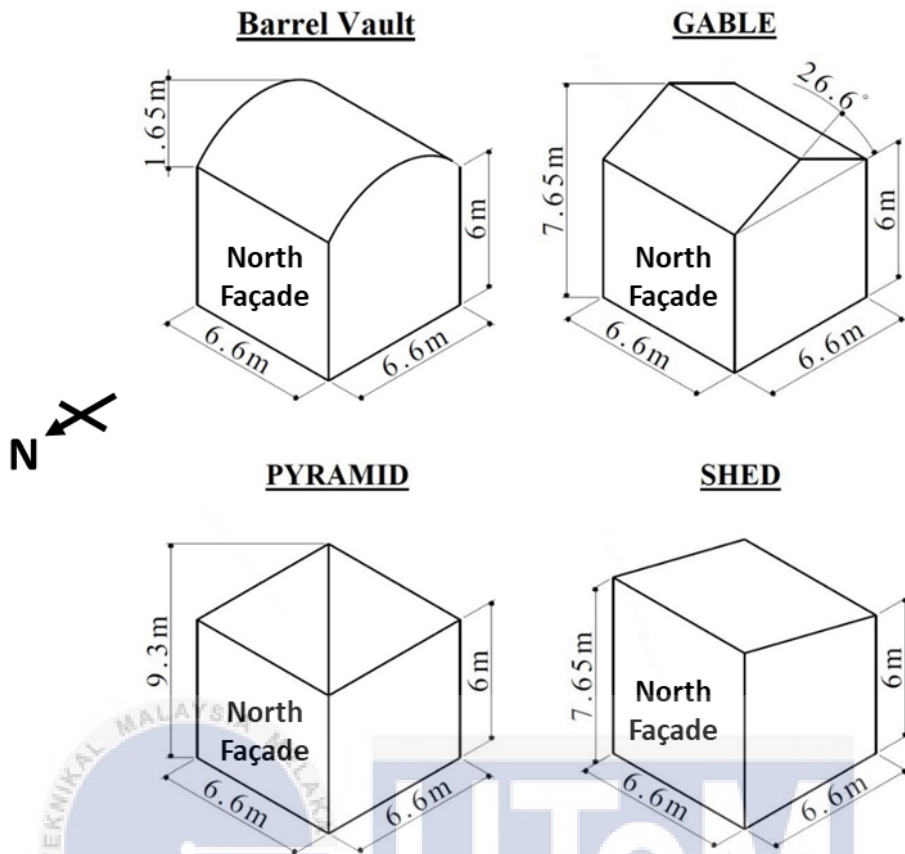


Figure 3.2: The Building Model Dimensions of Barrel Vault Roof (Top Left), Gable Roof (Top Right), Pyramid Roof (Bottom Left) and Shed Roof (Bottom Right).

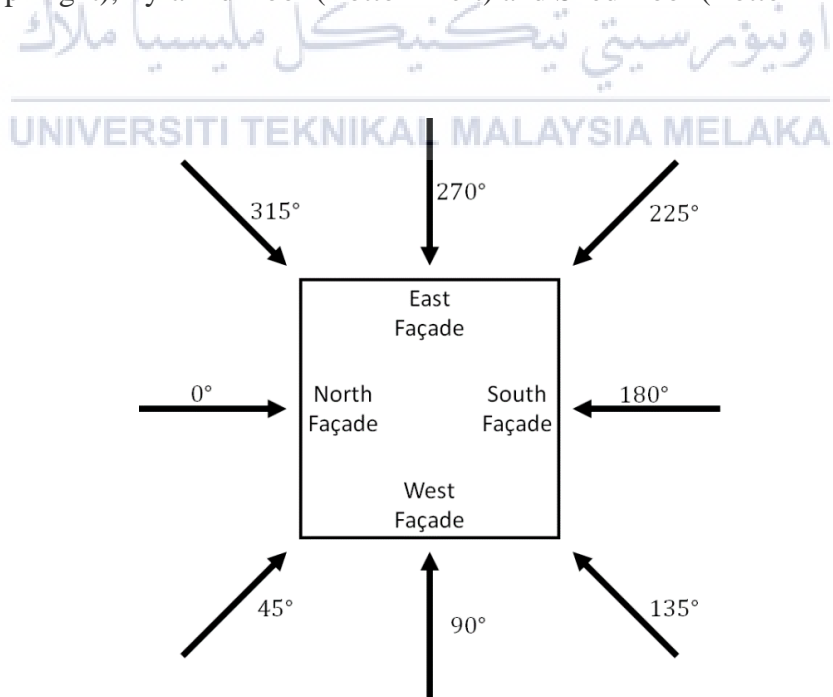


Figure 3.3: The Top View of the Building Model Facades Relative to the Wind Approach

3.3 COMPUTATIONAL DOMAIN

The domain size followed the previous work of Tominaga et al (2015) which was 126 m (Length), 54 m (Width) and 54 m (Height) as shown in Figure 3.4. The domain range from the windward façade of the building model was 42 m, more than the 5 building height, $5H_e$ (30 m) recommended at upstream; the domain range from the leeward façade of the building model was 77.4 m, more than the 10 building height, $10H_e$ (60 m) recommended at downstream; the domain range on the either side of the building model was 23.7 m, close to the recommended 4 building height, $4H_e$ (24 m); domain height was minimum 46.35 m from the roof, more than the recommended 5 building height, $5 H_e$ (30 m) stated by Oliveira and Younis (2000) and Cheng (2007) in Section 2.5.2.

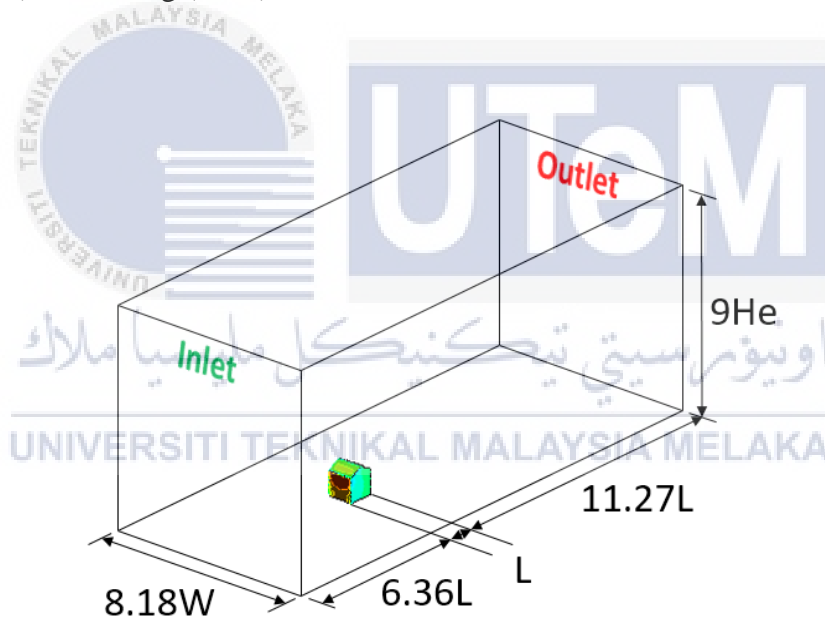


Figure 3.4: The Dimensions of the Computational Domain

3.4 MESHING

By referring to the findings of the previous simulation by Cheng (2007) stated in Section 2.5.3, the domain was discretized into 1.5 million tetrahedral elements with 4 hundred thousand nodes. There were three regions in the domain that required finer meshing for better data gathering: the inlet, the exterior surface of the building, the region around the building, the region on the leeward side of the model and ground. These three regions were the main focus to capture the turbulent or backflow in the domain.

For the exterior façade of the building model, 10 prismatic cell layers were applied with default smooth transition ratio and growth rate of 1.1 while face sizing was imposed with 100 mm element size for each surface area of the model. The region around the building model was applied with body sizing of 500 mm element size. Body sizing of 1200 mm element size was imposed on the region on the leeward side of the model.

Another face sizing of 2500mm was applied on the inlet and ground of the computational domain to better refine the grid closer to the ground. The wind profile comparison revealed the face sizing method on the inlet and ground was able perform similarly as the inflation method as shown in Figure 3.5. As seen from Table 3.1, the face sizing method created approximately 20,000 lesser in the number of element.

Table 3.1: Face Sizing and Inflation Method Comparison

Mesh Type	Number of Elements	Number of Nodes
Face Sizing	1,552,644	446,578
Inflation	1,572,632	476,518

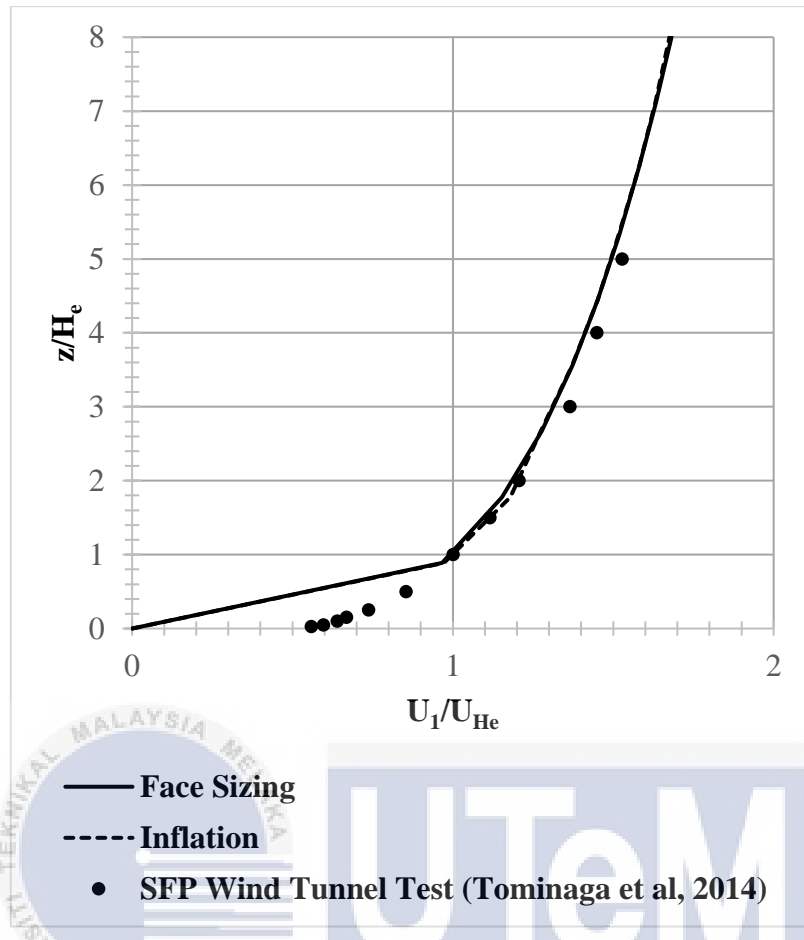


Figure 3.5: Wind Velocity Profile Comparison between Different Mesh Settings and SFP

اونيورمى تىكىچىكل ايا ملاك
UNIVERSITI TEKNIKAL MALAYSIA MELAKA

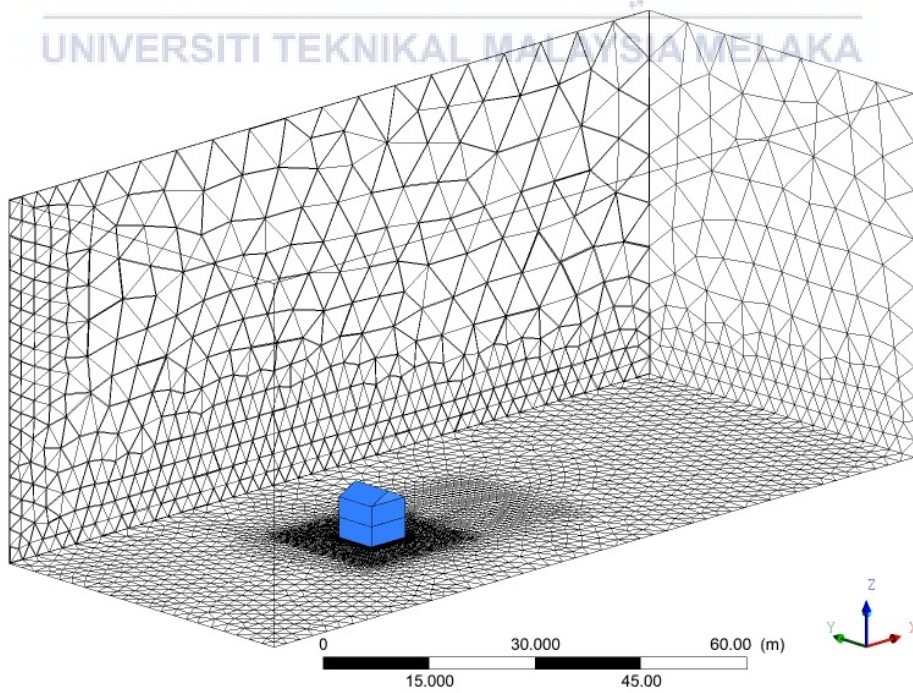


Figure 3.6: The Computational Domain

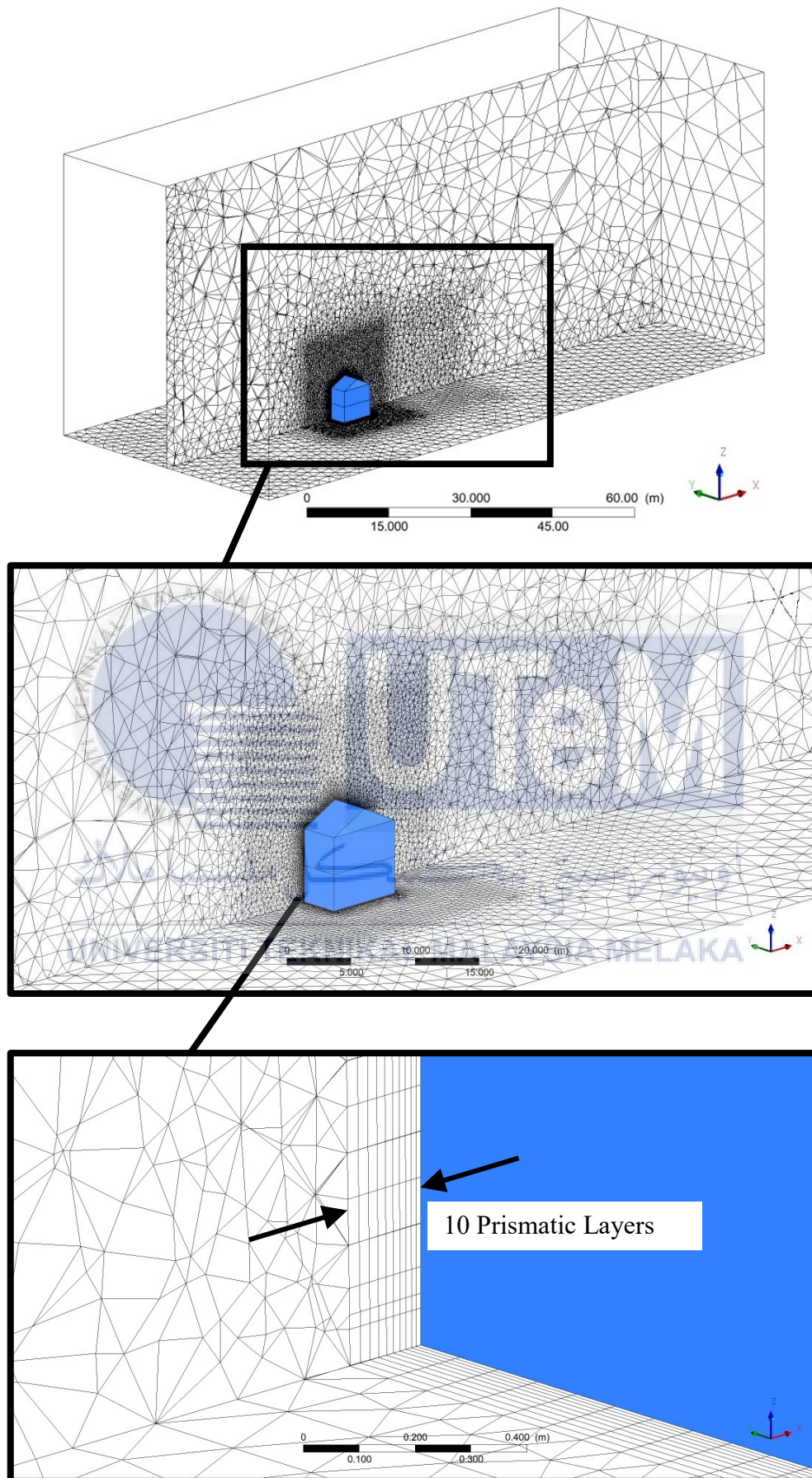


Figure 3.7: The Grid Topology and Prismatic Layers

3.5 TURBULENT MODELS

Based on the simulation results by Tominaga et al (2015) stated in Section 2.5.4, the Standard $k - \varepsilon$ and Realizable $k - \varepsilon$ turbulence models were tested in the simulation. The result comparison showed that the Realizable $k - \varepsilon$ turbulence model had higher sensitivity in capturing wind pressure on the building surface. Hence, the Realizable $k - \varepsilon$ turbulence model was used to obtain the most accurate results in the simulations.

3.6 BOUNDARY CONDITIONS

The definition of wind flow in the computational domain was set according to setting by Cheng (2007) stated in Section 2.5.5. The boundary conditions followed closely according to the previous work of Tominaga et al (2015). The wind was defined as air with properties of 1.225 kg/m^3 in density and 1.7894×10^{-5} in dynamic viscosity. An approaching flow power-law profile was imposed at the inlet as shown in Figure 3.1. Kikumoto et al. (2017) studies provided the power law equation as shown below:

$$U(z) = U_n \left(\frac{z}{z_n}\right)^\alpha$$

Where:

$U(z)$ = wind velocity relative to the height from the ground

U_n = reference wind velocity at reference height

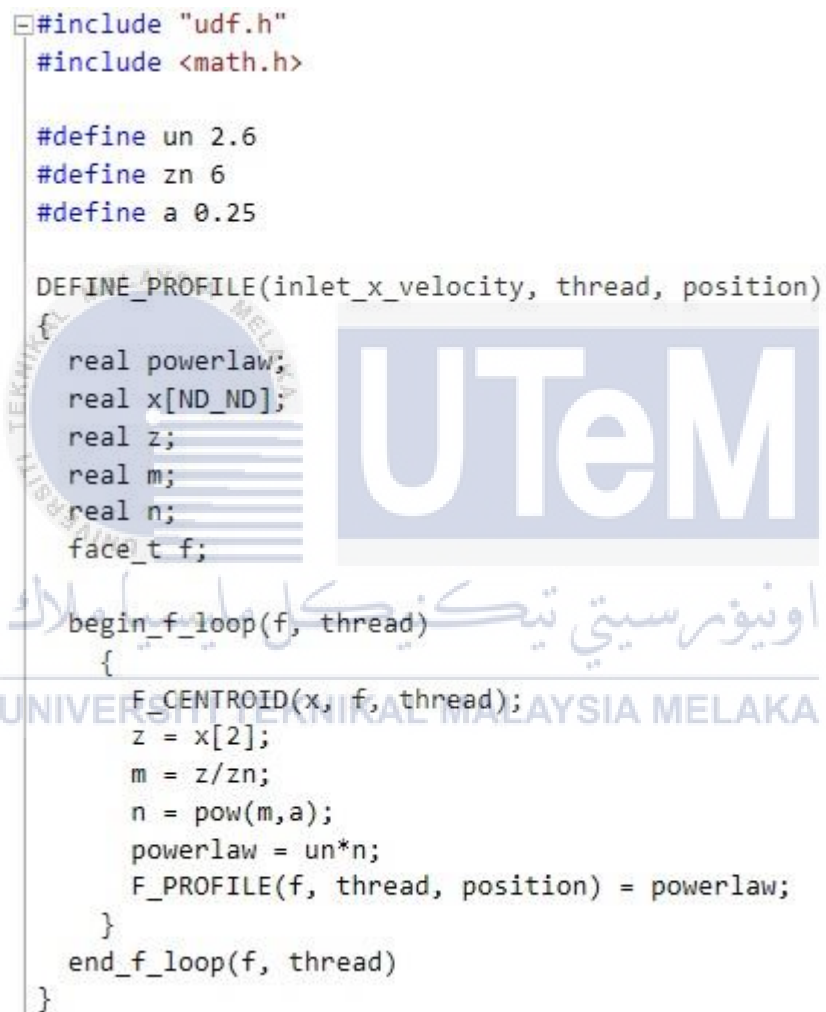
Z = height from the ground

Z_n = reference height from the ground

α = power-law index based on terrain category

To simulate conditions of a suburban terrain as in the studies of Tominaga et al (2014), the reference height from the ground, Z_n was actually building height, $H_e = 6 \text{ m}$ while the reference wind velocity at reference height was set with the streamwise velocity, $U_{H_e} =$

2.6 m/s. The power-law index was 0.25 for a suburban terrain category (Kikumoto et al, 2017). Imposing the power-law equation on the inlet flow in the CFD simulation required the application of User-Defined Function (UDF). The power-law equation was written in C programming language as seen in Figure 3.8 below. The power-law program file was then built and loaded into the ANSYS FLUENT component system through the User-Defined Functions “compiled” feature.



```

#include "udf.h"
#include <math.h>

#define un 2.6
#define zn 6
#define a 0.25

DEFINE_PROFILE(inlet_x_velocity, thread, position)
{
    real powerlaw;
    real x[ND_ND];
    real z;
    real m;
    real n;
    face_t f;

    begin_f_loop(f, thread)
    {
        F_CENTROID(x, f, thread);
        z = x[2];
        m = z/zn;
        n = pow(m,a);
        powerlaw = un*n;
        F_PROFILE(f, thread, position) = powerlaw;
    }
    end_f_loop(f, thread)
}

```

Figure 3.8: Power-Law Equation in UDF C Programming Code

Zero static pressure was applied on the domain outlet. Both of the sides and the top of the domain were applied symmetry boundary conditions zero normal velocity and zero gradients for all the variables. The building surfaces were stationary walls with no slip

conditions. The wall functions on the ground were altered for roughness height, k_s of 1.0mm and roughness constant, C_s of 1.0 to simulate the surrounding terrain conditions of the building model (Tominaga et al, 2014).

3.7 SOLUTION METHODS AND MONITORS

The Coupled Algorithm was applied for Pressure-Velocity Coupling and Least Square Cell Based for Gradient. The pressure interpolation was the Second Order while the Momentum, Turbulent Kinetic Energy and Turbulent Dissipation Rate were in the Second Order Upwind setting. The monitors for residuals was set to absolute convergence criterion. The absolute criteria for residuals of continuity, x-velocity, y-velocity, z-velocity, energy, k and ε were 0.001.



3.8 VALIDATION

The power-law application on the inlet flow was required to be validated against the Tominaga et al (2014) wind tunnel SFP experimental data. The power-law application was validated by comparing the wind velocity profiles on the inlet and across the building model from both CFD simulations and wind tunnel SFP data.

3.8.1 Approaching Flow Vertical Wind Velocity Profile Comparison between CFD with Power Law Implementation versus SFP Wind Tunnel Test

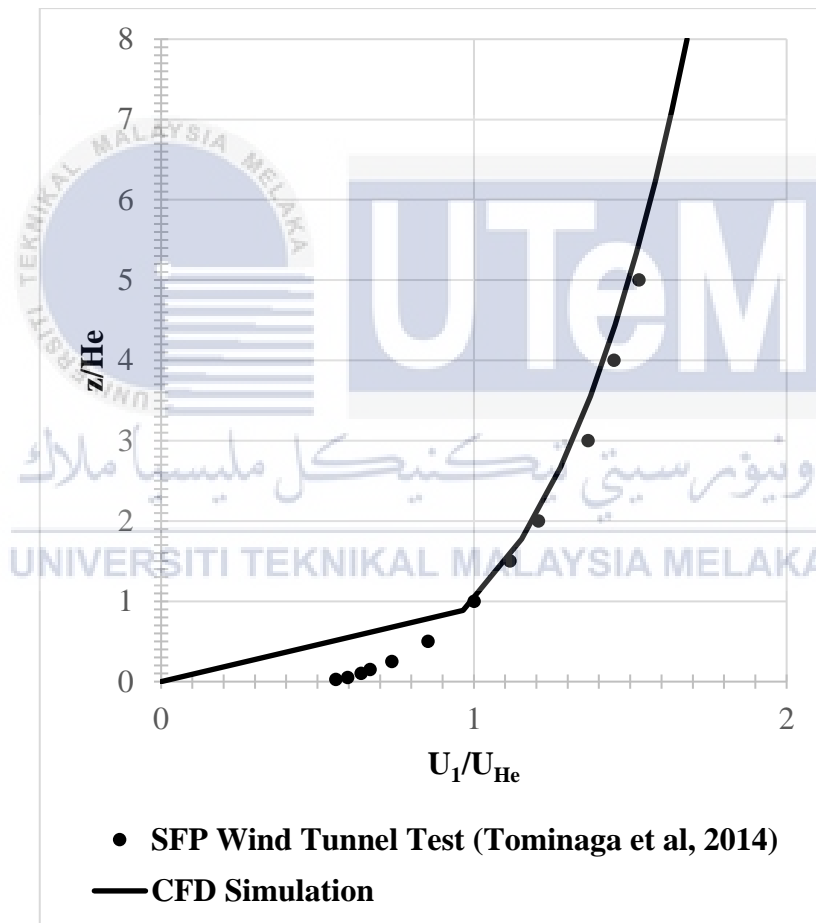


Figure 3.9: The Approaching Wind Velocity Profile Comparison between CFD Simulation and SFP Wind Tunnel Test (Tominaga et al, 2014).

The approaching flow was set to mimic natural wind approach by applying power law in wind velocity during the CFD simulation. Figure 3.9 shows the velocity profile of the approaching flow in CFD simulation versus the approaching flow from wind tunnel test. The approaching flow velocity profile of the CFD simulation followed exactly the same as the approaching flow velocity profile of the wind tunnel test from $z/H_e = 1.0$ onwards. The $z/H_e = 0$ to $z/H_e = 1.0$ was the region where the CFD simulation approaching flow velocity profile strayed away from the wind tunnel test approaching flow velocity profile. The CFD simulation profile shown is the best possible approaching flow velocity profile could be obtained from the CFD settings.



3.8.2 Vertical Wind Velocity Profile Comparison between CFD Power Law and Non-Power Law Implementation in Different Turbulent Models versus SFP Wind Tunnel Test

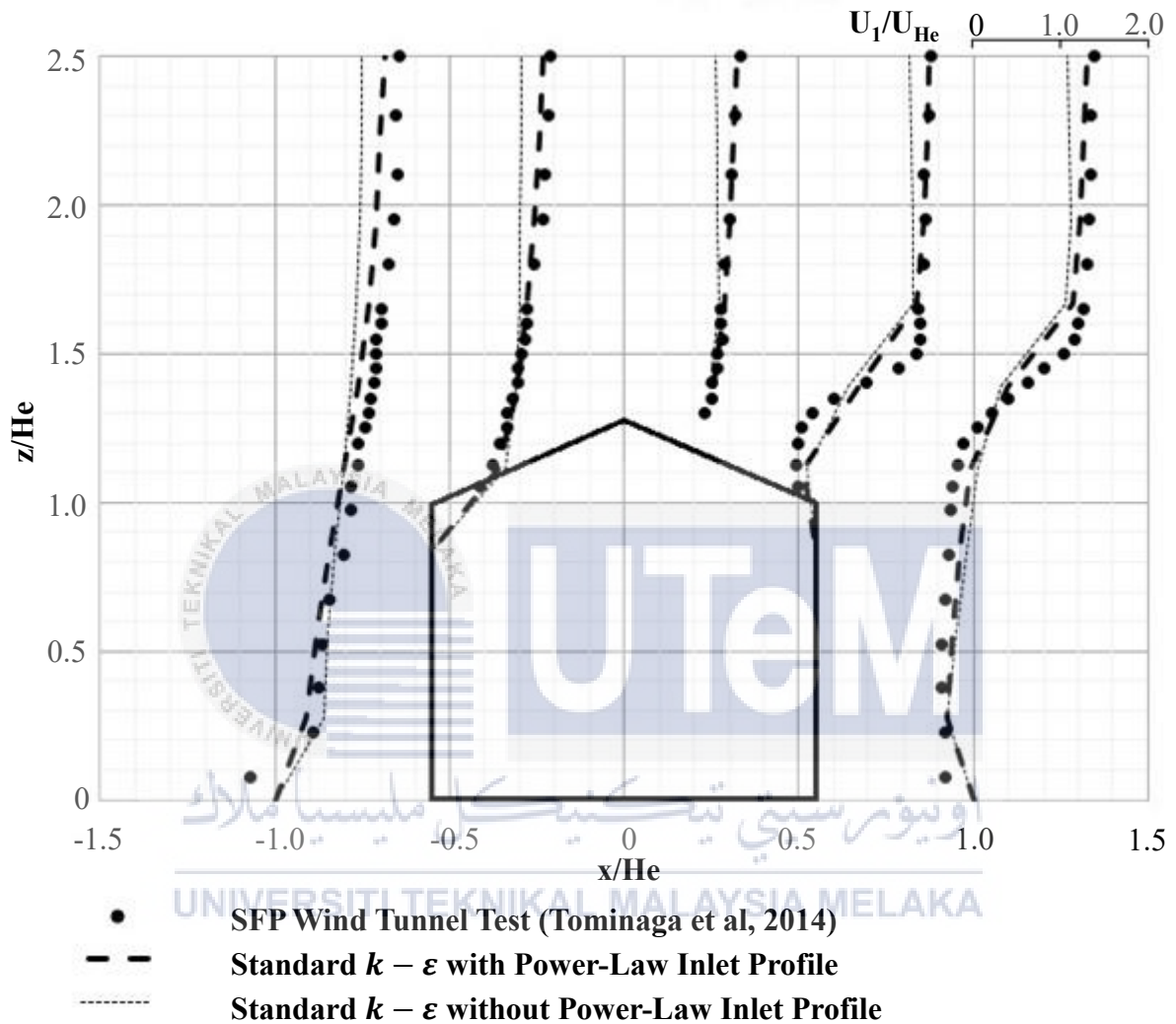


Figure 3.10: Standard $k - \epsilon$ Turbulent Model with Power Law and Non-Power Law Implementation versus SFP Wind Tunnel Test Velocity Profile.

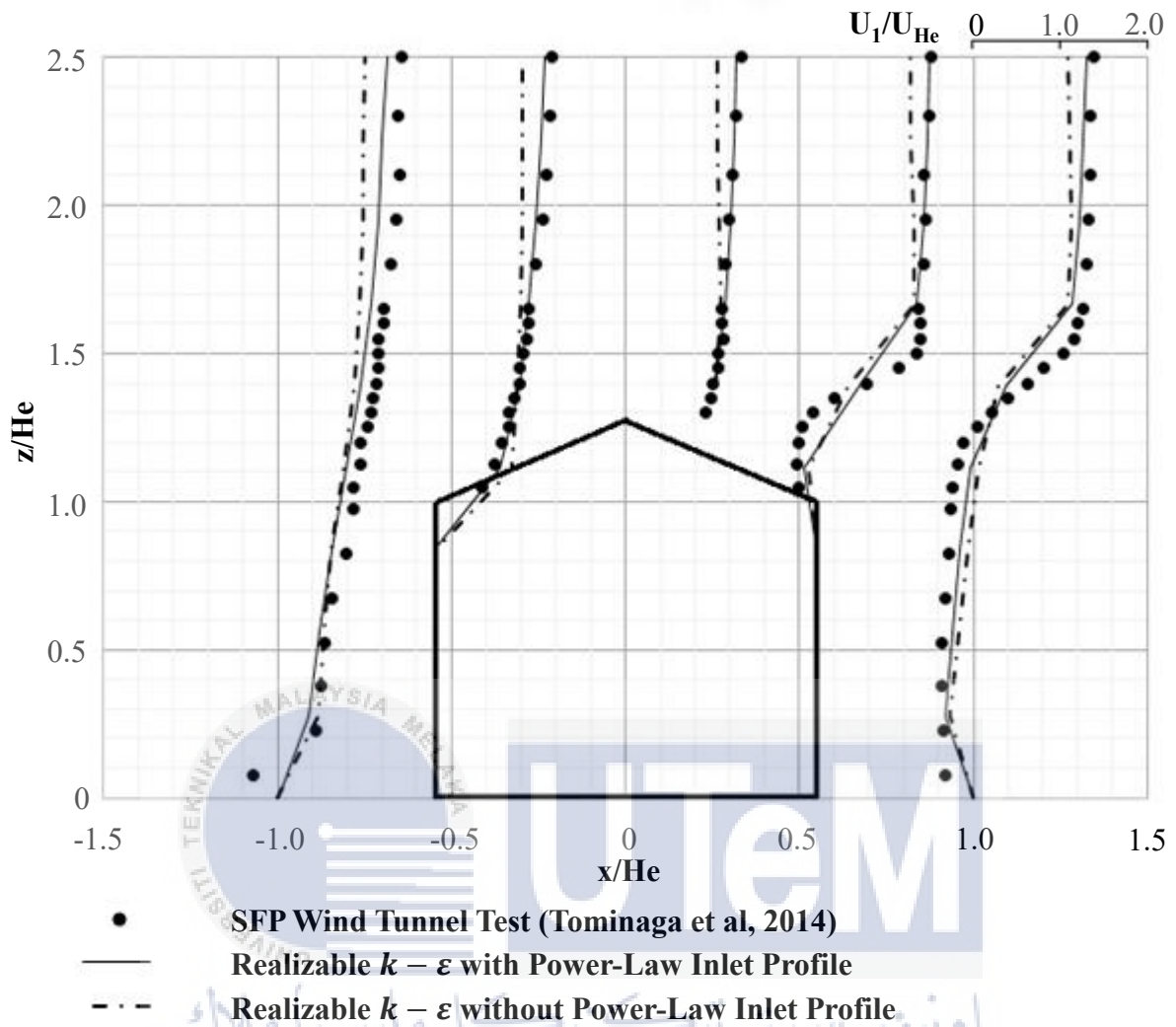


Figure 3.11: The Realizable $k - \varepsilon$ Turbulent Model with Power Law and Non-Power Law Implementation versus SFP Wind Tunnel Test Velocity Profile.

The Standard $k - \varepsilon$ and Realizable $k - \varepsilon$ turbulent models were tested with power law and non-power law implementations on their approaching airflow at the inlet to observe their velocity profile differences against the wind tunnel test. Both turbulent models showed that power law implementation in the approaching airflow at the inlet resembled more closely towards the wind tunnel test velocity profile compared to the non-power law implementation. The similarities in the wind velocity profiles in the CFD simulation and the wind tunnel test validated the adaptation of power law in the inlet approaching airflow.

3.9 VERIFICATION

The verification of the CFD simulation settings was done by employing the Grid Independent Test and the turbulent model comparison. The most suitable CFD settings was selected to ensure the CFD simulations run the most effective and efficient way.

3.9.1 Grid Independent Test

In the Grid Independent Test, three different grid size were applied to study the grid sensitivity: Coarse, Basic and Fine. Each of the grid qualities differed from each other by 25% in the grid size. Table 3.2 shows the details of each mesh quality settings.

Table 3.2: Grid Independent Test

Grid Quality	Coarse	Basic	Fine
Grid Size	125%	100%	75%
No. of Element	982,824	1,561,345	2,920,275
Nodes	286,152	448,550	818,560
Time Used (Mins)	15.6333	20.1000	105.0833
Pressure Difference (Pa)	3.3905	5.3413	5.8961

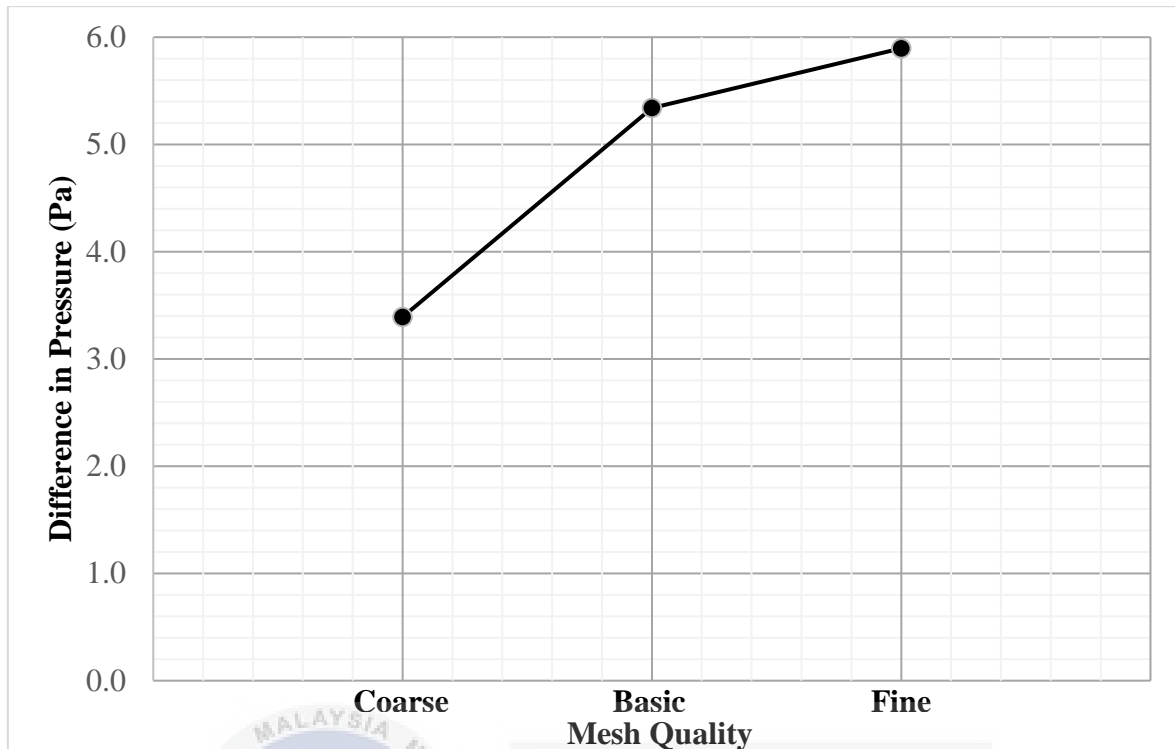


Figure 3.12: Pressure Difference between Windward and Leeward Building Façade versus Number of Element

The Basic Mesh Quality Simulation increased the number of elements and nodes by 58.86 % and 56.75% from the Coarse Grid Quality. The Basic Grid Quality Simulation time increased by 28.57% and the pressure difference were recorded at a 57.54% increase compared to Coarse Grid Quality. The Fine Grid Quality Simulation increased the number of elements and nodes by 87.04% and 82.49% from the Basic Grid Quality. The Fine Grid Quality Simulation time increased by 422.80% and the pressure difference were recorded at a 10.39% increase only when compared to the Basic Grid Quality. Apart from that, the number of element in Fine Grid Quality approached three millions which caused a huge burden to a Dual-Core 1.6GHz processor. The huge consumptions in simulation time and processing power were not able to justify the use of Fine Grid Quality. Thus, the Basic Grid Quality was selected as the most practical application in the CFD simulation.

3.9.2 Turbulent Model Comparison

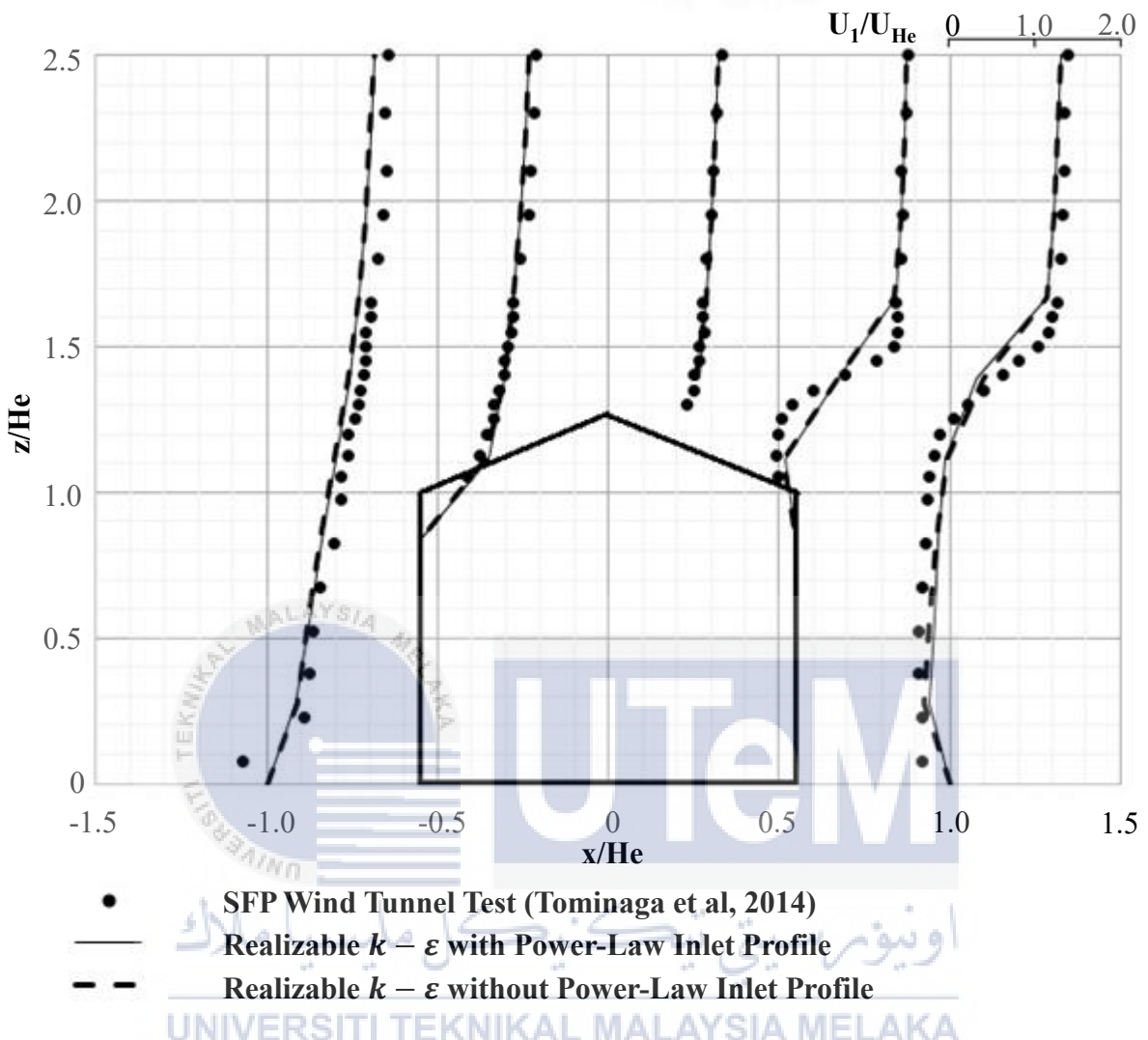


Figure 3.13: Wind Velocity Profiles Comparison of CFD with Different Turbulent Models versus Actual Wind Tunnel Test

As part of the validation, two turbulent models were compared to select the best fit model. The Standard $k - \epsilon$ and Realizable $k - \epsilon$ were chosen for simulation testing. The result represented in Figure 4.2 shows that there was no significant difference between the wind velocity profiles of both turbulent models. Both turbulent model wind velocity profiles were exact to the wind tunnel test wind velocity profile at whole computational domain except for the leeward region on the building model. These two turbulent models struggled

to capture the backflow of the wind properly and produced similar wind velocity profile. The Realizable $k - \epsilon$ and Standard $k - \epsilon$ turbulent model scored fair in the wind velocity profile comparison.

Table 3.3: Turbulent Model Comparison

Turbulent Model	Standard k-ϵ	Realizable k-ϵ
Time Used (Mins)	18.6167	20.1000
Pressure Difference (Pa)	3.7619	5.3413

Due to the draw in the wind velocity profile comparison, the wind pressure differences from both turbulent model were compared to determine the best application as shown in Table 3.3. The Realizable $k - \epsilon$ turbulent model captured higher pressure difference at 5.3413 Pascal compared to Standard $k - \epsilon$ turbulent model at 3.7619. The pressure difference of the Realizable $k - \epsilon$ turbulent model was 41.98% increase from the pressure difference of Standard $k - \epsilon$ turbulent model. Although the Realizable $k - \epsilon$ turbulent model has increased the simulation time by 7.97%, the time increment was in an acceptable 10% range. The Grid Independent Test further showed that in the finer mesh settings, the pressure difference value recorded approaches 6.0 Pa. Hence, the Realizable $k - \epsilon$ turbulent model was adopted into the CFD simulation.

CHAPTER 4

RESULTS AND DISCUSSIONS

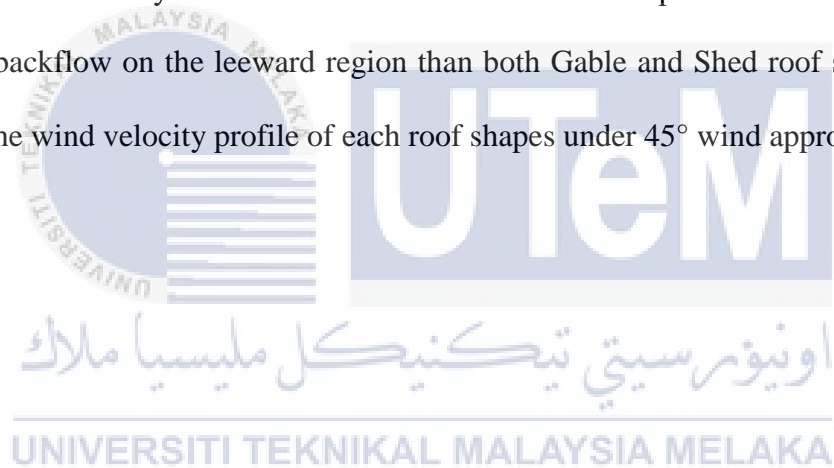
4.1 WIND VELOCITY PROFILE

The wind velocity profile is one of the key parameters in this CFD simulation to observe the airflow around the building model. The wind velocity profiles for 0° , 90° , 180° and 270° wind approach angle cases were obtained at distance of $x/H_e = -6.6, -3.3, 0, 3.3$ and 6.6 with $x/H_e = 0$ as the center of the building model. As for $45^\circ, 135^\circ, 225^\circ$ and 315° wind approach angle cases, the wind velocity profiles were obtained at distance of $x/H_e = -6.6, -4.6669, -3.3, 0, 3.3, 4.6669$ and 6.6 with $x/H_e = 0$ as the center of the building model. Only the wind velocity profiles for 0° and 45° wind approach angles will be explained in this section as they showed how wind velocity profiles formed when wind approaches from the normal of the façade and from the building edge. The rest of the wind profiles will be shown in appendix from Figure C1 to C6 for further references.

In the 0° wind approach angle, The Barrel Vault roof induced the largest wind velocity profile, the Gable roof came in second place, followed by the Shed roof and lastly the Pyramid roof. Both semi-symmetrical roof shapes: the Barrel Vault and the Gable created the largest wind velocity profile when the wind approach angle is normal to the building façade. The asymmetrical Shed roof created moderate wind velocity profile in this wind approach angle. Meanwhile, the full-symmetrical Pyramid roof had the smallest wind velocity profile. All roof shapes were observed to have significant backflow on the leeward

region except the Barrel Vault roof. Figure 4.6 shows the wind velocity profile of each roof shapes under 0° wind approach angle.

In the 45° wind approach angle, The Shed roof induced the largest wind velocity profile, the Gable roof came in second place, followed by the Barrel Vault roof and lastly the Pyramid roof. The asymmetrical Shed roof created the largest wind velocity profile when the wind approach angle is normal to the building façade. Both semi-symmetrical roof shapes: the Barrel Vault and the Gable created the moderate wind velocity profile in this wind approach angle. Meanwhile, the full-symmetrical Pyramid roof had the smallest wind velocity profile. The Pyramid and the Barrel Vault roof shapes were observed to have significant backflow on the leeward region than both Gable and Shed roof shapes. Figure 4.7 shows the wind velocity profile of each roof shapes under 45° wind approach angle.



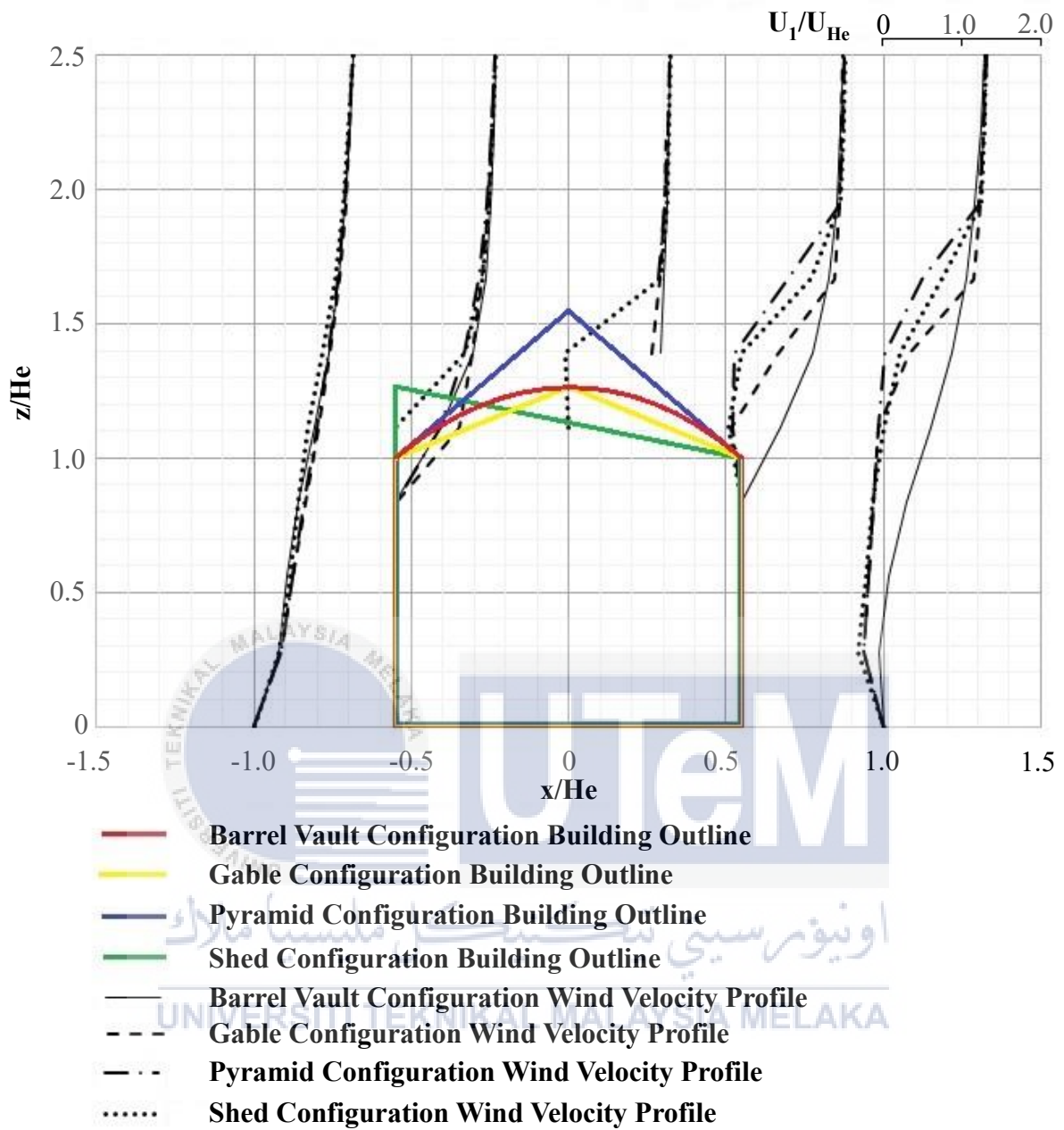


Figure 4.1: The Wind Velocity Profile of Each Roof Shapes on 0° Wind Approach Angle.

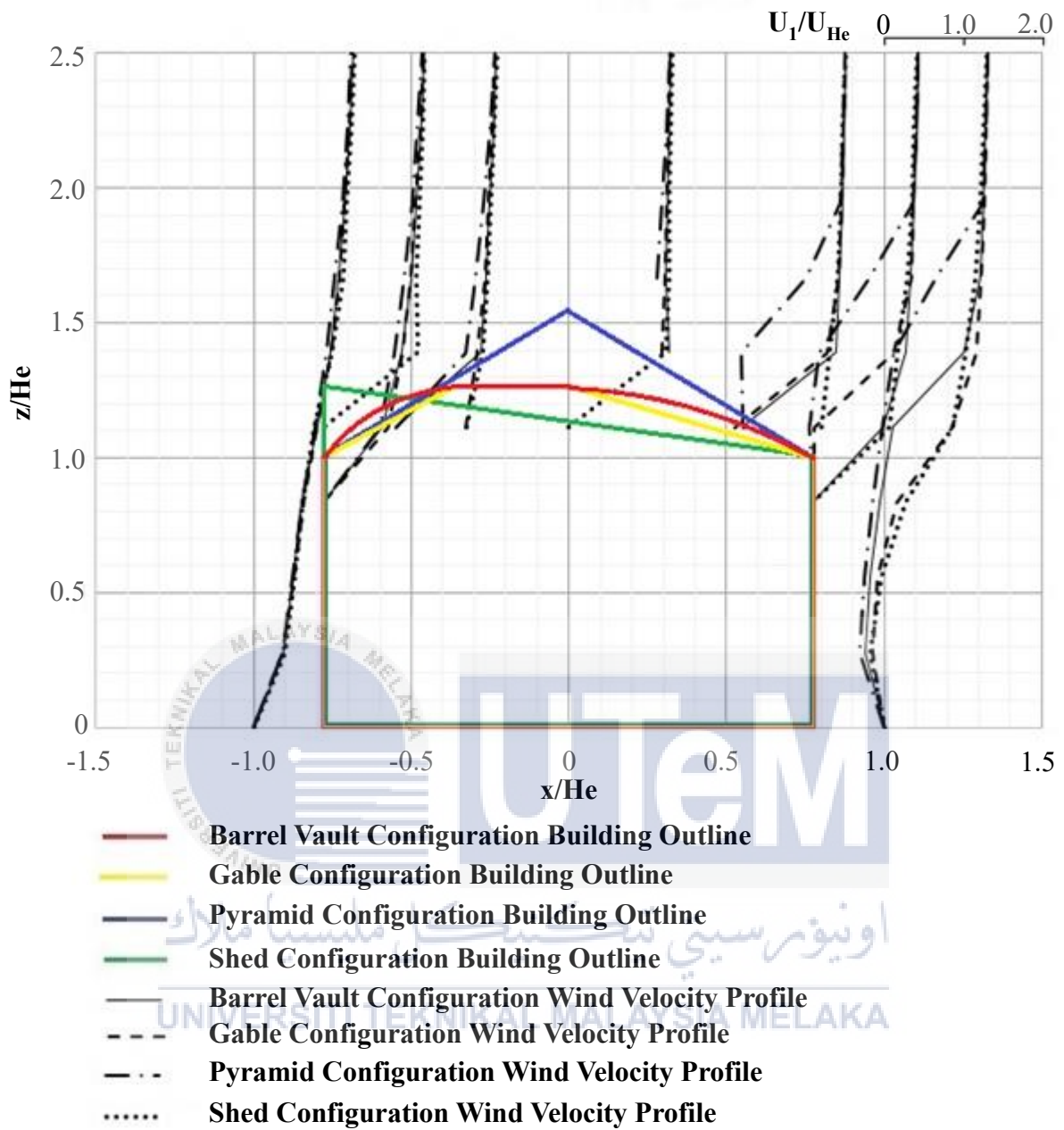
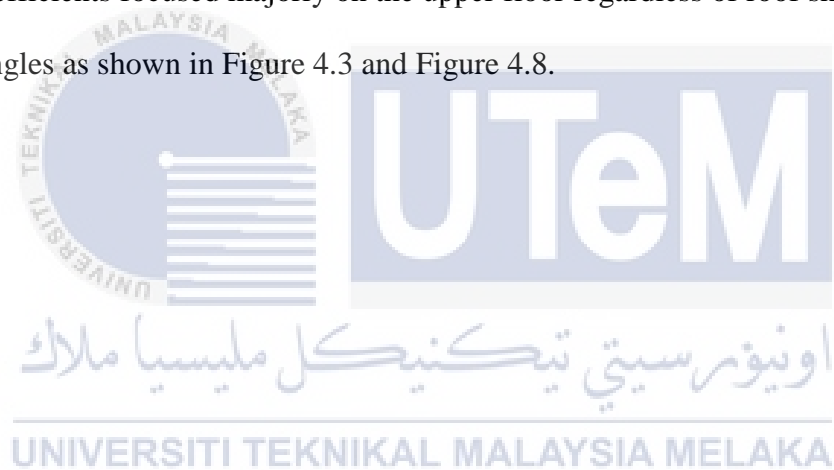


Figure 4.2: The Wind Velocity Profile of Each Roof Shapes on 45° Wind Approach Angle.

4.2 COEFFICIENT OF WIND PRESSURE DISTRIBUTION AROUND THE BUILDING MODEL

Figure 4.3 shows the pressure coefficient distribution contour around the building model under 0° wind approach angle while Figure 4.8 shows the pressure coefficient distribution contour around the building model under 45° wind approach angle. Figure 4.3 illustrates the pressure coefficient distribution pattern when the wind approach angle is normal to the building façade. Figure 4.8 on the other hand, illustrates the pressure coefficient distribution pattern when the wind approached the building model from one of its edges. From the contours, it is interesting to note that both maximum and minimum pressure coefficients focused majorly on the upper floor regardless of roof shapes and wind approach angles as shown in Figure 4.3 and Figure 4.8.



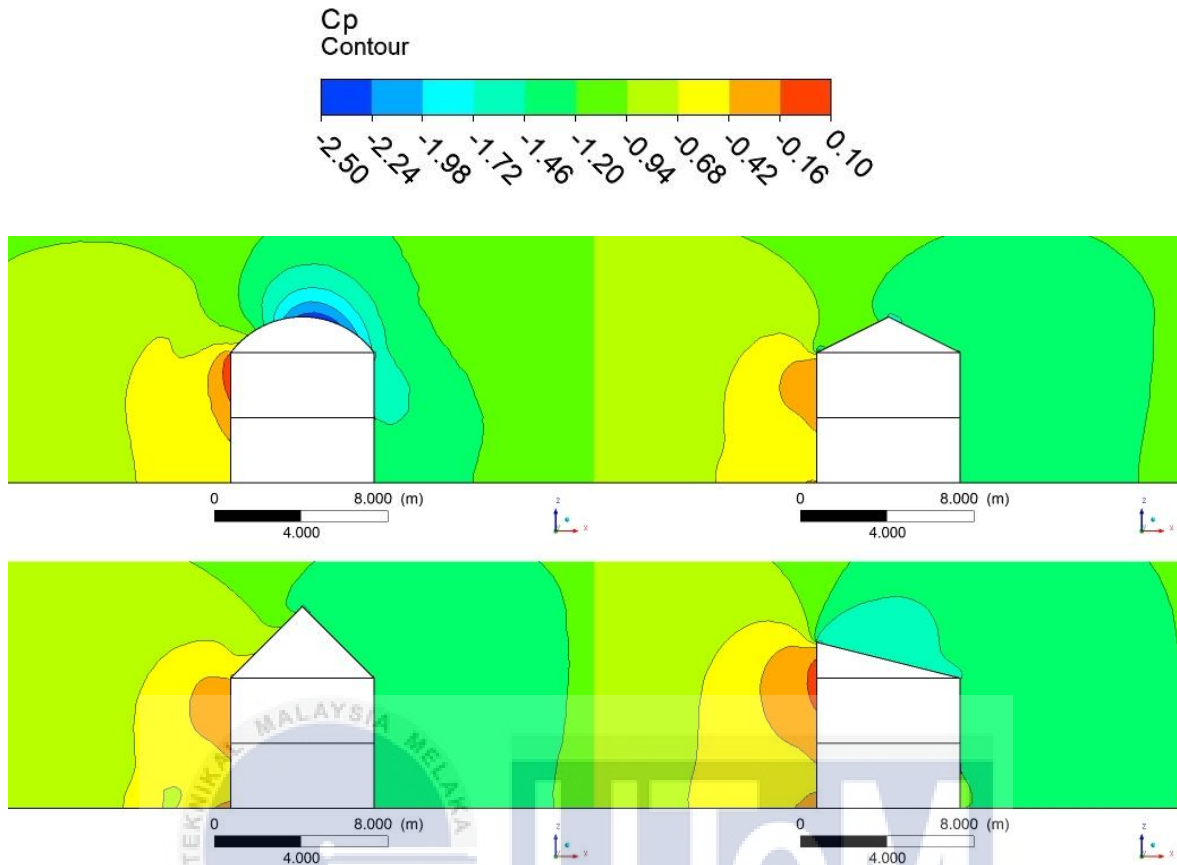


Figure 4.3: The Wind Pressure Coefficient Distribution Contour around the Building Model of Barrel Vault Roof (Top Left), Gable Roof (Top Right), Pyramid Roof (Bottom Left) and Shed Roof (Bottom Right) under 0° Wind Approach Angle.

When the wind approach angle is normal to the building facades, each roof shapes will create different maximum wind pressure coefficient on the windward surface. In this case, Shed roof configuration produced the largest maximum wind pressure coefficient as it has the largest windward surface area. The barrel vault roof configuration also created a significant wind pressure coefficient on the windward facades although a similar shape in a blunt body will be considered as the most aerodynamic shape in the wind tunnel test. On the leeward side, only the Barrel Vault roof configuration managed to build up negative wind pressure coefficient on the ground floor compared to other roof configurations.

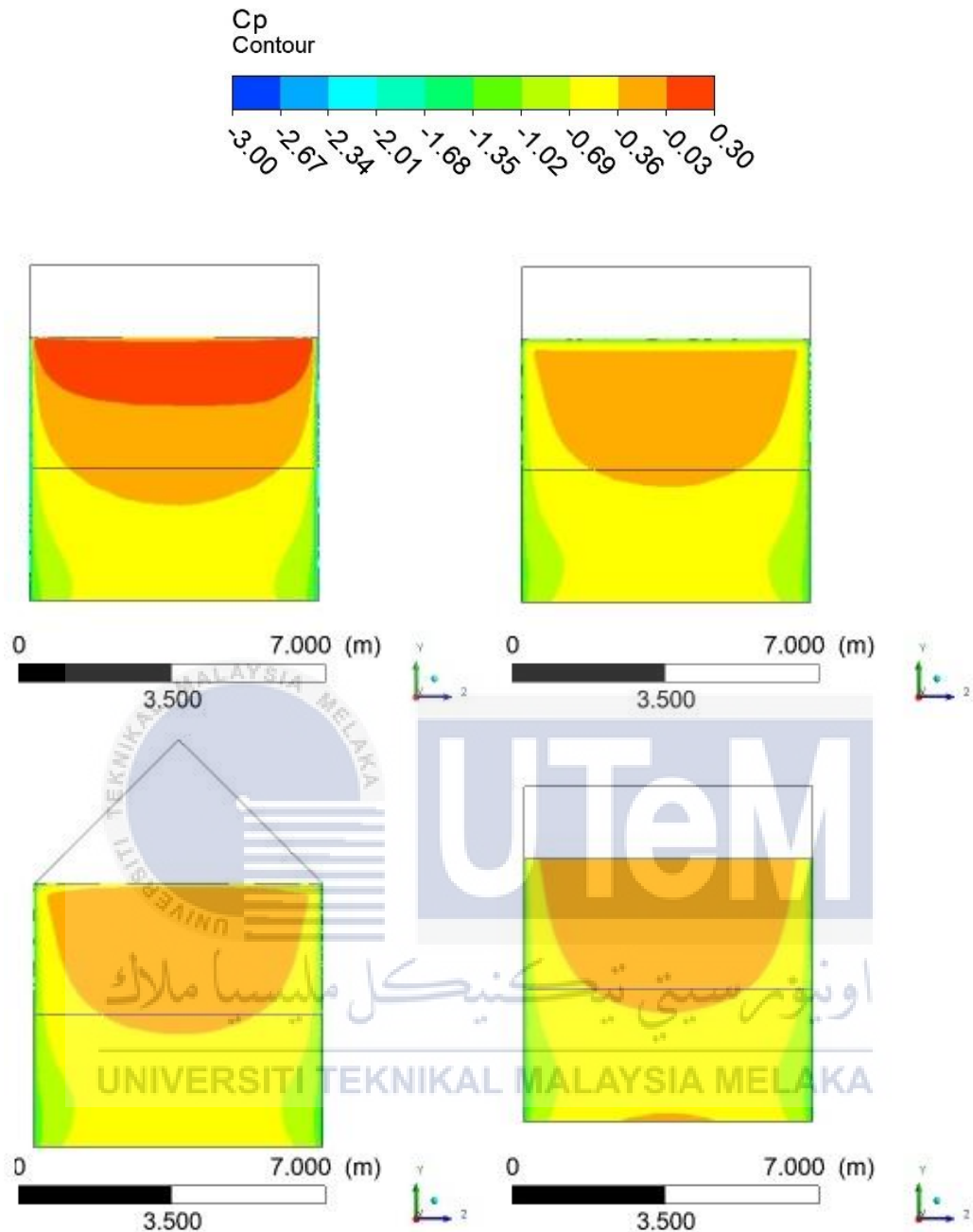


Figure 4.4: The Wind Pressure Coefficient Distribution Contour on the North Facade of Barrel Vault Roof (Top Left), Gable Roof (Top Right), Pyramid Roof (Bottom Left) and Shed Roof (Bottom Right) under 0° Wind Approach Angle.

Across all roof configurations, the Barrel Vault was the only roof able to generate the maximum pressure coefficient at the top edge of the north facade upper floor. The rest of the roof produced similar pressure coefficient contour as seen in Figure 4.4.

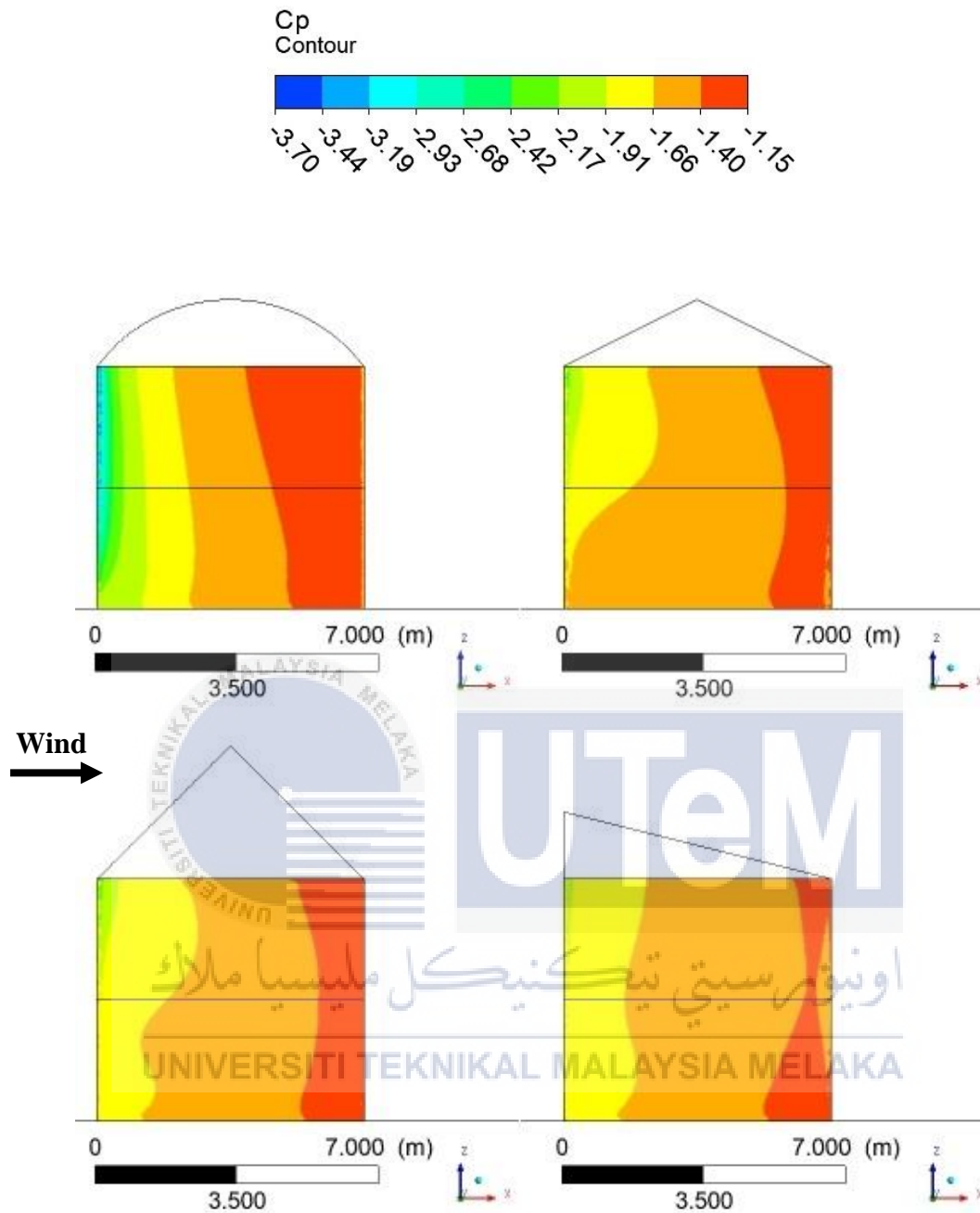


Figure 4.5: The Wind Pressure Coefficient Distribution Contour on the East Facade of Barrel Vault Roof (Top Left), Gable Roof (Top Right), Pyramid Roof (Bottom Left) and Shed Roof (Bottom Right) under 0° Wind Approach Angle.

The minimum pressure coefficient can be observed on the east facade upper and ground floor of the Barrel Vault Configuration. The rest of the roof produced similar pressure coefficient ranging from -2.17 to -1.15 as seen in Figure 4.5.

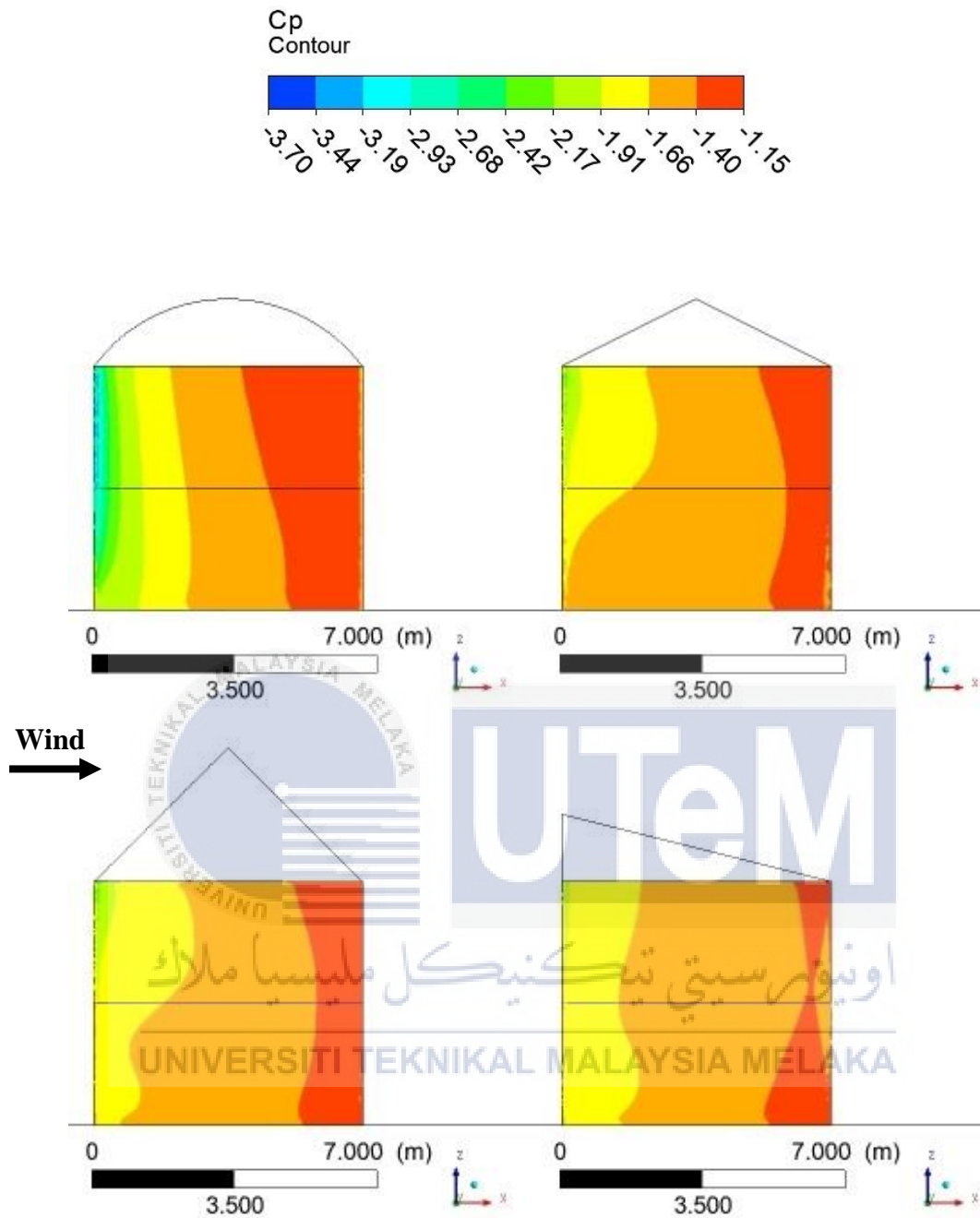


Figure 4.7: The Wind Pressure Coefficient Distribution Contour on the West Facade of Barrel Vault Roof (Top Left), Gable Roof (Top Right), Pyramid Roof (Bottom Left) and Shed Roof (Bottom Right) under 0° Wind Approach Angle.

On the west façade, the pressure coefficient contour showed the same as the ones on the eastward façade with the minimum pressure coefficient observed on the ground and upper floor of the Barrel Vault Configuration.

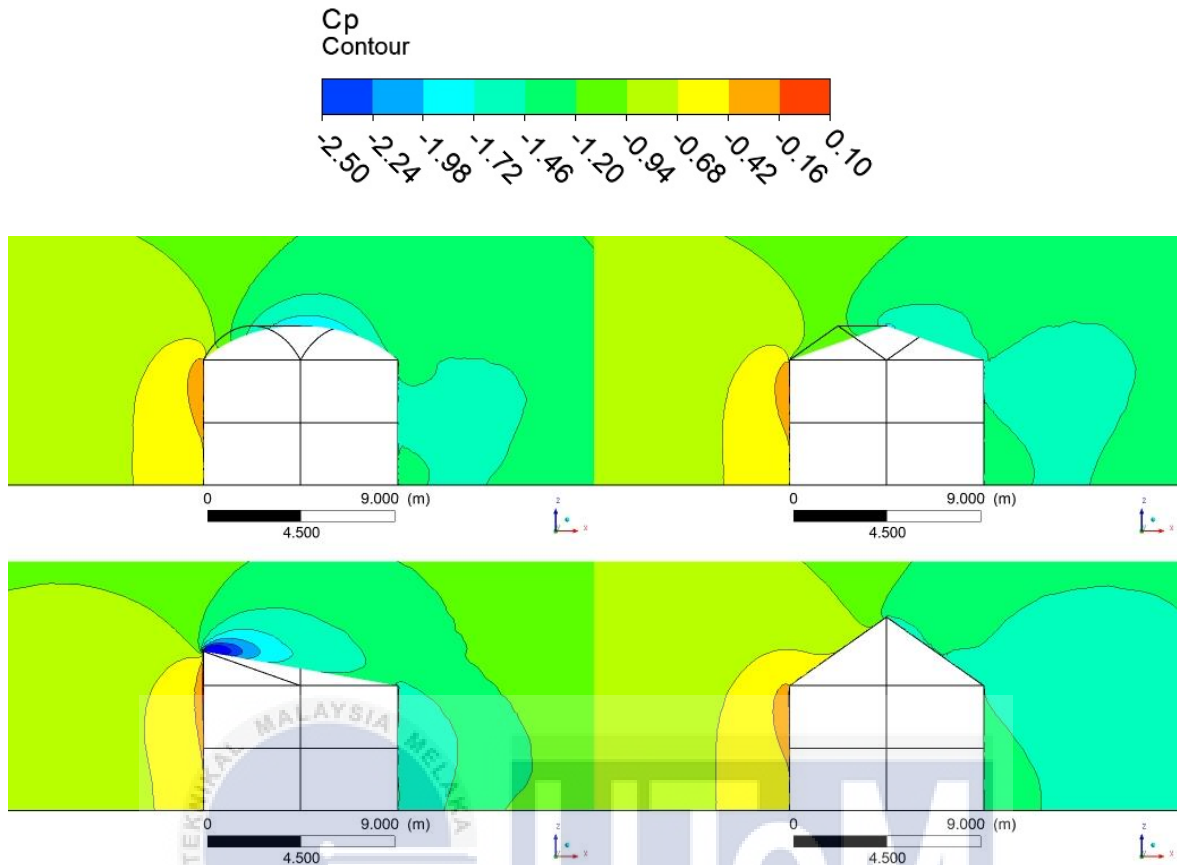


Figure 4.8: The Wind Pressure Coefficient Distribution Contour around the Building Model of Barrel Vault Roof (Top Left), Gable Roof (Top Right), Pyramid Roof (Bottom Left) and Shed Roof (Bottom Right) under 45° Wind Approach Angle.

The outcome of the wind pressure coefficient difference of each roof shapes by the 45° wind approach angle was trending similarly as the results in the average wind approach angle. Hence, it could be used to predict from the wind pressure coefficient distribution contour of the average wind approach angle. On the windward building edge side, the maximum wind pressure coefficient distribution created was similar on each roof shapes as seen on Figure 4.8.

But on the leeward side, the Shed roof configuration produced the largest low wind pressure coefficient region that covered the ground and upper floor. The next largest low wind pressure coefficient region was produced by the Barrel Vault roof configuration and only covered the upper floor. The Gable roof configuration created a small low wind pressure coefficient region that covered a portion of the upper floor while the low wind pressure coefficient region created by the Pyramid roof configuration barely touched the upper floor and missed out the ground floor completely. Thus, the difference in the minimum wind pressure coefficient on the leeward building edge of each roof shapes determined their potential to create the maximum wind pressure coefficient difference.



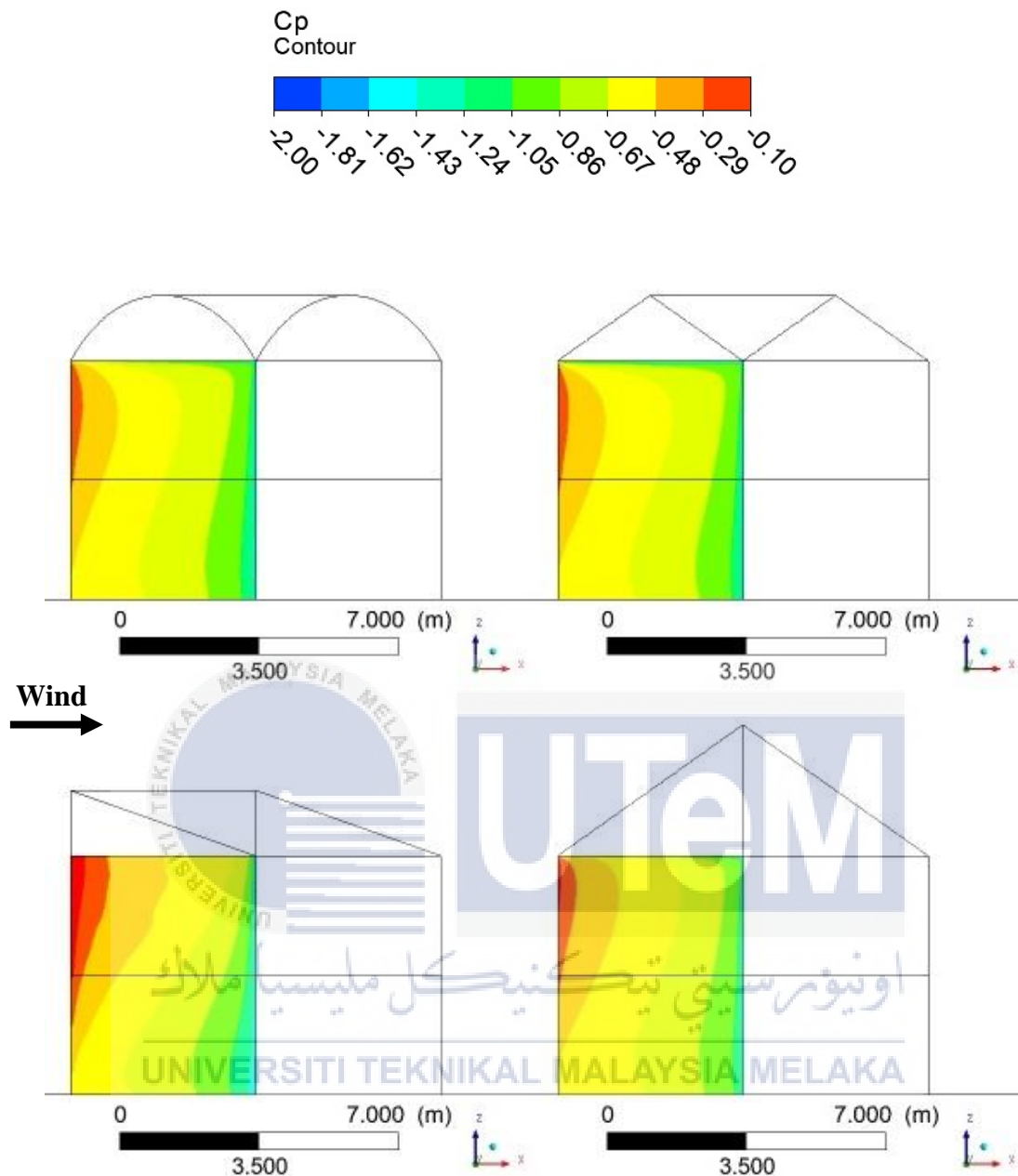


Figure 4.9: The Wind Pressure Coefficient Distribution Contour on the North Facade of Barrel Vault Roof (Top Left), Gable Roof (Top Right), Pyramid Roof (Bottom Left) and Shed Roof (Bottom Right) under 45° Wind Approach Angle.

The maximum pressure coefficient focused on the north façade upper floor windward edge for all roof shapes. Only the Shed roof was able to create significant minimum pressure coefficient when the wind approached from the building edge as seen in Figure 4.9.

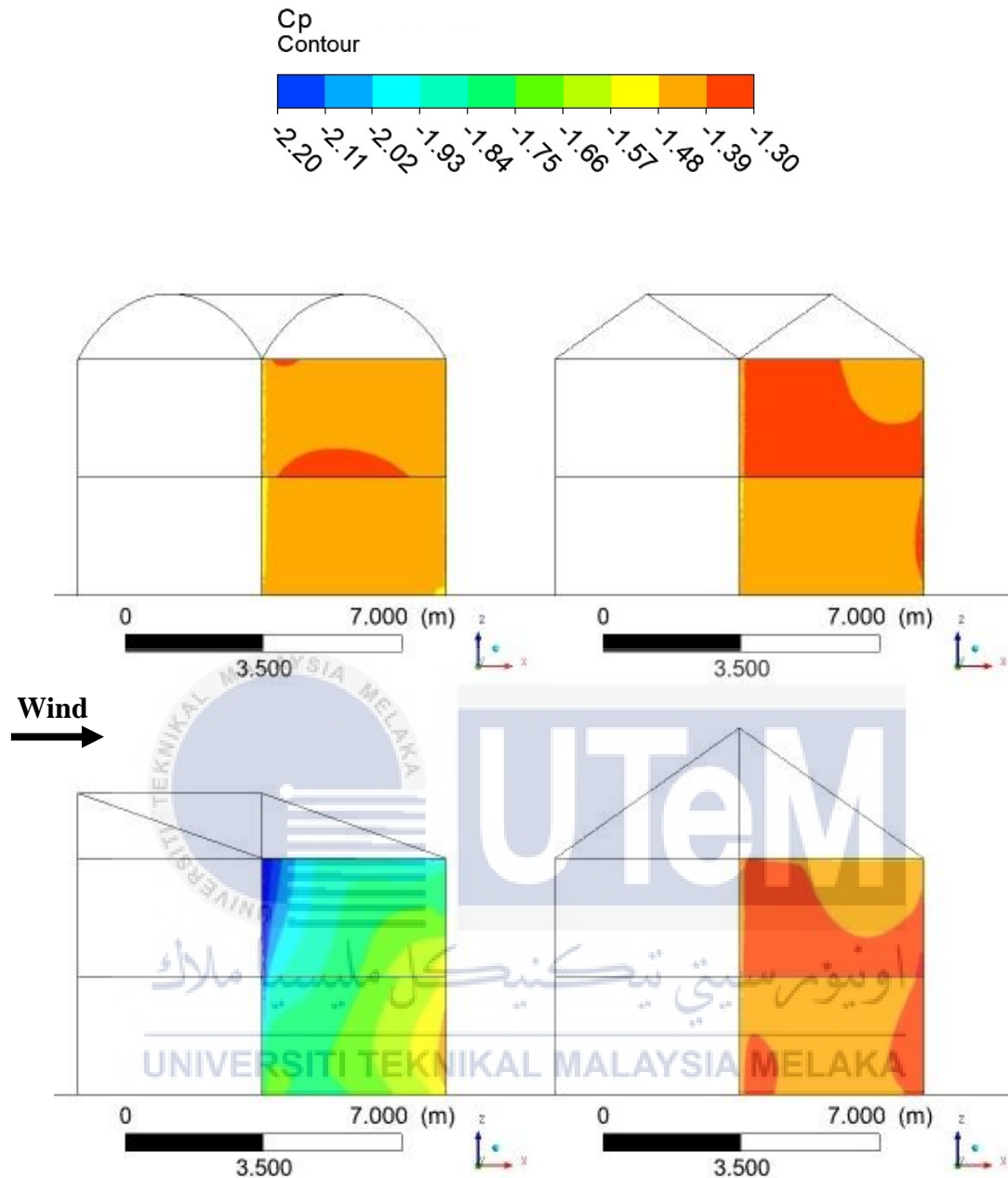


Figure 4.10: The Wind Pressure Coefficient Distribution Contour on the East Facade of Barrel Vault Roof (Top Left), Gable Roof (Top Right), Pyramid Roof (Bottom Left) and Shed Roof (Bottom Right) under 45° Wind Approach Angle.

Only the Shed roof configuration was able to create minimum pressure coefficient on the east façade upper floor as seen in Figure 4.10. The Shed and Barrel Vault roof shapes were not able to generate maximum pressure coefficient unlike the Gable and Pyramid roof.

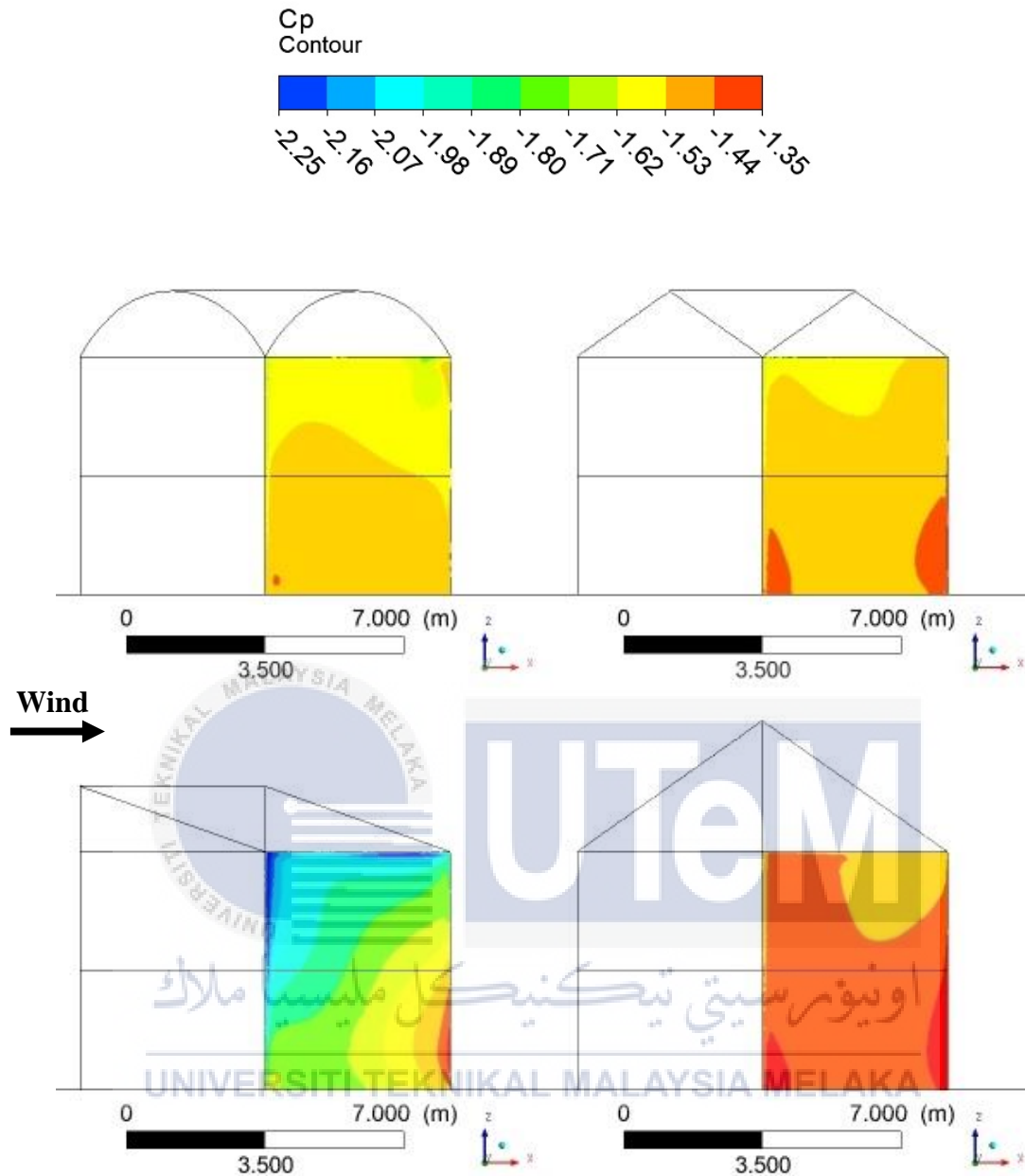


Figure 4.11: The Wind Pressure Coefficient Distribution Contour on the South Facade of Barrel Vault Roof (Top Left), Gable Roof (Top Right), Pyramid Roof (Bottom Left) and Shed Roof (Bottom Right) under 45° Wind Approach Angle.

The asymmetrical roof was able to generate both minimum and maximum pressure coefficients on the South façade of the building model. The fully-symmetrical Pyramid roof was able to create maximum pressure coefficient while both semi-symmetrical roofs, Barrel Vault and Gable struggled to get either maximum or minimum pressure coefficient.

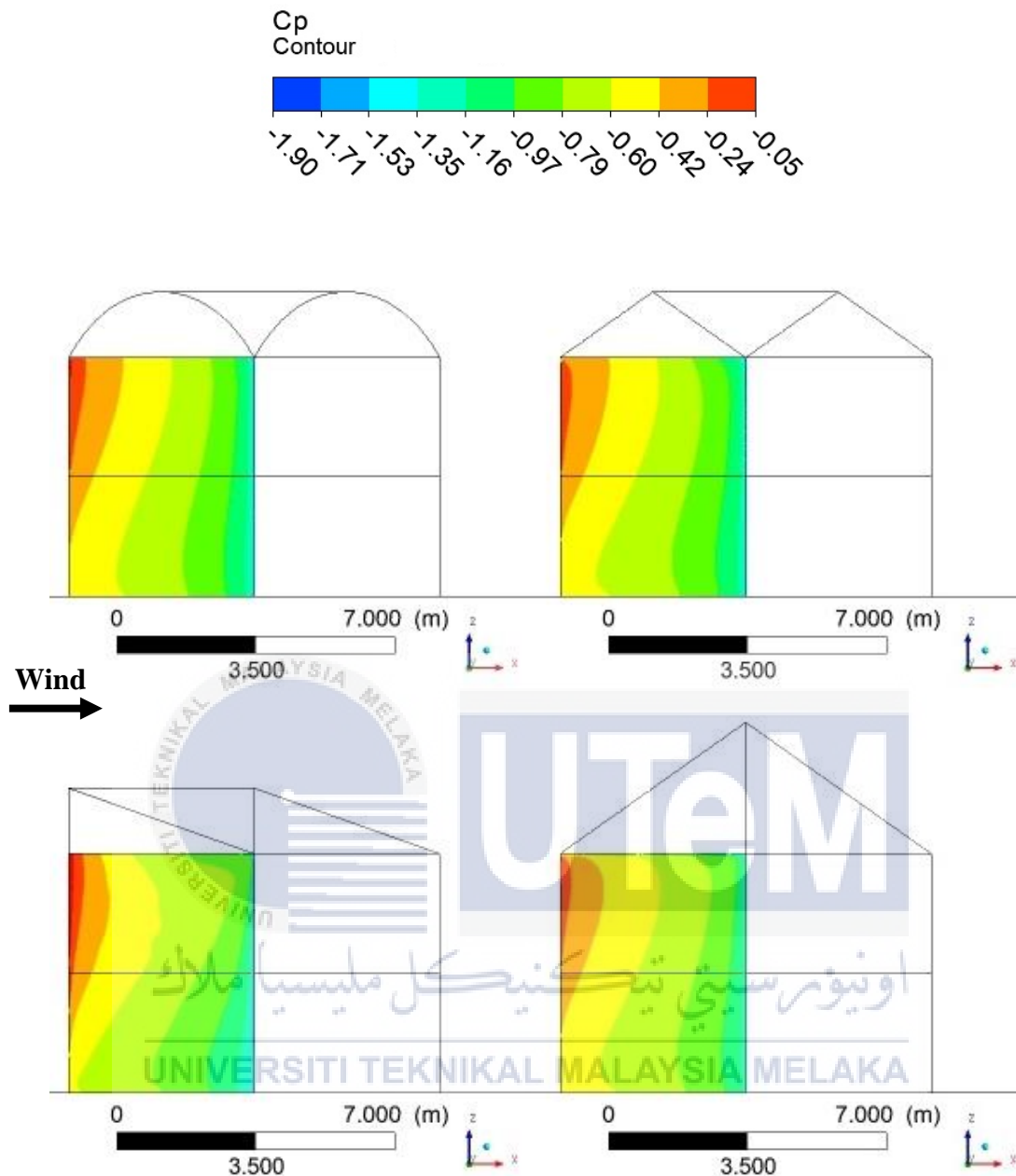


Figure 4.12: The Wind Pressure Coefficient Distribution Contour on the West Facade of Barrel Vault Roof (Top Left), Gable Roof (Top Right), Pyramid Roof (Bottom Left) and Shed Roof (Bottom Right) under 45° Wind Approach Angle.

The west facade was the windward façade in this wind approach direction. Both minimum and maximum pressure coefficients were detected on all roof shapes. There were not any significant difference across different roof configurations.

4.3 DIFFERENCE IN THE WIND PRESSURE COEFFICIENTS BETWEEN OPPOSING FACADES

The wind driven natural ventilation rate is determined by the formula stated in Section 2.1 as shown below:

$$Q_{\text{ventilation}} = U_{\text{wind}} \sqrt{\frac{C_{p1} - C_{p2}}{\frac{1}{A_1^2 \cdot C_1^2} + \frac{1}{A_2^2 \cdot C_2^2}}}$$

Where:

$Q_{\text{ventilation}}$ = wind driven ventilation rate (m³/s)

U_{wind} = wind speed at far-field (m/s)

C_{p1} = coefficient of wind pressure drag at the upstream opening

C_{p2} = coefficient of wind pressure drag at the downstream opening

A_1 = cross sectional area of the inlet (m²)

A_2 = cross sectional area of the outlet (m²)

C_1 = discharge coefficient at the inlet

C_2 = discharge coefficient at the outlet

The U_{wind} , A_1 , A_2 , C_1 and C_2 were assumed as a constant value for all simulation cases. As such, the value of $(C_{p1} - C_{p2})$ was proportional to the wind driven natural ventilation rate, $Q_{\text{ventilation}}$ as shown below. The value of difference in wind pressure coefficients, C_{diff} became the determining factor of the wind driven natural ventilation rate.

$$Q_{\text{ventilation}} \propto (C_{p1} - C_{p2})$$

$$Q_{\text{ventilation}} \propto C_{diff},$$

Where:

$$C_{diff} = (C_{p1} - C_{p2})$$

$$C_p = \frac{P - P_{Wind}}{P_{Wind}}$$

Where:

$$P_{Wind} = \frac{1}{2} \rho (U_{Wind})^2$$

For all roof shapes simulations, cross ventilation did not happen between ground and upper floor. In a typical double storey house, the stair which is the only connecting medium between both floors does not have the capability to generate significant cross ventilation. Hence, both ground and upper floors had their own wind driven natural ventilation rate analysis respectively in this study. Due to the fact that the ventilation rate formula only applies to opposing facades, the building model facades were split into two combinations: North-South (NS) facades and East-West (EW) facades. The data analysis is categorized into two parts: wind approach angle based in Section 4.3.1 and roof shape based in Section 4.3.2 to 4.3.5. Full details of the wind pressure and the coefficient of wind pressure data are listed in Table D1 and D2 in the appendix.

UNIVERSITI TEKNIKAL MALAYSIA MELAKA

4.3.1 Difference in Wind Pressure Coefficient Data for All Roof Shapes in the Average Wind Approach Angle

It is commonly accepted where the natural wind will change its direction from time to time especially during the interchange of the monsoon seasons. It is better to average the wind driven ventilation potential among all eight wind approach angles for the study of inconsistent wind directions condition. The difference in coefficient of wind pressure results are shown in Figure 4.13 and Figure 4.14 respectively. For more details, the difference in wind pressure coefficients, C_{diff} data for 0° , 45° , 90° , 135° , 180° , 225° , 270° and 315° wind approach angles are located in the appendix from Figure D1 to D16.

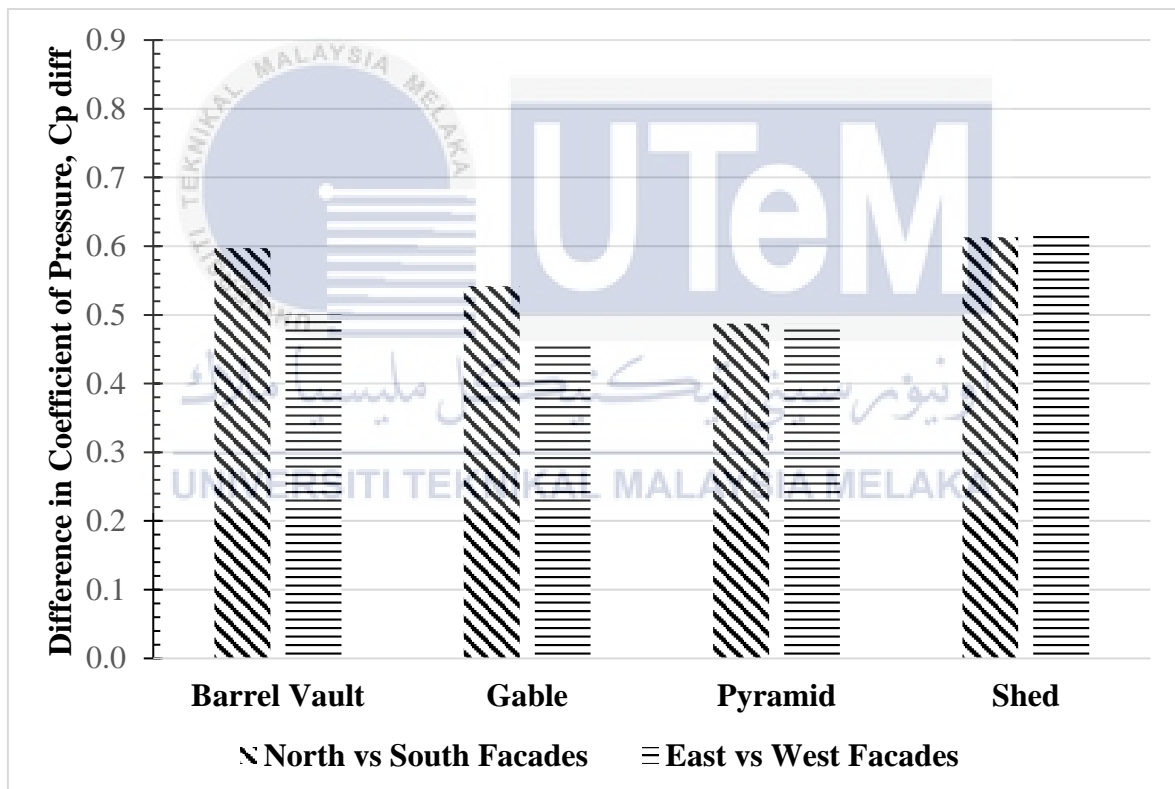


Figure 4.13: Difference in Wind Pressure Coefficients, C_{diff} against the Ground Floor Building Model Façades of Each Roof Shapes at the Average Wind Approach Angle.

On the ground floor, the Shed roof topped the other roofs in ventilation potential either in the North-South or the East-West facades. The Barrel Vault roof came in second,

the Gable roof was the second runner-up while the Pyramid roof came in last. For roof with symmetrical design such as the Barrel Vault and the Gable configurations, they had higher potential in the North-South facades than the East-West facades by at least 19.17%. While for asymmetrical roof shape, then trending was reversed. The Shed configuration had higher potential in the East-West facades than the North-South facades by 1.39%. It is worth to note that the Pyramid roof had same potential in both North-South and East-West facades due to the symmetrical roof shape in all facades. Figure 4.13 shows the difference in wind pressure coefficients, C_{diff} against the ground floor building model façades of each roof shapes at the average wind approach angle.

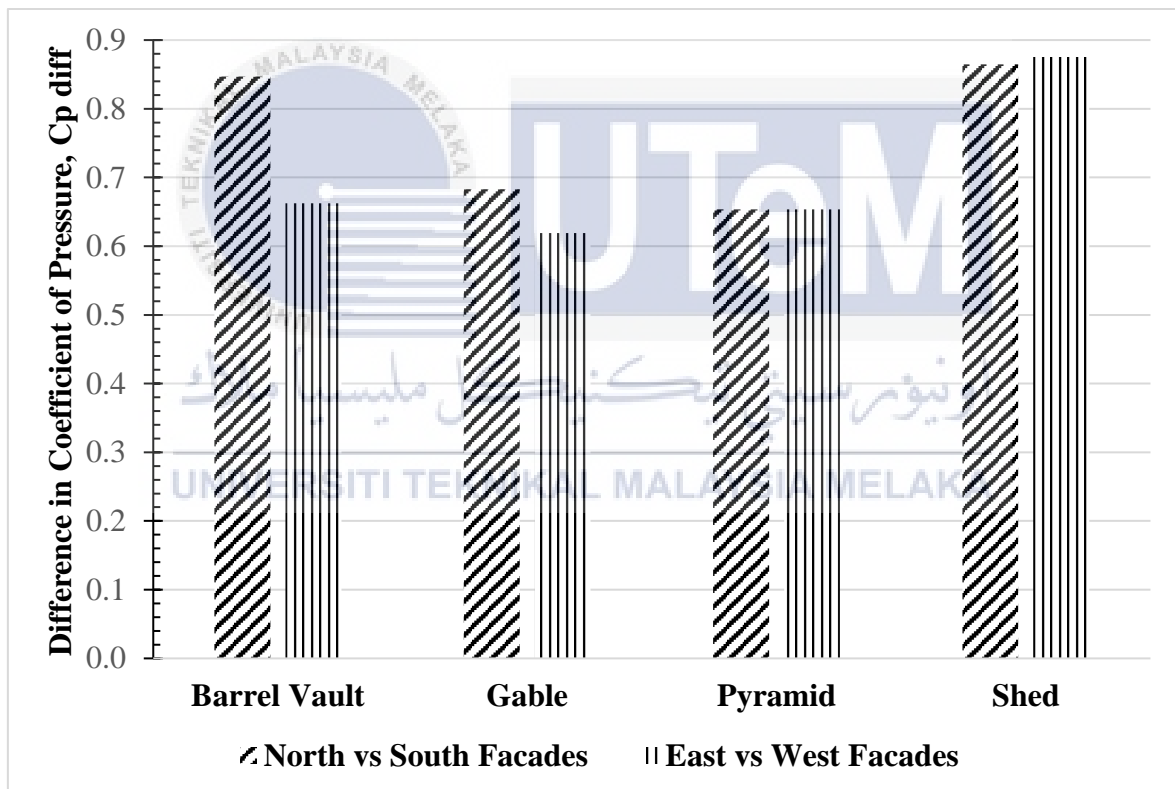


Figure 4.14: Difference in Wind Pressure Coefficients, C_{diff} against the Upper Floor Building Model Façades of Each Roof Shapes at the Average Wind Approach Angle.

On the upper floor, the wind driven natural ventilation potential ranking remained the same trending as in the ground floor. But a higher wind pressure coefficient difference

was recorded in the upper floor compared to the ground floor. The highest and lowest wind pressure coefficients were all concentrated on the upper floor. It was believed that higher distance from ground would receive a more developed air flow, thus creating a larger difference in wind pressure among the opposing facades. Figure 4.14 shows the difference in wind pressure coefficients, C_{diff} against the upper floor building model façades of each roof shapes at the average wind approach angle.

The overall wind driven natural ventilation potential was the highest when asymmetrical roof shape was employed. The shed roof potential proofed this trending with the highest difference in the coefficient of wind pressure for both ground and upper floor. The next best natural ventilation performers were roof shapes symmetrical on two of the four building model facades. Barrel Vault roof and Gable roof both fell into this category. It was observed that the curve roof of Barrel Vault configuration was able to generate higher difference in coefficient of wind pressure than the straight roof of Gable configuration. The worst wind driven ventilation potential was recorded in the Pyramid roof. The symmetry of the roof in all four facades made it hard to create sufficient blockage for huge wind pressure difference between opposing facades.

4.3.2 Difference in Wind Pressure Coefficient Data for Barrel Vault Roof Shapes in the All Wind Approach Angles

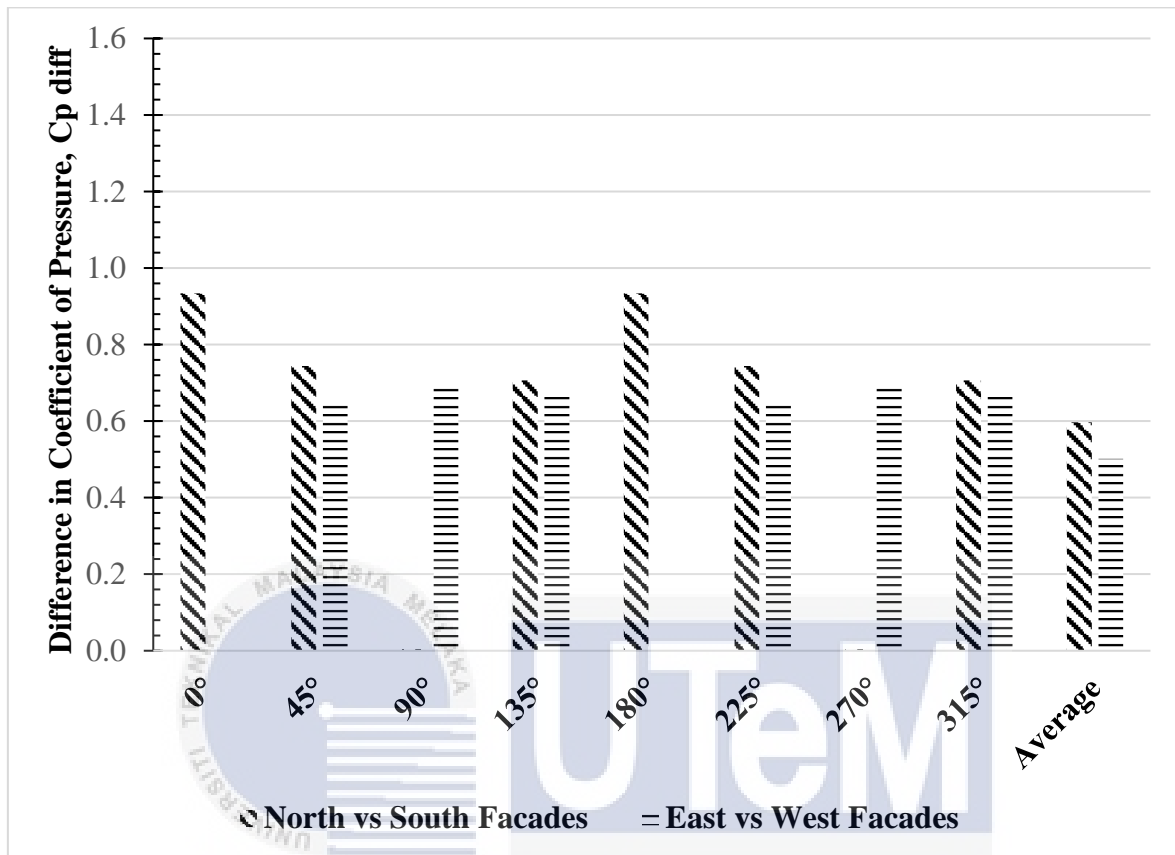


Figure 4.15: Difference in Wind Pressure Coefficients, C_{diff} against All Wind Approach Angles at the Ground Floor Building Model Façades of the Barrel Vault Roof Shape.

On the ground floor, the Barrel Vault roof performed the best when the wind approached from the normal of the building façade. This result can be seen where the North-South facades of the Barrel Vault roof recorded the highest difference values in both 0° and 180° wind approach angles. The lowest potential was recorded in both 45° and 225° wind approach angles where the wind approached the building model from the building edge. Figure 4.15 shows the difference in wind pressure coefficients, C_{diff} against all wind approach angle at the ground floor building model façades of the Barrel Vault roof shape.

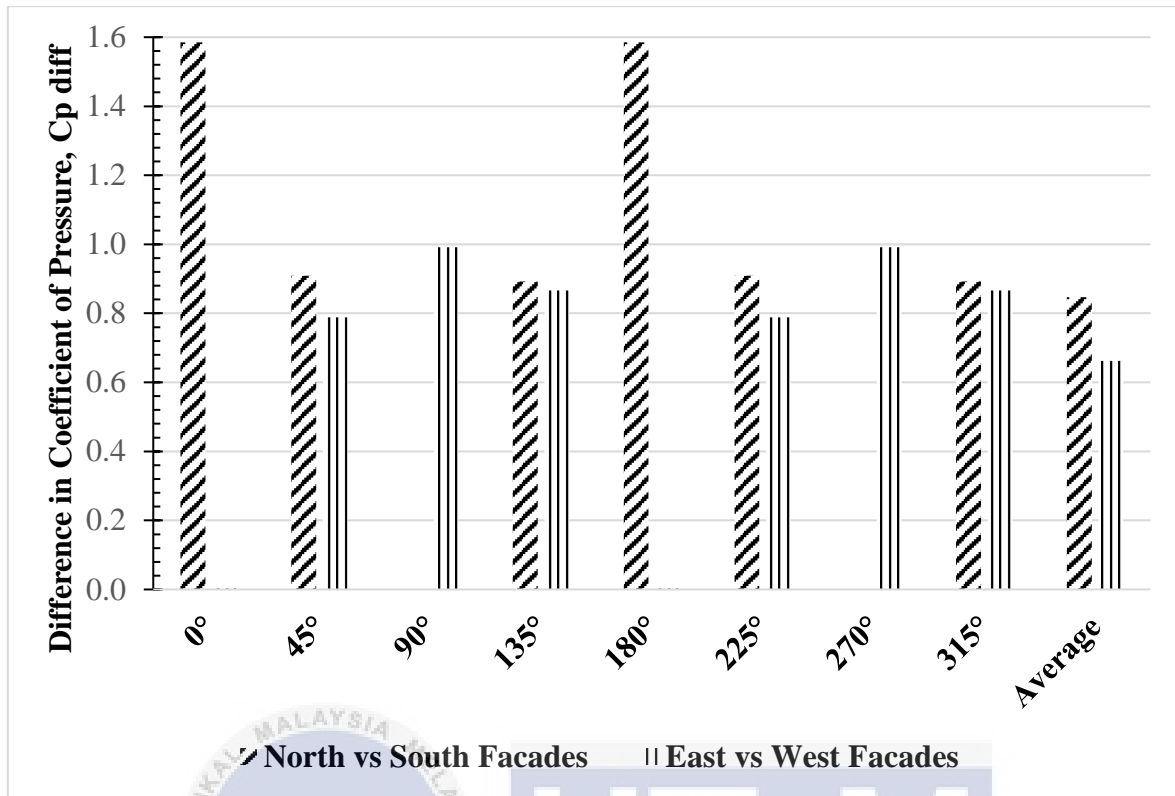


Figure 4.16: Difference in Wind Pressure Coefficients, C_{diff} against All Wind Approach Angles at the Upper Floor Building Model Façades of the Barrel Vault Roof Shape.

On the upper floor, the wind driven natural ventilation potential trending showed the same as in the ground floor. But a higher wind pressure coefficient difference was recorded in the upper floor compared to the ground floor. The highest and lowest wind pressure coefficients were all concentrated on the upper floor. It was believed that higher distance from ground would receive a more developed air flow, thus creating a larger difference in wind pressure among the opposing facades. Figure 4.16 shows the difference in wind pressure coefficients, C_{diff} against all wind approach angle at the upper floor building model façades of the Barrel Vault roof shape.

It was observed that semi-symmetry Barrel Vault roof had the highest wind driven natural ventilation potential on either ground or upper floor when the wind approached in a

direction normal to the building façade. The North-South facades typically had higher wind pressure coefficient difference than the East-West facades in most of the wind approach angles. The difference in roof height across the North-South facades believed to have contributed to the better potential.

4.3.3 Difference in Wind Pressure Coefficient Data for Gable Roof Shapes in the All Wind Approach Angles

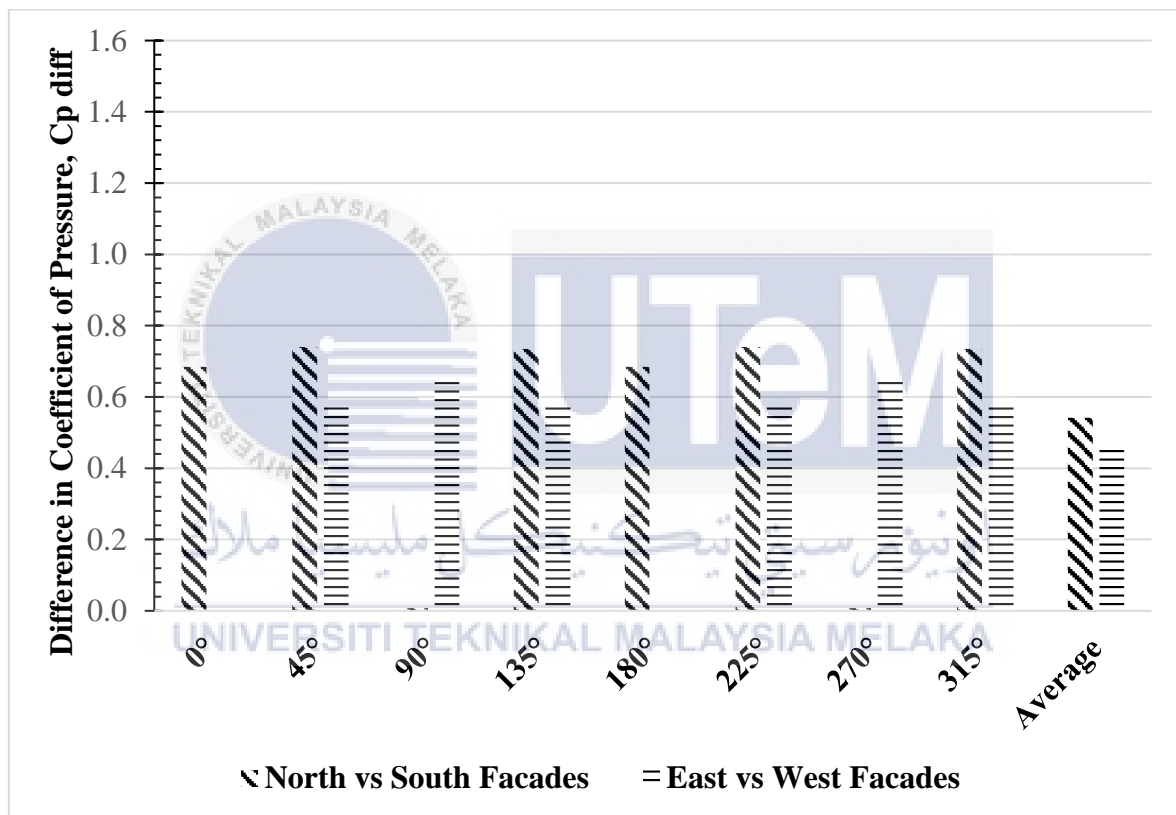


Figure 4.17: Difference in Wind Pressure Coefficients, C_{diff} against All Wind Approach Angles at the Ground Floor Building Model Façades of the Gable Roof Shape.

On the ground floor, the Gable roof performed the best when the wind approached from the normal of the building façade. This result can be seen where the North-South facades of the Gable roof recorded the highest difference values in both 0° and 180° wind approach angles. The lowest potential was recorded in both 45° and 225° wind approach

angles where the wind approached the building model from the building edge. Figure 4.17 shows the difference in wind pressure coefficients, C_{diff} against all wind approach angle at the ground floor building model façades of the Gable roof shape.

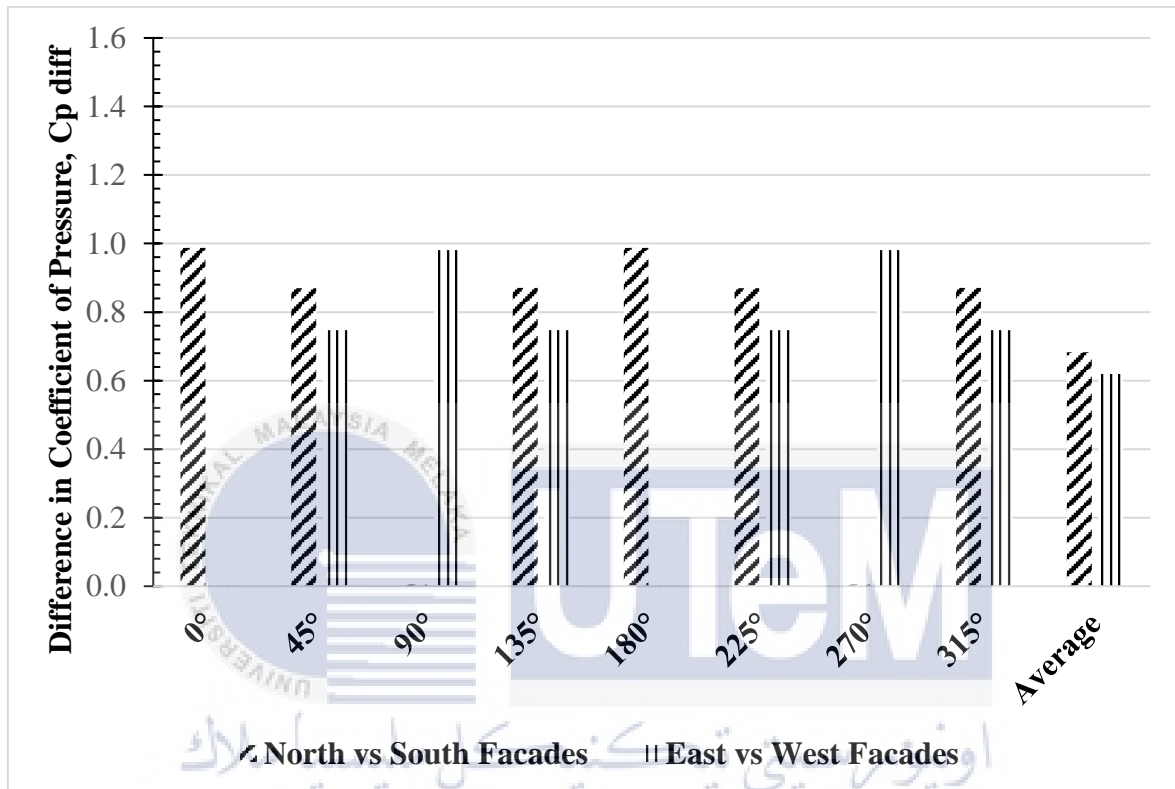


Figure 4.18: Difference in Wind Pressure Coefficients, C_{diff} against All Wind Approach Angles at the Upper Floor Building Model Façades of the Gable Roof Shape.

On the upper floor, the wind driven natural ventilation potential topped when the wind approach angle was normal to the façade and dropped when wind approached from the building edges. A higher wind pressure coefficient difference was recorded in the upper floor compared to the ground floor same as the case in Barrel Vault roof. Figure 4.18 shows the difference in wind pressure coefficients, C_{diff} against all wind approach angle at the upper floor building model façades of the Gable roof shape.

It was observed that semi-symmetry Gable roof had the highest wind driven natural ventilation potential on either ground or upper floor when the wind approached in a direction normal to the building façade. The North-South facades typically had higher wind pressure coefficient difference than the East-West facades in most of the wind approach angles. The difference in roof height across the North-South facades believed to have contributed to the better potential.

4.3.4 Difference in Wind Pressure Coefficient Data for Pyramid Roof Shapes in the All Wind Approach Angles

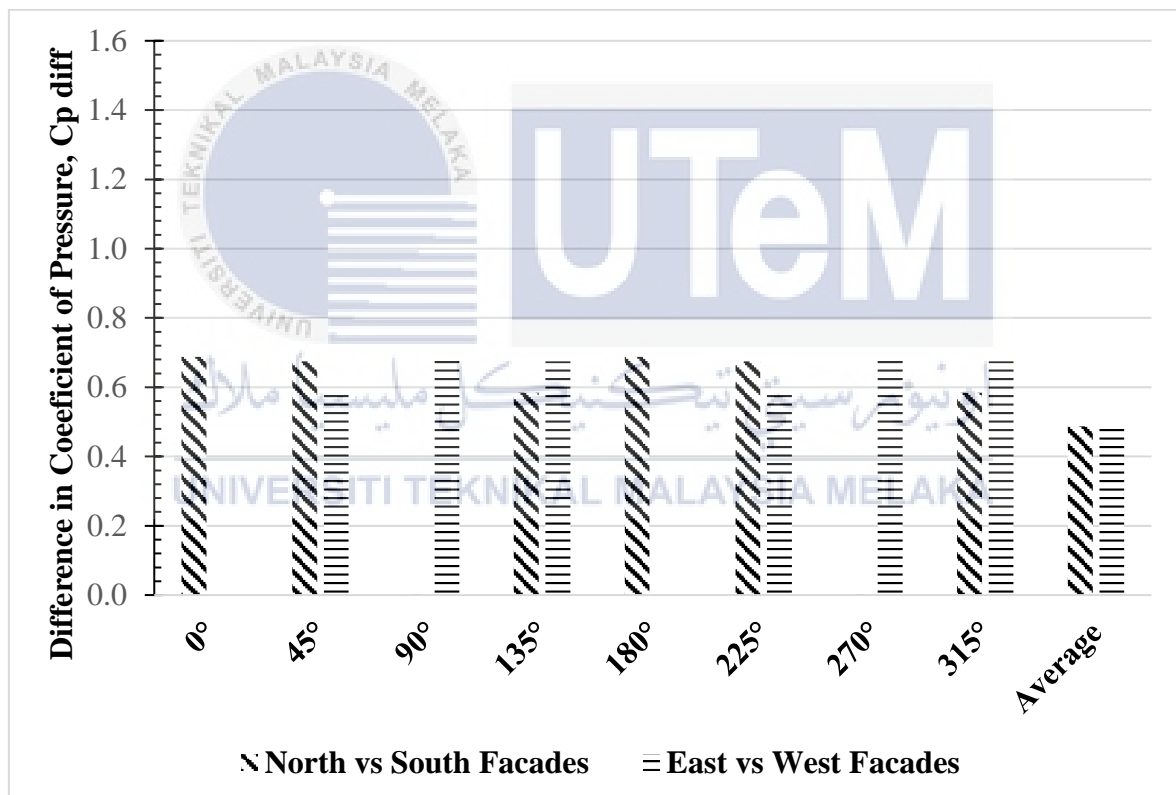


Figure 4.19: Difference in Wind Pressure Coefficients, C_{diff} against All Wind Approach Angles at the Ground Floor Building Model Façades of the Pyramid Roof Shape.

On the ground floor, the Pyramid roof performed equally across different wind approach angles. The North-South facades combination and the East-West facades

combination had equal chance of generating the same maximum wind pressure coefficient difference. Figure 4.19 shows the difference in wind pressure coefficients, C_{diff} against all wind approach angle at the ground floor building model façades of the Pyramid roof shape.

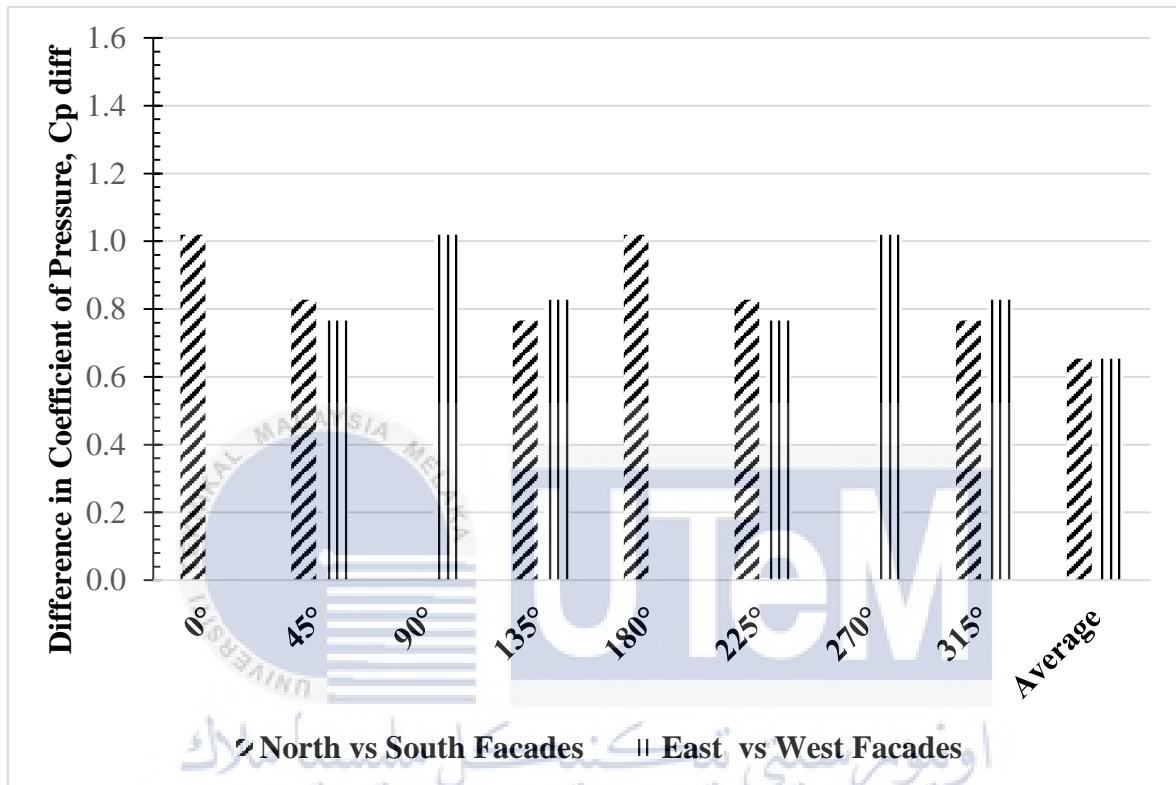


Figure 4.20: Difference in Wind Pressure Coefficients, C_{diff} against All Wind Approach Angles at the Upper Floor Building Model Façades of the Pyramid Roof Shape.

On the upper floor, the wind driven natural ventilation potential trending showed the same as in the ground floor. But a higher wind pressure coefficient difference was recorded in the upper floor compared to the ground floor same as the case in Barrel Vault roof. Figure 4.20 shows the difference in wind pressure coefficients, C_{diff} against all wind approach angle at the upper floor building model façades of the Pyramid roof shape.

It was observed that full-symmetry Pyramid roof had the most balanced wind driven natural ventilation potential on either ground or upper floor in either wind approach angles. Both North-South facades and East-West facades induced a similar wind pressure coefficient difference. Due to the symmetry roof shapes in all facades, the Pyramid roof was unable to create large wind pressure difference and ended up in the worst wind driven natural ventilation potential in this study.

4.3.5 Difference in Wind Pressure Coefficient Data for Shed Roof Shapes in the All Wind Approach Angles

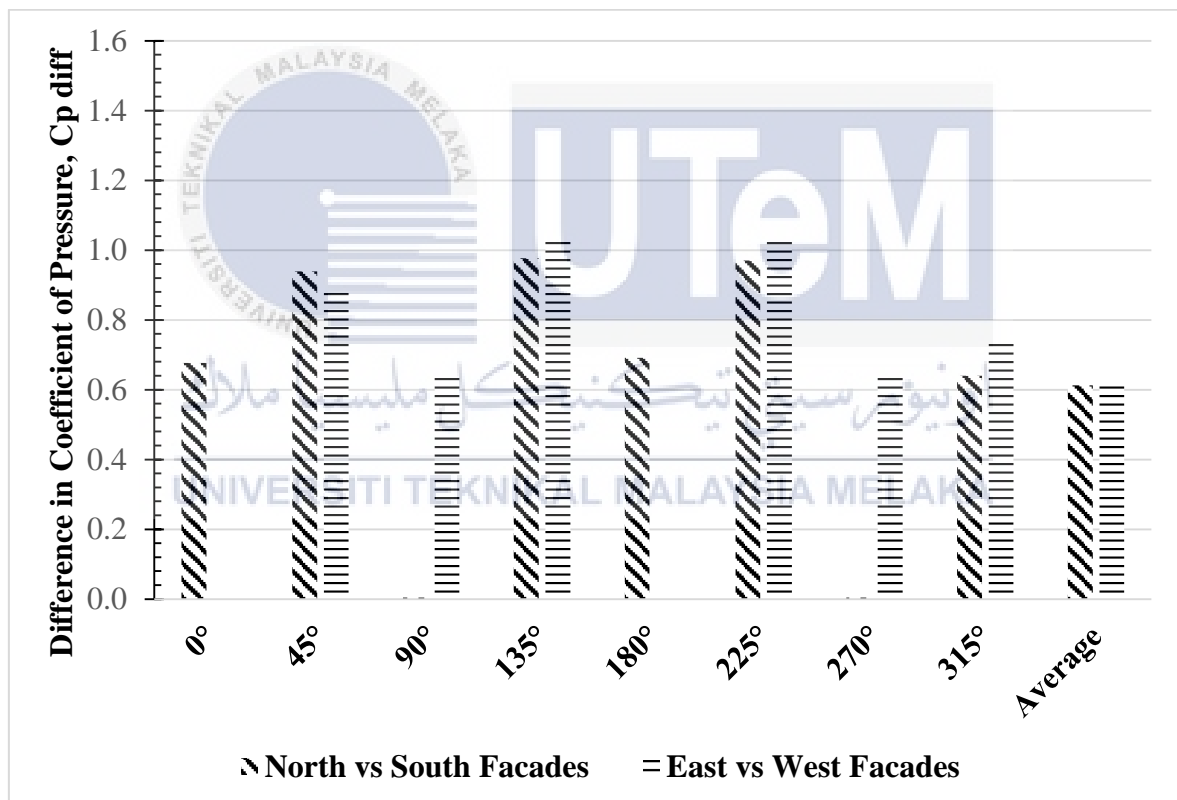


Figure 4.21: Difference in Wind Pressure Coefficients, C_{diff} against All Wind Approach Angles at the Ground Floor Building Model Façades of the Shed Roof Shape.

On the ground floor, the Shed roof performed the best when the wind approached from the building edge. This result can be seen where the East-West facades of the Shed roof

recorded the highest difference values in both 135° and 225° wind approach angles. The lowest potential was recorded in both 90° and 270° wind approach angles where the wind approach angle were normal to the building façade. Figure 4.21 shows the difference in wind pressure coefficients, C_{diff} against all wind approach angle at the ground floor building model façades of the Shed roof shape.

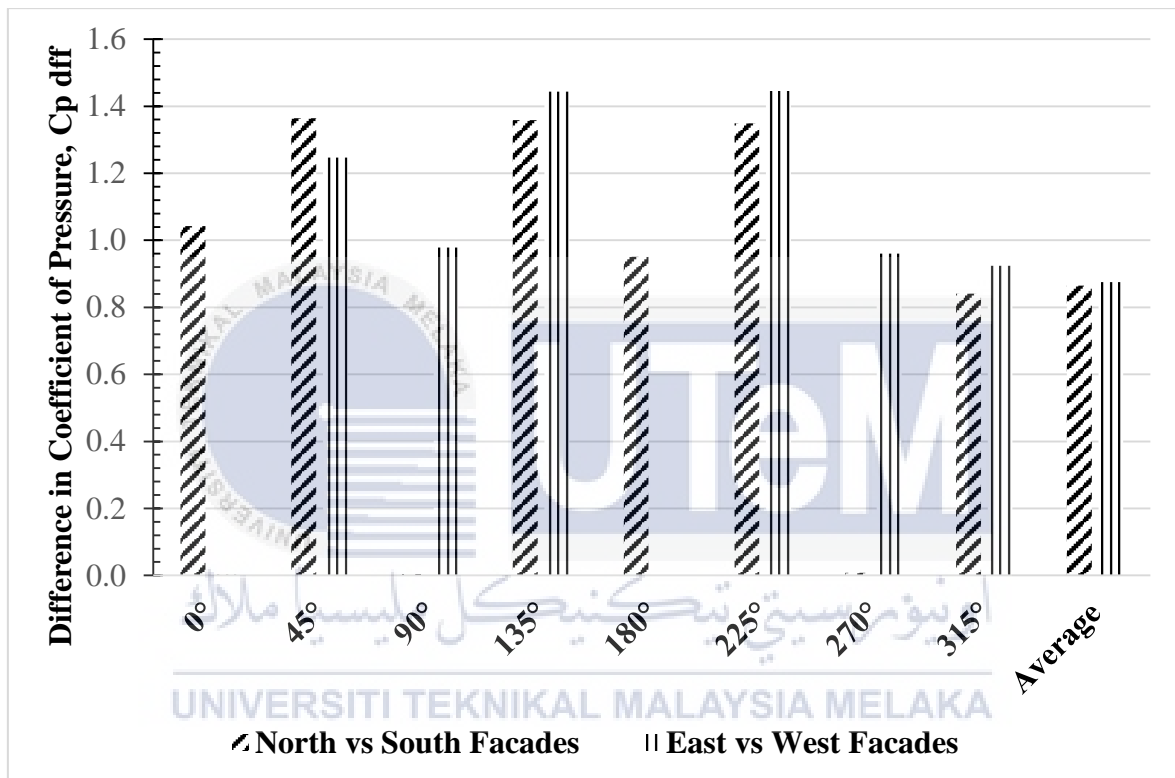


Figure 4.22: Difference in Wind Pressure Coefficients, C_{diff} against All Wind Approach Angles at the Upper Floor Building Model Façades of the Shed Roof Shape.

On the upper floor, the wind driven natural ventilation potential trending showed the same as in the ground floor. But a higher wind pressure coefficient difference was recorded in the upper floor compared to the ground floor same as the case in Barrel Vault roof. Figure 4.22 shows the difference in wind pressure coefficients, C_{diff} against all wind approach angle at the upper floor building model façades of the Shed roof shape.

It was observed that asymmetry Shed roof had the highest wind driven natural ventilation potential on either ground or upper floor when the wind approach direction was on the building edge. The East-West facades typically had higher wind pressure coefficient difference than the North-South facades in most of the wind approach angles.



CHAPTER 5

CONCLUSION AND RECOMMENDATION

5.1 CONCLUSION

The natural ventilation potential of a building is strongly influenced by the roof shape. In general, the Shed roof had the highest natural ventilation potential, the Barrel Vault roof came in second, followed by the Gable roof and lastly, the Pyramid roof. It was observed that asymmetrical roof shape was able to induce better ventilation potential than the symmetrical roof shape. Apart from that, curved roof surface had higher natural ventilation potential than the flat roof surface. As a conclusion, an asymmetrical roof shape with a curved surface shall be chosen in order to achieve the highest natural ventilation potential during the roof design process.

5.2 RECOMMENDATIONS

This study only focused only on determining the cross ventilation among opposing facades. Future studies are encouraged to determine the potential of cross ventilation among adjacent facades because some housing units in the high rise buildings may only have the option of cross ventilation through adjacent facades. If the most suitable roof shape can be identified, it will have huge impact on a large group of population and benefit the energy conservation effort. The weather conditions shall be one of the interesting field to study in future. The temperature and humidity of air may influence the rate and the pattern of the cross ventilation. All the recommendations suggested are hopefully be able to provide future researchers to create a more detailed and beneficial study on this topic.

REFERENCES

- Afshin, M., Sohankar, A., Dehghan Manshadi, M. and Kazemi Esfeh, M. (2016). An experimental study on the evaluation of natural ventilation performance of a two-sided wind-catcher for various wind angles. *Elsevier. Renewable Energy* 85 (2016). 1068-1078.
- Ahepp. (2017). What is laminar flow?. *Simwiki. SimScale CAE Forum*. Retrieved from <https://www.simscale.com/forum/t/what-is-laminar-flow/70247>
- ANSI/ASHRAE. (2013). Ventilation for acceptable indoor air quality. *ASHRAE.org*, ANSI/ASHRAE Addendum p to ANSI/ASHRAE Standard 62.1 (2013), 1-10.
- ASHRAE. (2016). The standards for ventilation and indoor air quality. *ASHRAE.org*, Standards 62.1 & 62.2. Retrieved from <https://www.ashrae.org/resources--publications/bookstore/standards-62-1--62-2>
- Aynsley, R. (2007). Natural ventilation in passive design. *BEDP Environment, Design Guide*, Tec 2 (2007), 1-12.
- Bastide, A., Lauret, P., Garde, F. and Boyer, H. (2006). Building energy efficiency and thermal comfort in tropical climates. presentation of a numerical approach for predicting the percentage of well-ventilated living spaces in buildings using natural ventilation. *Elsevier. Energy and Buildings* 38 (2006), 1093-1103.

Bengtson, H. and Stonecypher, L. (2010). Pipe flow calculations 2: Reynolds number and laminar & turbulent flow. *Brighthubengineering.com*. Civil Engineering, Hydraulics. Retrieved from <http://www.brighthubengineering.com/hydraulics-civil-engineering/55053-pipe-flow-calculations-2-reynolds-number-and-laminar-and-turbulent-flow/>

Benson, T. (2014). Reynolds number. *National Aeronautics and Space Administration*. Glenn Research Center. Retrieved from <https://www.grc.nasa.gov/www/k-12/airplane/reynolds.html>

Briney, A. (2017). Winds and the pressure gradient force. *ThoughtCo*. Humanities, Geography. Retrieved from <https://www.thoughtco.com/winds-and-the-pressure-gradient-force-1434440>

Burnett, J., Bojic, M., and Yik, F. (2005). Wind-induced pressure at external surfaces of a high-rise residential building in hong kong. *Elsevier*. Building and Environment 40 (2005), 765-777.

Cheng, S. Y. (2007). The effect of building shape modification on wind pressure differences for cross-ventilation of a low-rise building. *Department of Thermal-Fluid*, Faculty of Mechanical Engineering, Kolej Universiti Teknikal Kebangsaan Malaysia, 1-12.

Chu, C., Lan, T., Tasi, R., Wu, T. and Yang, C. (2017). Wind-driven natural ventilation of greenhouse with vegetation. *Elsevier*. Biosystems Engineering 164 (2017), 221-234.

- Da Graca, G. C. and Linden, P. (2016). Ten questions about natural ventilation of non-domestic buildings. *Building and Environment* (2016).
- Hall, N. (2015). Boundary layer. *National Aeronautics and Space Administration*. Glenn Research Center. Retrieved from <https://www.grc.nasa.gov/www/k-12/airplane/boundlay.html>
- Hoxey R. P. and Richards P. J. (1993). Flow patterns and pressure field around a full-scale building. *Elsevier. Journal of Wind Engineering and Industrial Aerodynamics*, 50 (1993), 203-212.
- Iasfunda. (2017). Circulation: pressure, vertical and horizontal distribution. *Iasfunda.com*. Geography. Retrieved from <http://www.iasfunda.com/2017/03/17/atmospheric-circulation-pressure-vertical-and-horizontal-distribution/>
- Kikumoto, H., Ooka, R., Sugawara, H. and Lim, J. (2017). Observational study of power-law approximation of wind profiles within an urban boundary layer for various wind conditions. *Elsevier. Journal of Wind Engineering and Industrial Aerodynamics* 164 (2017). 13-21.
- Kralik, J., Konecna, L. and Lavrincikova, D. (2017). Experimental validation of computer fluid dynamics simulation aimed on pressure distribution on gable roof of low-rise building. *Elsevier. Procedia Engineering* 190 (2017). 337-384.

- Kubota, T. and Ahmad, S. (2006). Wind environment evaluation of neighborhood areas in major towns of Malaysia. *Journal of Asian Architecture and Building Engineering*, vol.5 no.1 (2006), 1-8.
- Lei, Z., Liu, C., Wang, L. and Li, N. (2017). Effect of natural ventilation on indoor air quality and thermal comfort in dormitory during winter. *Elsevier, Building and Environment* 125 (2017), 240-247.
- Linden, P. F. (1999). The fluid mechanics of natural ventilation. *Department of Applied Mechanics and Engineering Sciences*, University of California, 31 (1999), 201-238.
- Lucas, J. (2014). What is fluid dynamics. *Livescience*. Tech. Retrieved from <https://www.livescience.com/47446-fluid-dynamics.html>
- Norhidayah, A., Lee, C., Azhar, M.K. and Nurulwahida, S. (2013). Indoor air quality and sick building syndrome in three selected buildings. *Elsevier, Procedia Engineering* 53 (2013), 93-98.
- Oliveira, P. J. and Younis, B. A. (2000). On the prediction of turbulent flows around full-scale buildings. *Elsevier, Journal of Wind Engineering and Industrial Aerodynamics* 86 (2000), 203-220.
- Omrani, S., Garcia-Hansen, V., Capra, B. R. and Drogemuller, R. (2017). Effect of natural ventilation mode on thermal comfort and ventilation performance: full-scale measurement. *Elsevier, Energy and Buildings* 156 (2017), 1-16

Peren, J.I., Van Hooff, T., Ramponi, R., Blocken, B. and Leite, B.C.C. (2015). Impact of roof geometry of an isolated leeward sawtooth roof building on cross-ventilation: straight, concave, hybrid or convex?. *Elsevier. J. Wind Eng. Ind. Aerodyn.* 145 (2015), 102-114.

Ramakrishna, M. (2011). Elements of computational fluid dynamics. *Golden Jubilee Publication*. Department of Aerospace Engineering, Indian Institute of Technology Madras, 1-614.

Reis, M. L. C. C., Falcao Filho, J. B. P., Basso, E. and Caldas, V. R. (2015). Pressure coefficient evaluation on the surface of the sonda iii model tested in the ttp pilot transonic wind tunnel. *Journal of Physics: Conference Series*, 588 (2015), 012003, 1-16.

Schulze, T. and Eicker, U. (2013). Controlled natural ventilation for energy efficient buildings. *Elsevier, Energy and Buildings* 56 (2013), 221-232.

Spiru, P. and Simona, P. L. (2017). A review on interactions between energy performance of the building, outdoor air pollution and the indoor air quality. *Elsevier, Energy Procedia* 128 (2017), 179-186.

Tiwari, P. (n.d.). Atmospheric pressure: measurement, distribution and controlling factors. *Geographynotes.com*. Atmosphere. Retrieved from <http://www.geographynotes.com/atmosphere/atmospheric-pressure-measurement-distribution-and-controlling-factors/854>

Tominaga, Y., Akabayashi, S., Kitahara, T. and Arinami, Y. (2015). Air flow around isolated gable-roof buildings with different roof pitches: wind tunnel experiments and cfd simulations. *Elsevier, Building and Environment* 84 (2015), 204-213.

Trinh, K. T. (2010). On the critical Reynolds number for transition from laminar to turbulent flow. *Institute of Food Nutrition and Human Health. Massey University*, 1-39.

Walker, A. (2016). Natural ventilation. *Whole Building Design Guide*, National Institute of Building Sciences. Retrieved from <http://www.wbdg.org/resources/natural-ventilation>

Woodford, C. (2017). Aerodynamics: an introduction. *Explainthatstuff.com*. Science, Aerodynamics. Retrieved from <http://www.explainthatstuff.com/aerodynamics.html>

Versteeg H. K. and Malalasekera W. (1995). Introduction to computational fluid dynamics: the finite volume method. *Harlow. Longman Scientific & Technical*.

APPENDIX A

PSM Gantt Chart

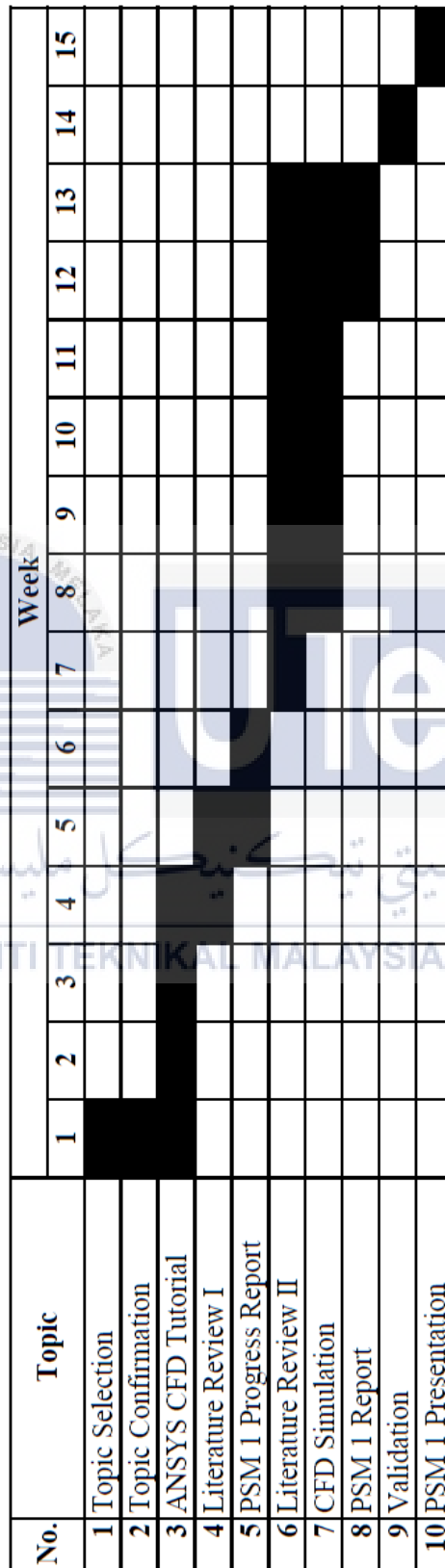


Figure A1: PSM 1 Gantt Chart

APPENDIX A

No.	Topic	Week															
		1	2	3	4	5	6	7	8	9	10	11	12	13	14	15	
1	Verification																
2	CFD Simulation																
3	PSM 2 Progress Report																
4	CFD Simulation																
5	PSM 2 Final Report																
6	PSM 2 Presentation																

Figure A2: PSM 2 Gantt Chart

APPENDIX B

Methodology Flowchart

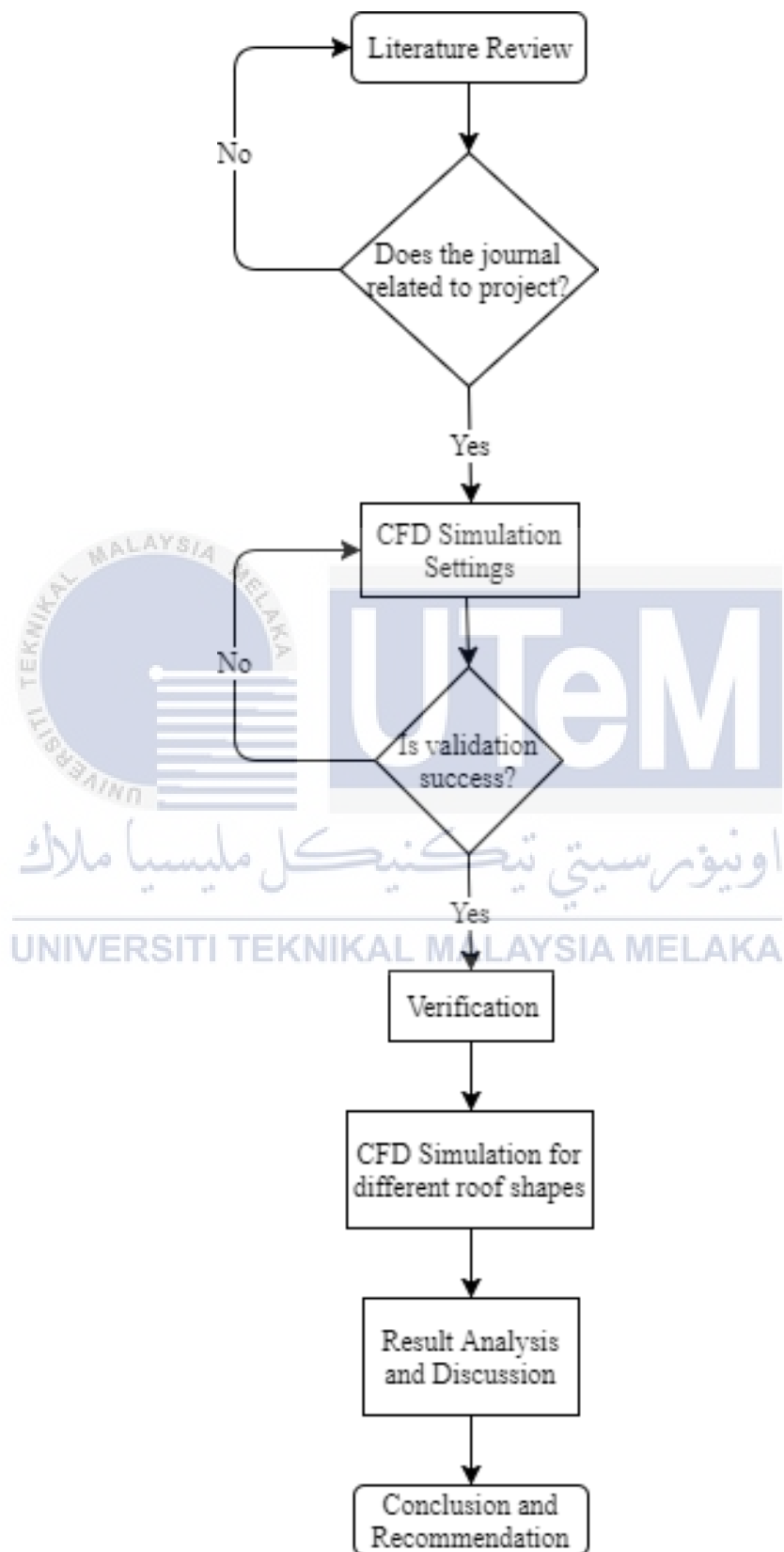


Figure B1: Flowchart of General Methodology

APPENDIX C

Wind Velocity Profile

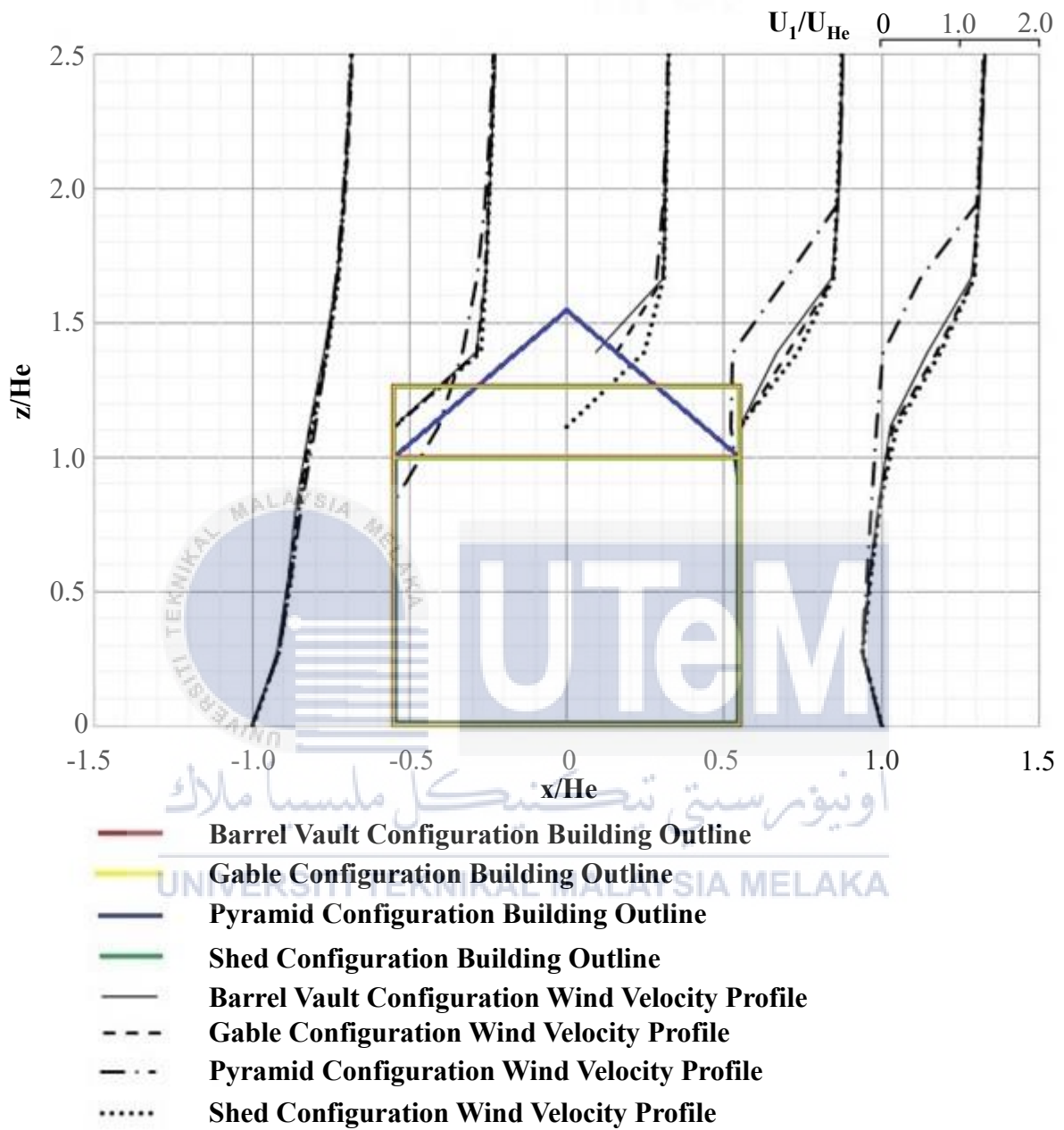


Figure C1: The Wind Velocity Profile of Each Roof Shapes on 90° Wind Approach Angle.

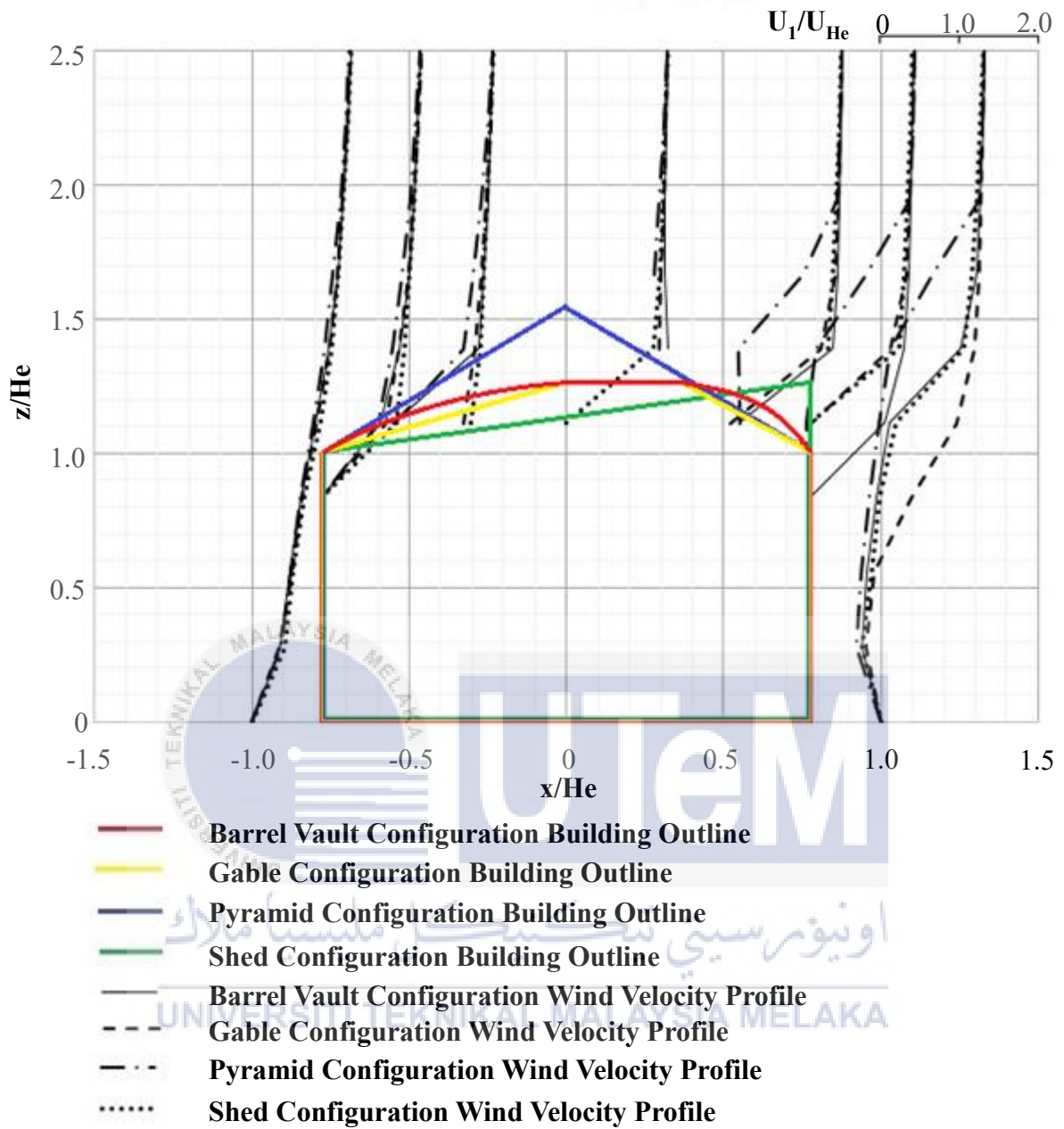


Figure C2: The Wind Velocity Profile of Each Roof Shapes on 135° Wind Approach Angle.

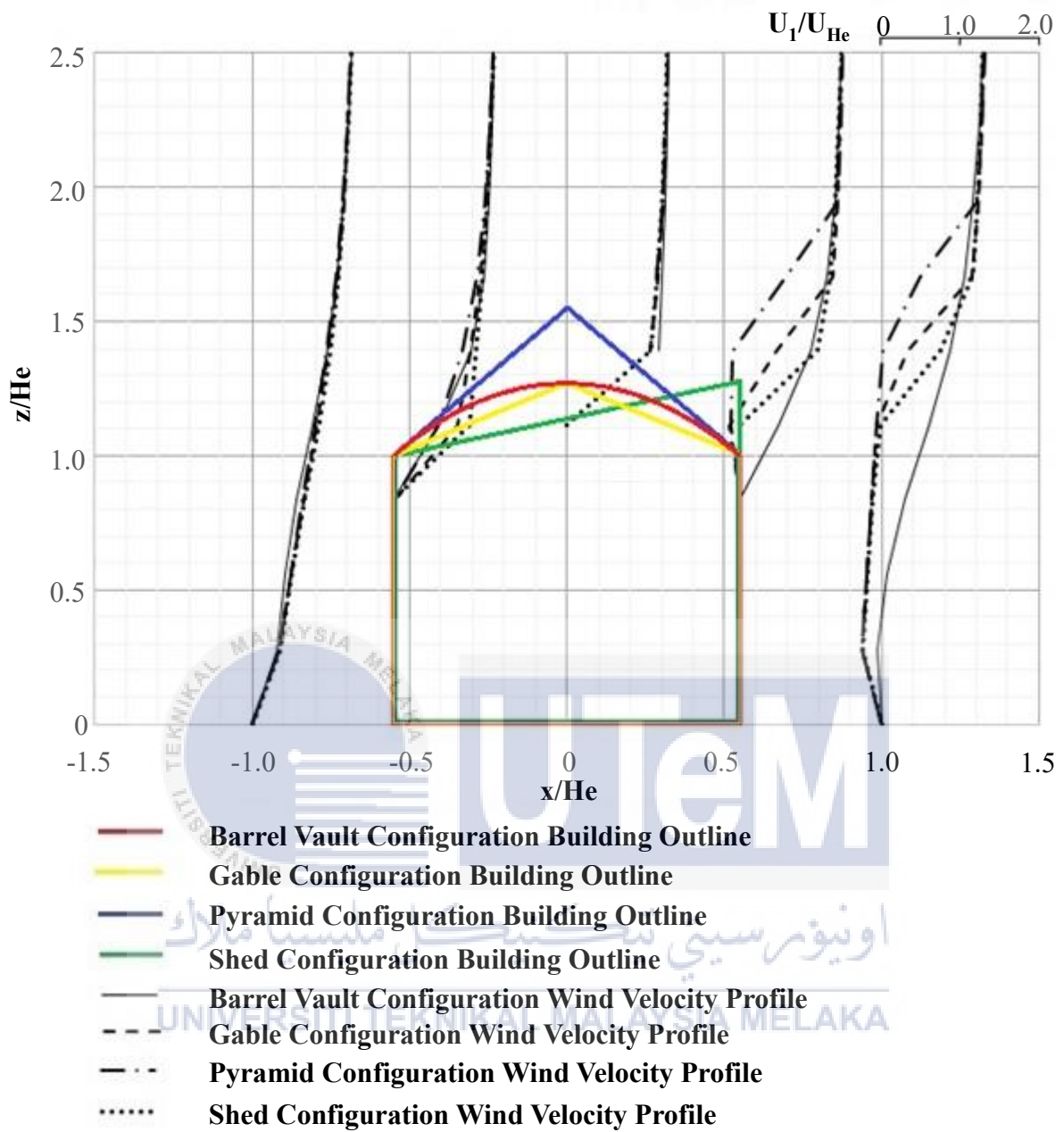


Figure C3: The Wind Velocity Profile of Each Roof Shapes on 180° Wind Approach Angle.

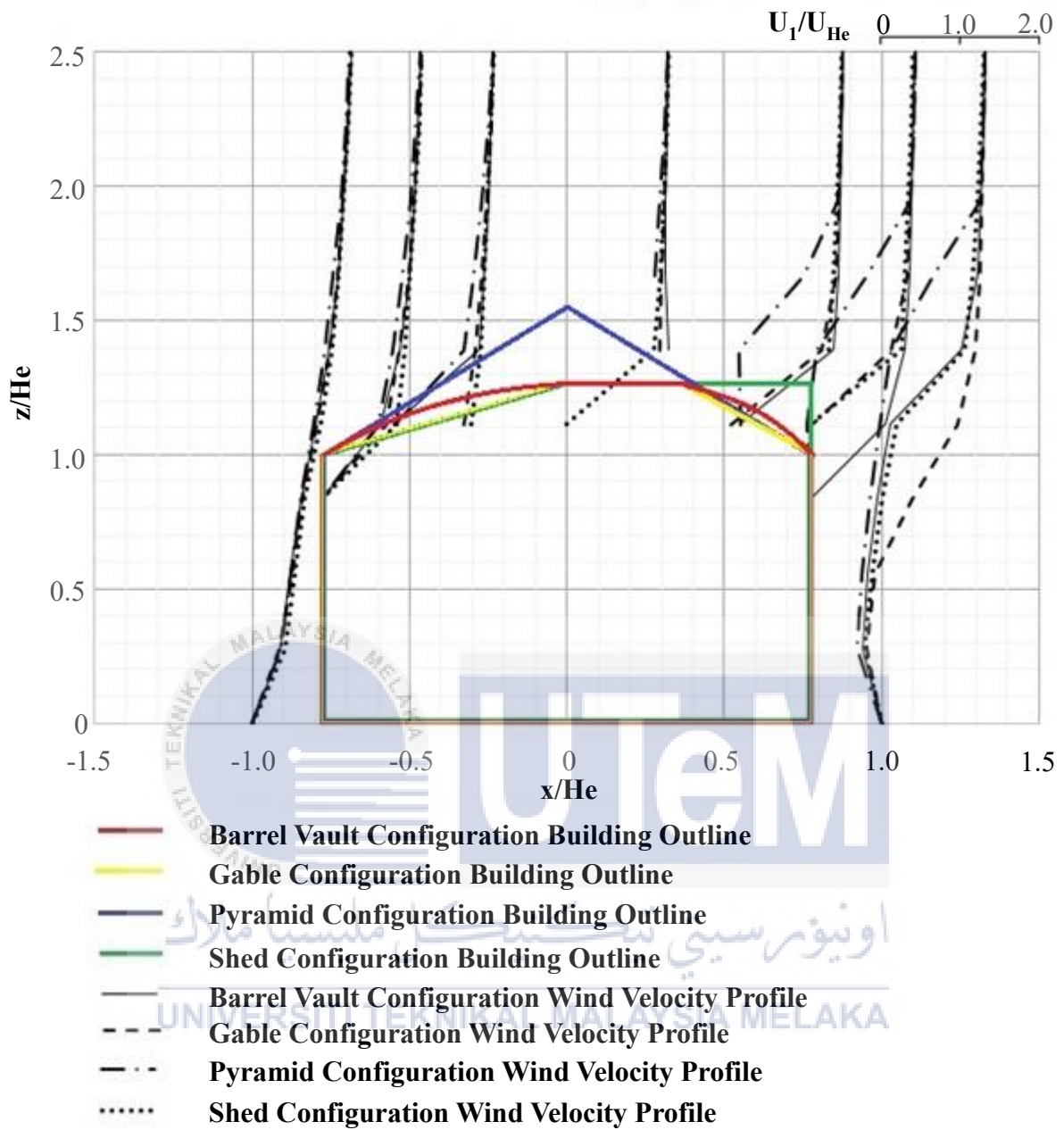


Figure C4: The Wind Velocity Profile of Each Roof Shapes on 225° Wind Approach Angle.

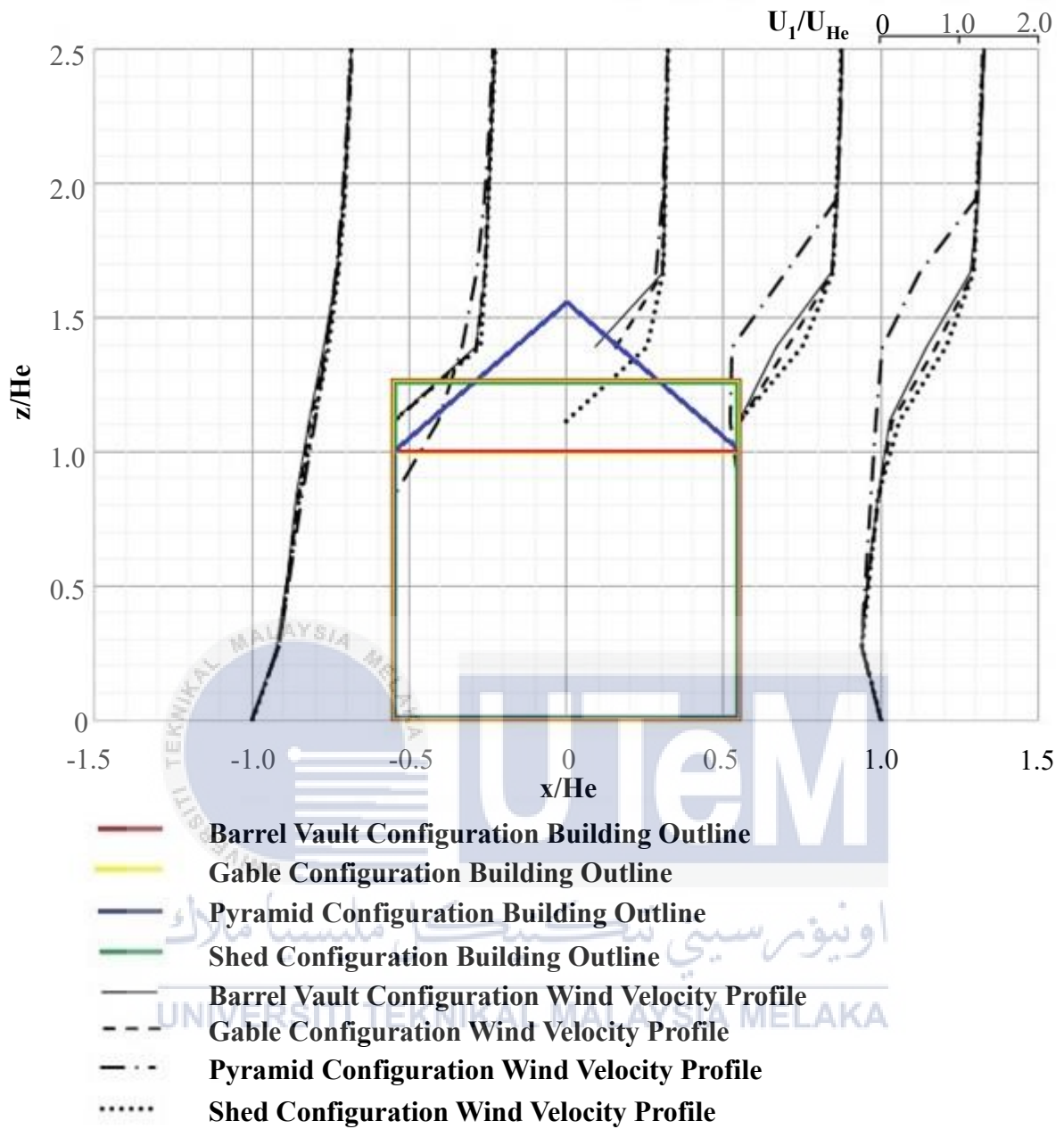


Figure C5: The Wind Velocity Profile of Each Roof Shapes on 270° Wind Approach Angle.

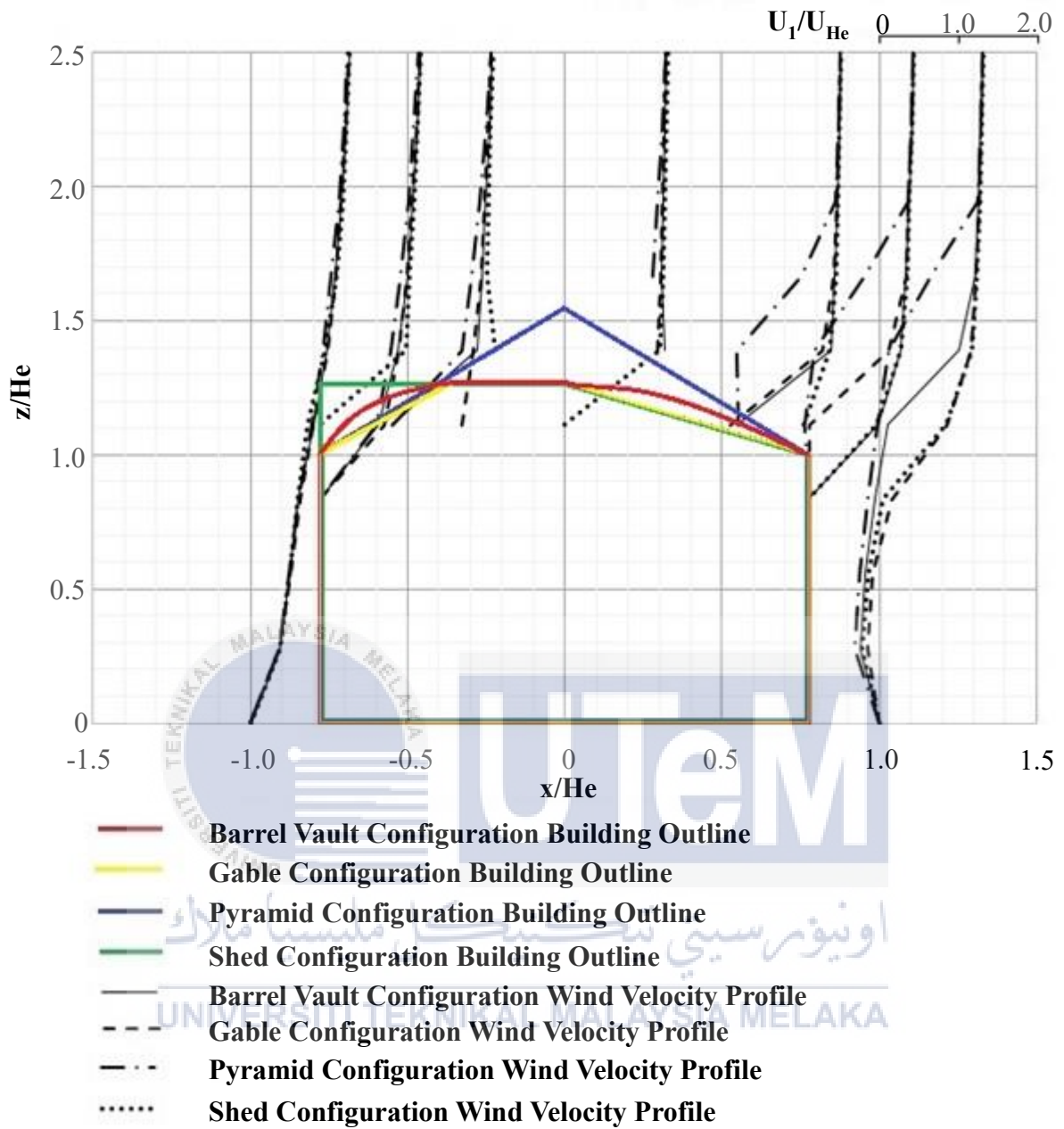


Figure C6: The Wind Velocity Profile of Each Roof Shapes on 315° Wind Approach Angle.

APPENDIX D

Difference in Coefficient of Wind Pressure

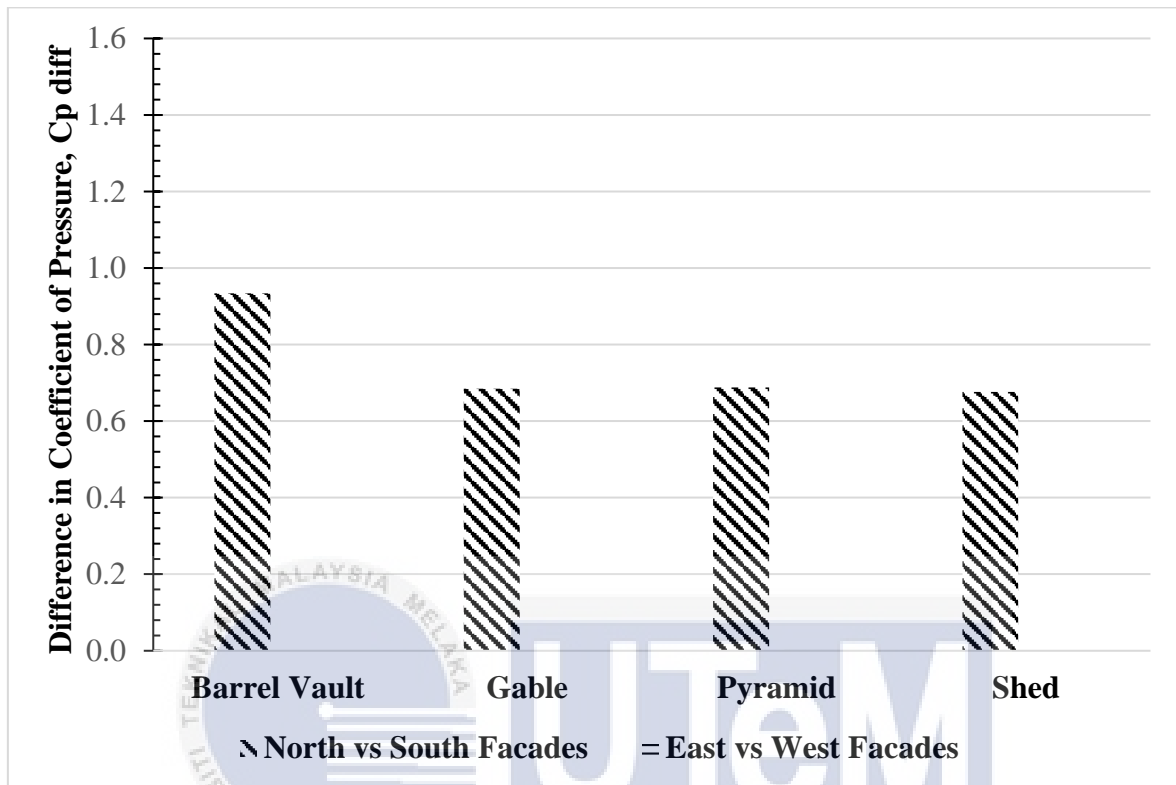


Figure D1: Difference in Wind Pressure Coefficients, C_{diff} against the Ground Floor

Building Model Façades of Each Roof Shapes at the 0° Wind Approach Angle.

UNIVERSITI TEKNIKAL MALAYSIA MELAKA

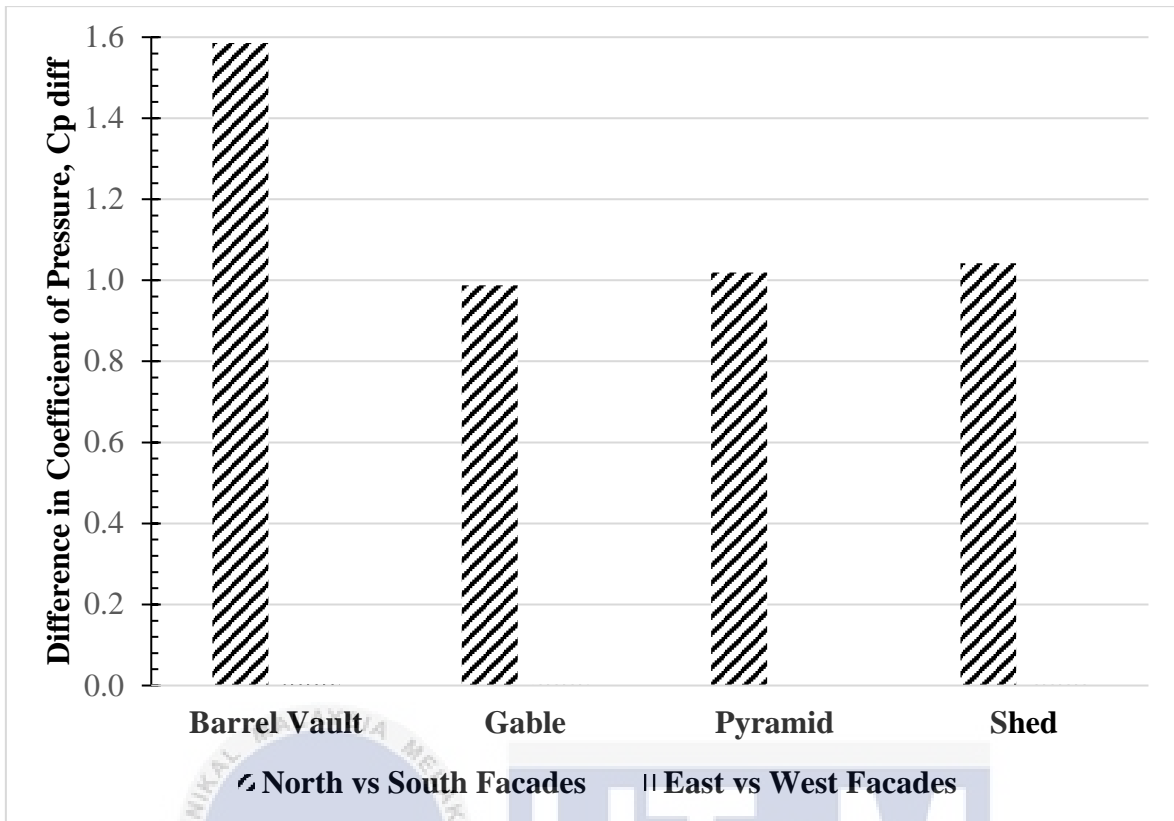


Figure D2: Difference in Wind Pressure Coefficients, C_{diff} against the Upper Floor Building Model Façades of Each Roof Shapes at the 0° Wind Approach Angle.

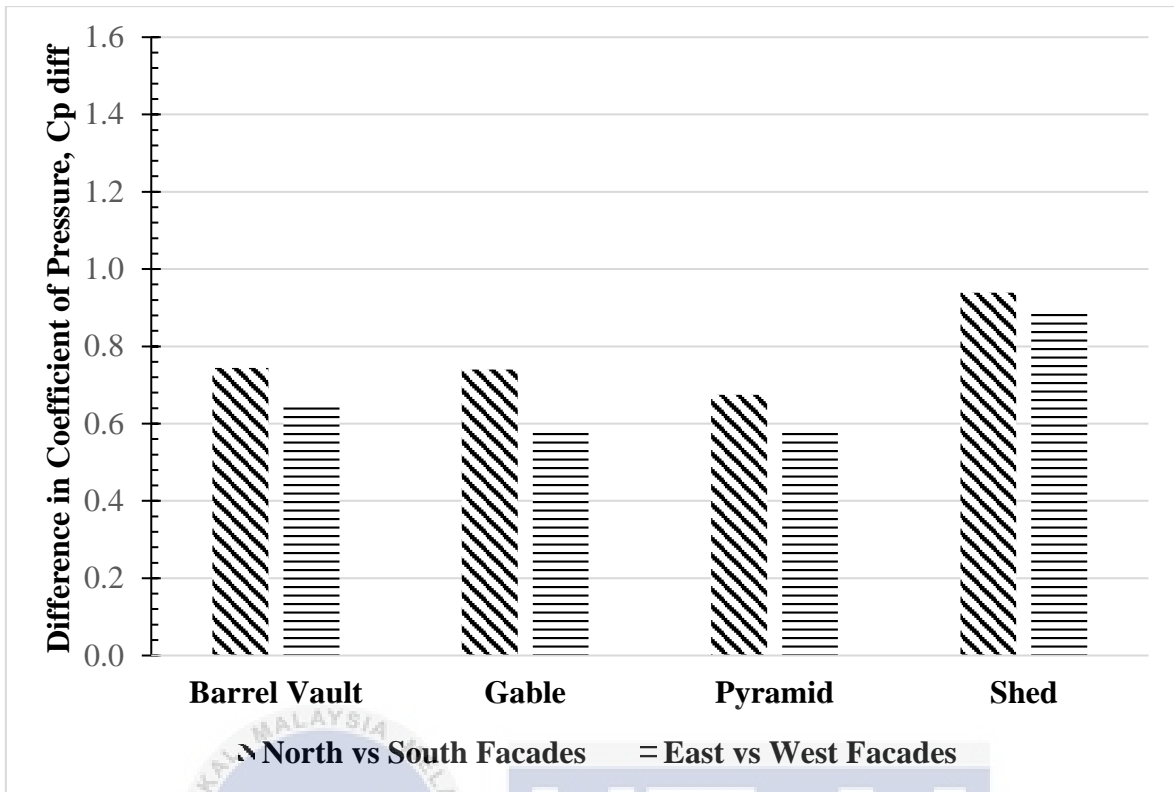


Figure D3: Difference in Wind Pressure Coefficients, C_{diff} against the Ground Floor Building Model Façades of Each Roof Shapes at the 45° Wind Approach Angle.

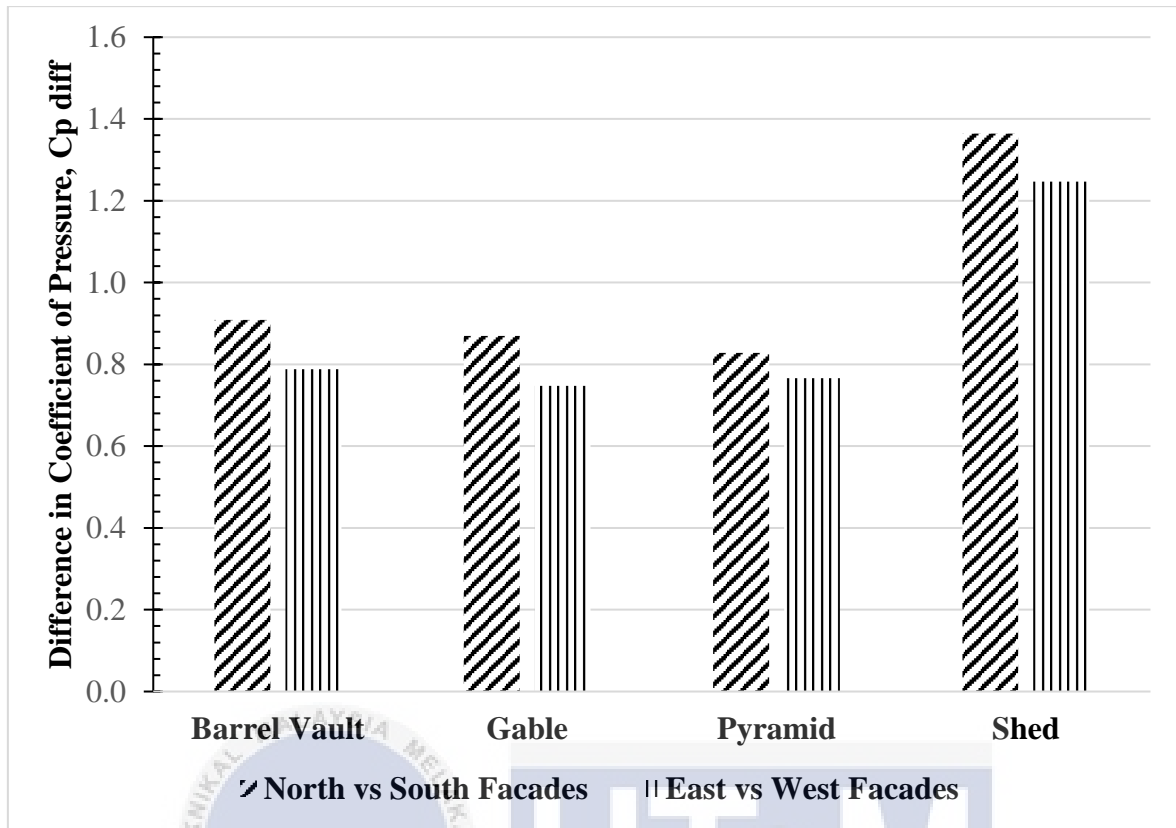


Figure D4: Difference in Wind Pressure Coefficients, C_{diff} against the Upper Floor Building Model Façades of Each Roof Shapes at the 45° Wind Approach Angle.

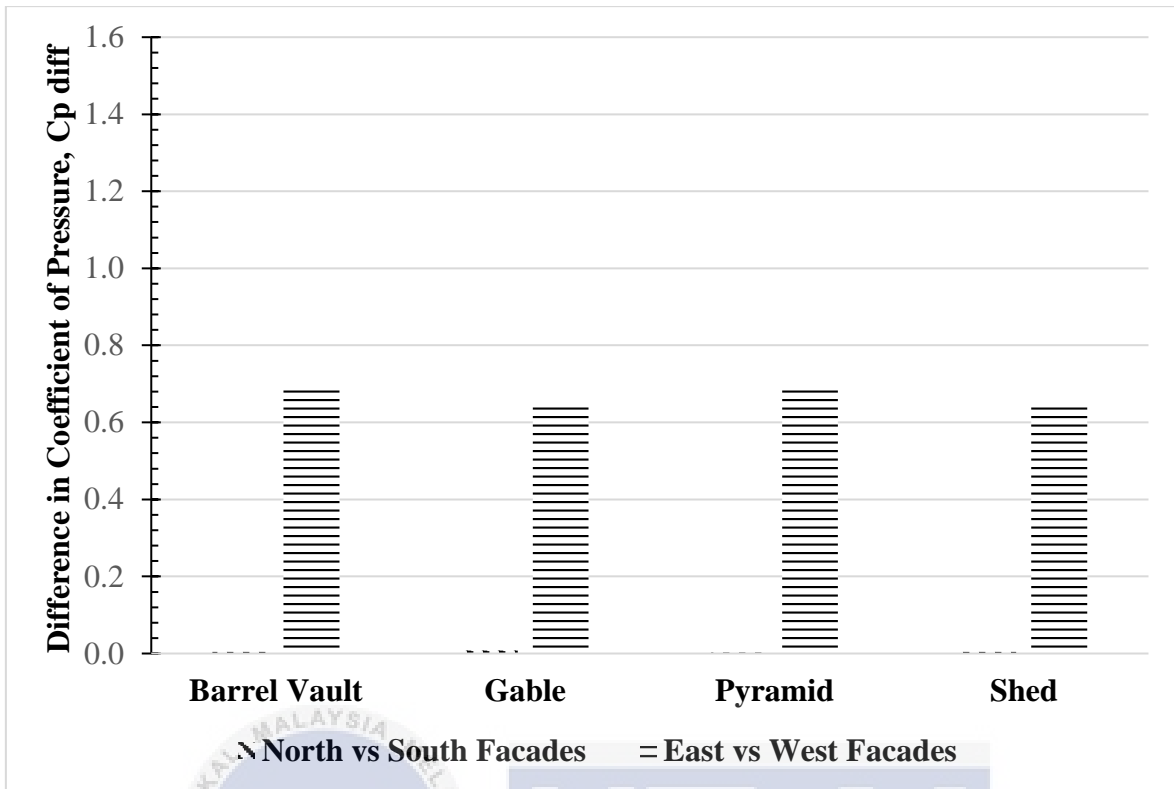


Figure D5: Difference in Wind Pressure Coefficients, C_{diff} against the Ground Floor Building Model Façades of Each Roof Shapes at the 90° Wind Approach Angle.

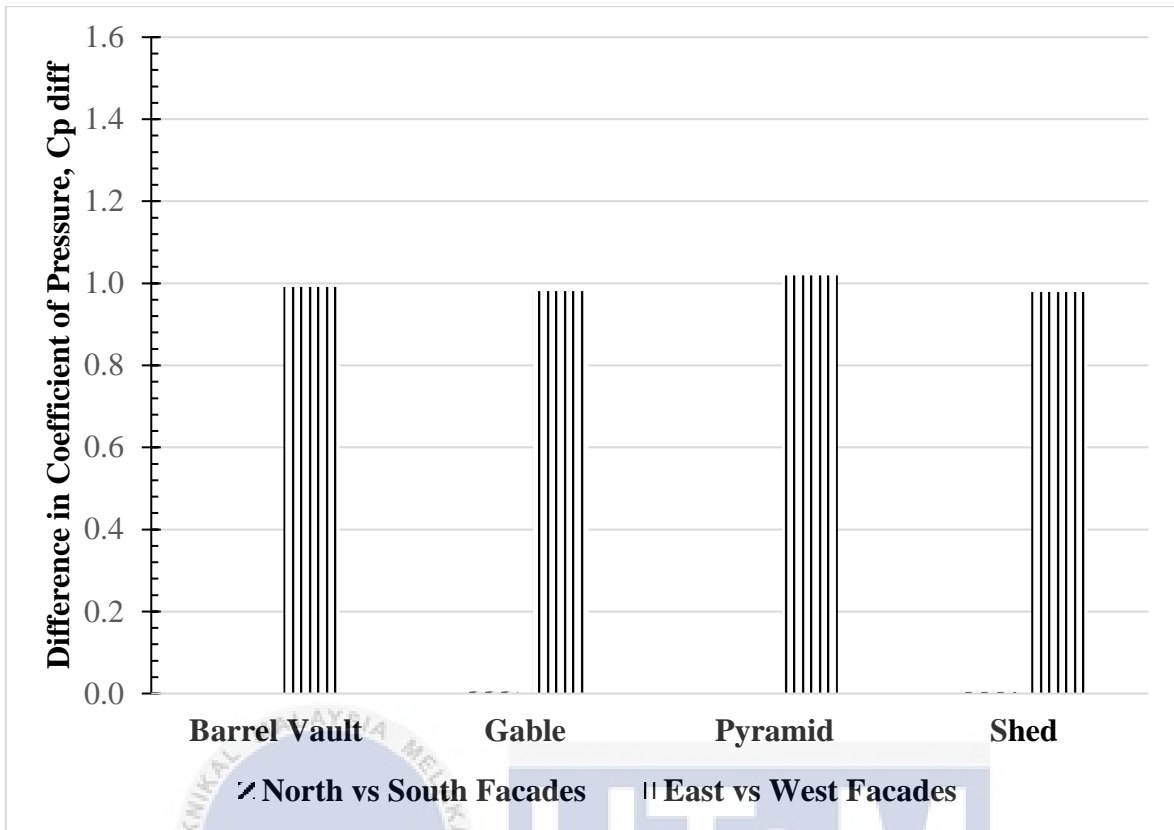


Figure D6: Difference in Wind Pressure Coefficients, C_{diff} against the Upper Floor Building Model Façades of Each Roof Shapes at the 90° Wind Approach Angle.

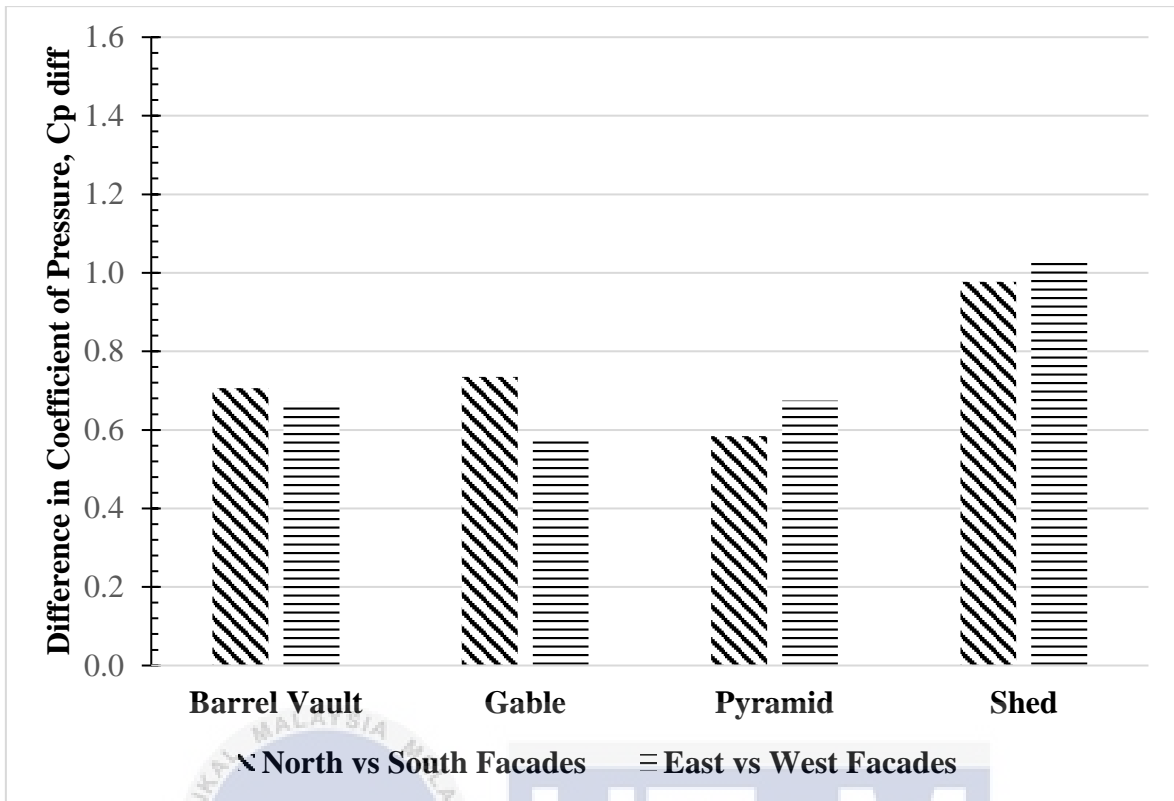


Figure D7: Difference in Wind Pressure Coefficients, C_{diff} against the Ground Floor Building Model Façades of Each Roof Shapes at the 135° Wind Approach Angle.

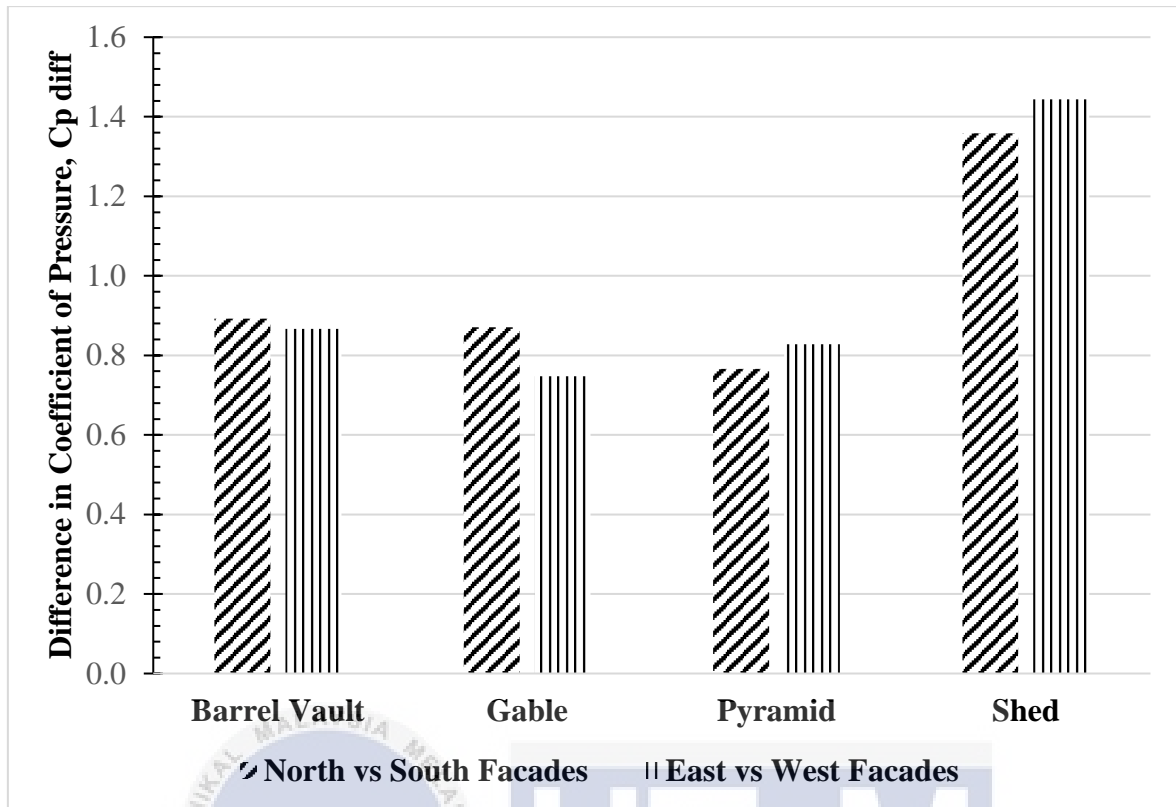


Figure D8: Difference in Wind Pressure Coefficients, C_{diff} against the Upper Floor Building Model Façades of Each Roof Shapes at the 135° Wind Approach Angle.

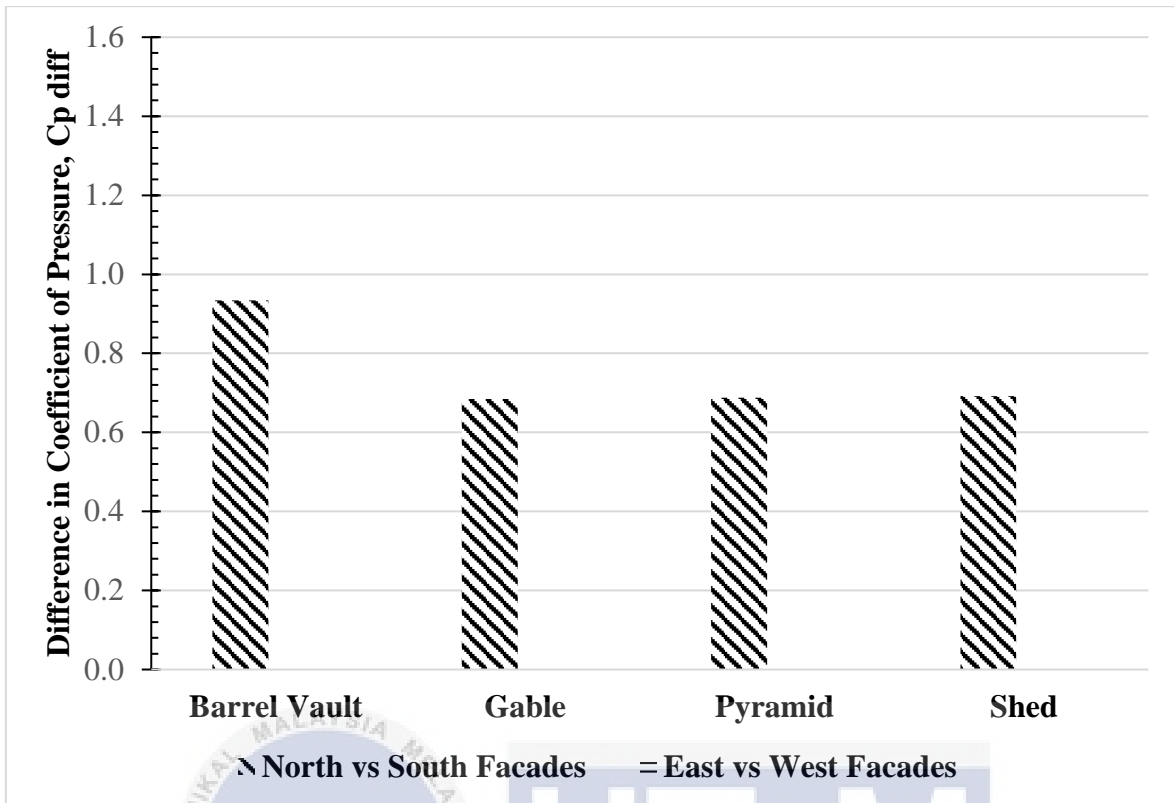


Figure D9: Difference in Wind Pressure Coefficients, C_{diff} against the Ground Floor Building Model Façades of Each Roof Shapes at the 180° Wind Approach Angle.

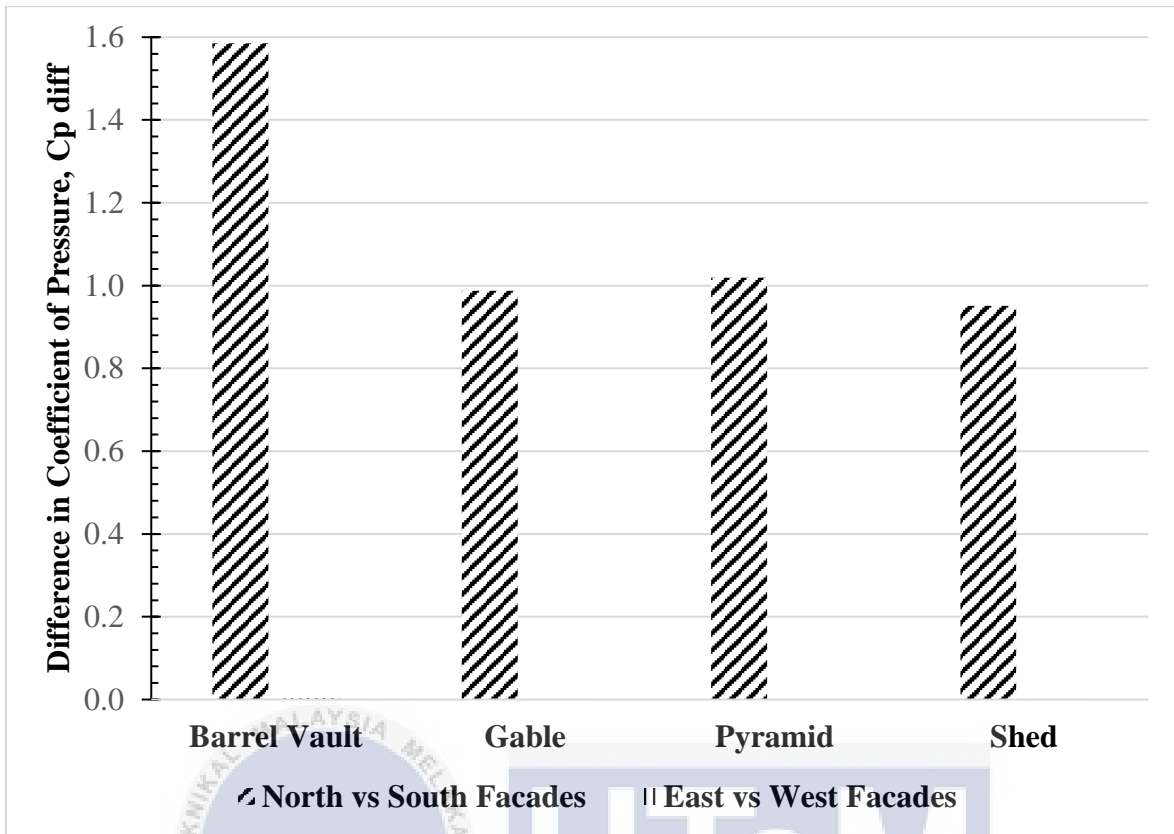


Figure D10: Difference in Wind Pressure Coefficients, C_{diff} against the Upper Floor Building Model Façades of Each Roof Shapes at the 180° Wind Approach Angle.

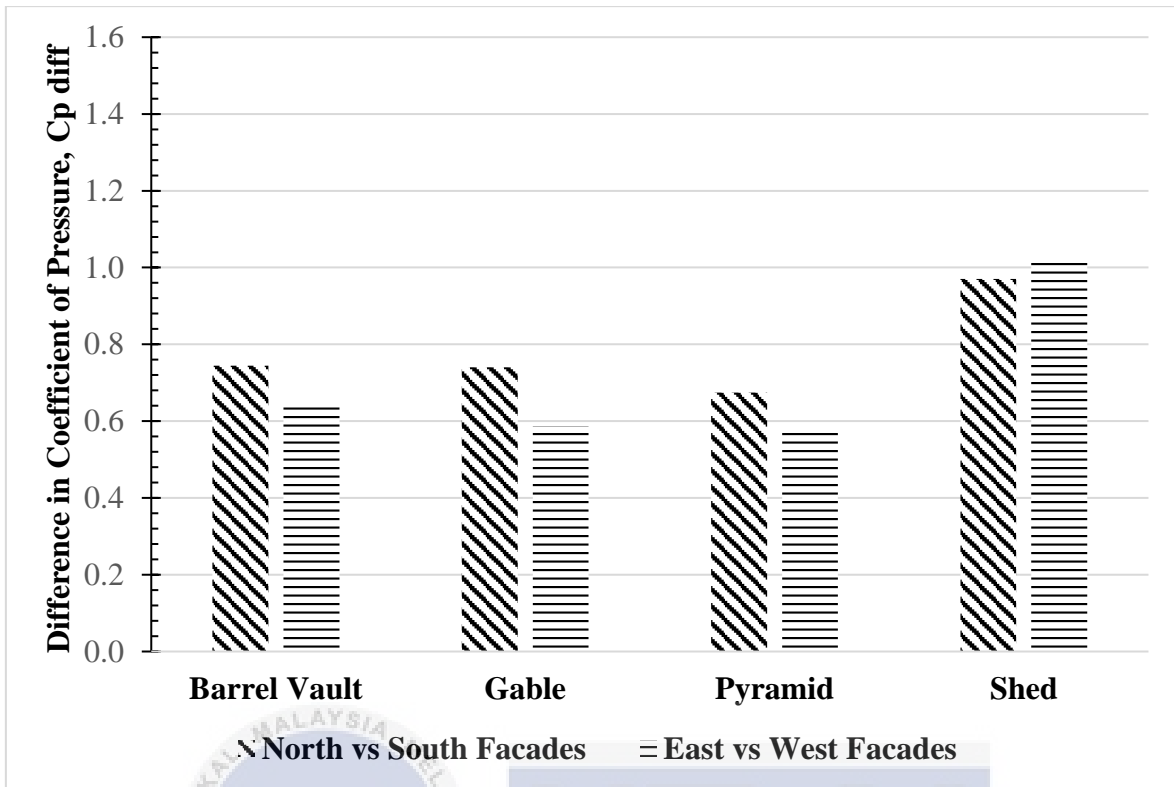


Figure D11: Difference in Wind Pressure Coefficients, C_{diff} against the Ground Floor Building Model Façades of Each Roof Shapes at the 225° Wind Approach Angle.

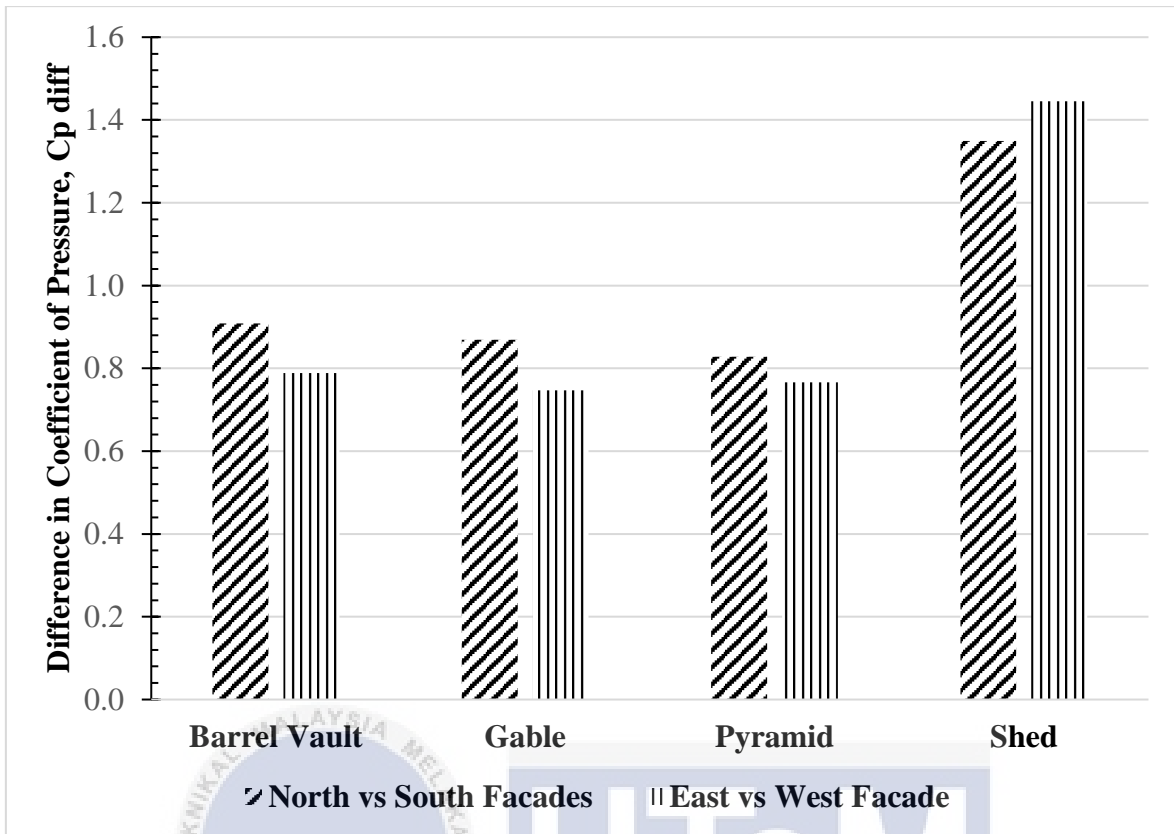


Figure D12: Difference in Wind Pressure Coefficients, C_{diff} against the Upper Floor Building Model Façades of Each Roof Shapes at the 225° Wind Approach Angle.

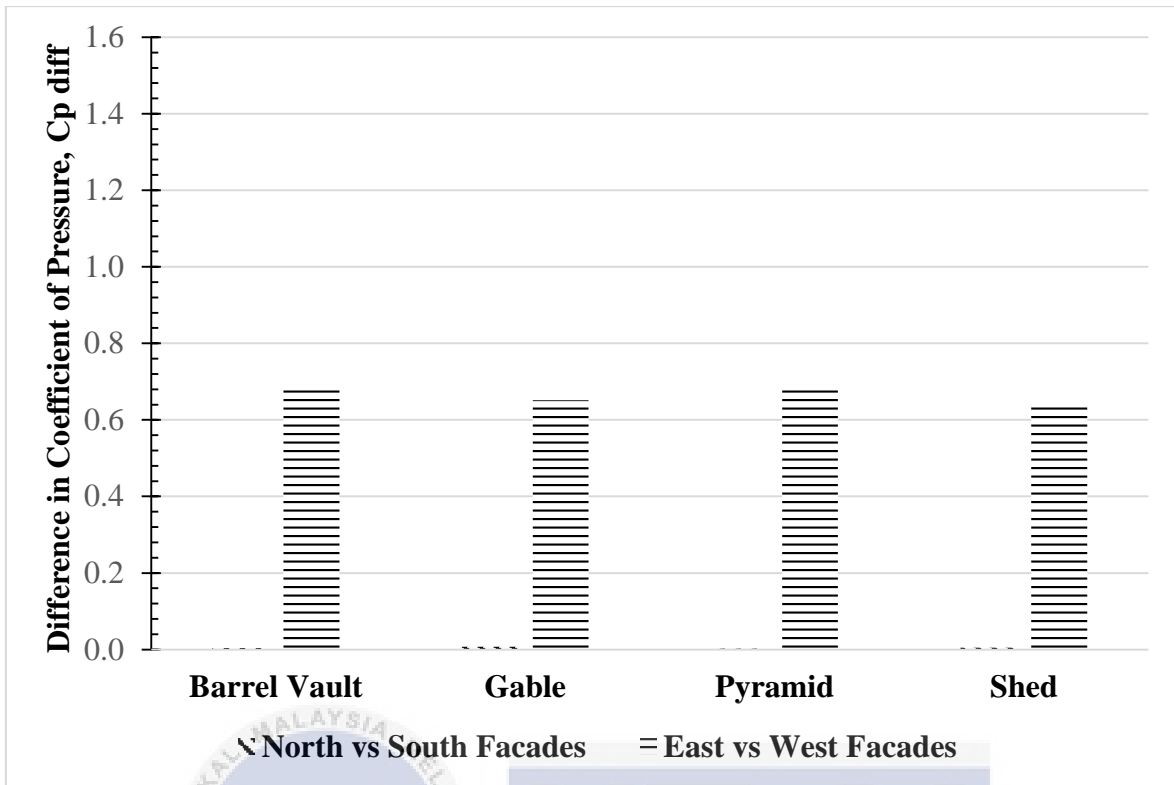


Figure D13: Difference in Wind Pressure Coefficients, C_{diff} against the Ground Floor Building Model Façades of Each Roof Shapes at the 270° Wind Approach Angle.

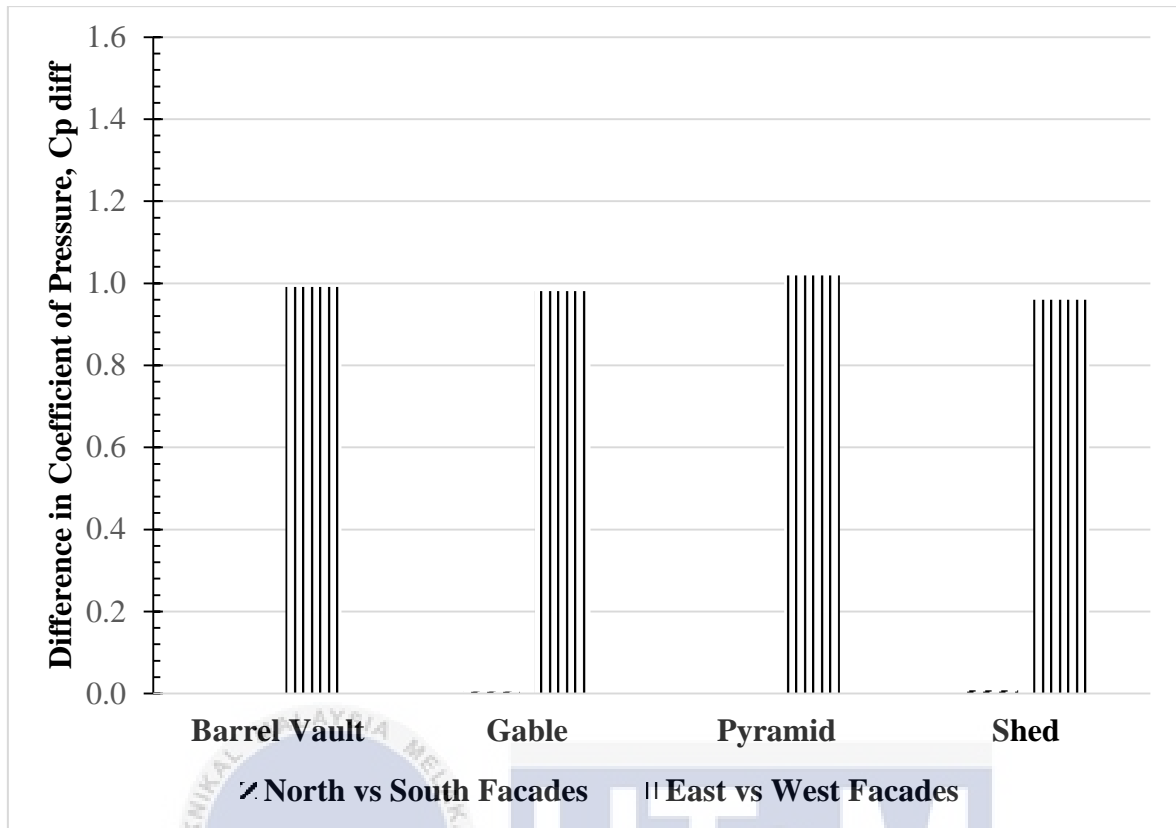


Figure D14: Difference in Wind Pressure Coefficients, C_{diff} against the Upper Floor Building Model Façades of Each Roof Shapes at the 270° Wind Approach Angle.

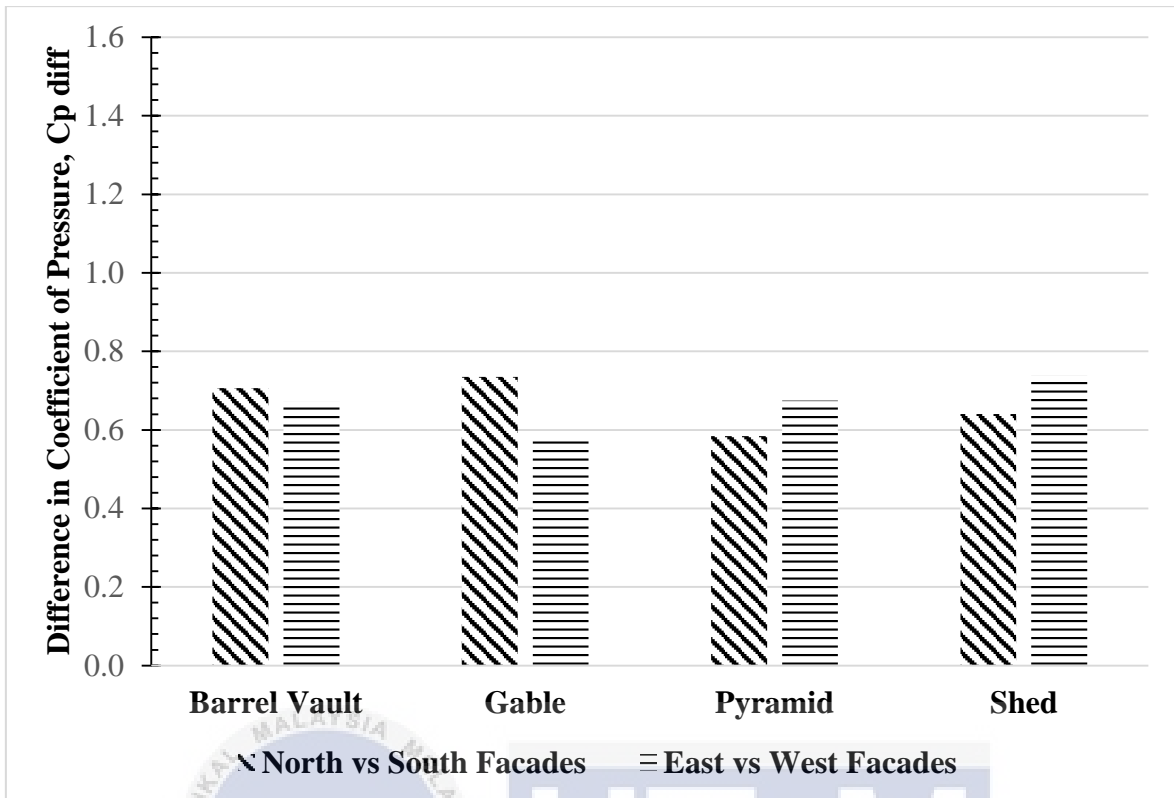


Figure D15: Difference in Wind Pressure Coefficients, C_{diff} against the Ground Floor Building Model Façades of Each Roof Shapes at the 315° Wind Approach Angle.

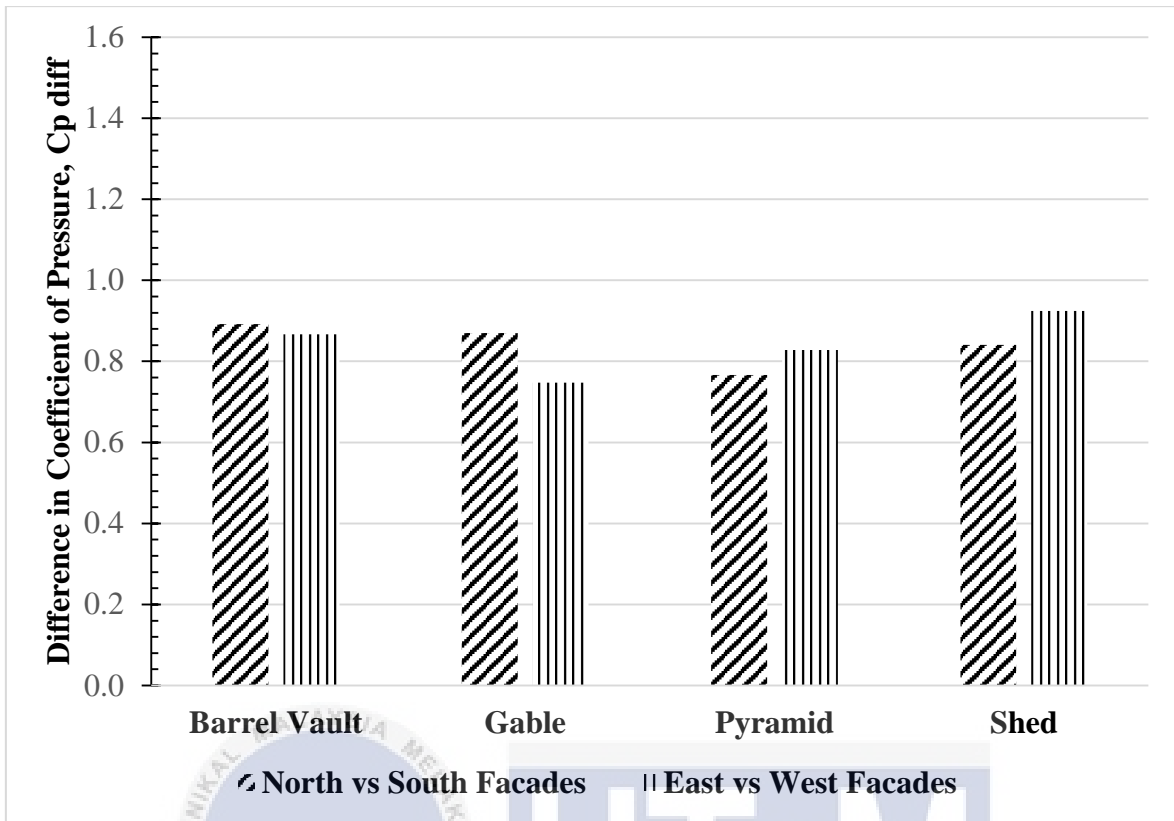


Figure D16: Difference in Wind Pressure Coefficients, C_{diff} against the Upper Floor Building Model Façades of Each Roof Shapes at the 315° Wind Approach Angle.

Table D1: Wind Pressure Data for Each Roof Shapes

0° Wind Approach Angle					
Facade	Pressure (Pa)	Barrel Vault	Gable	Pyramid	Shed
North Ground	Min	-6.6099	-2.6901	-2.7856	-2.8982
	Max	3.1408	2.8524	2.8977	2.9249
	Average	1.8849	1.7591	1.7897	1.8891
North Upper	Min	-7.4777	-3.9290	-4.6673	-2.8495
	Max	5.3388	3.4631	3.6479	4.0008
	Average	3.7286	2.7922	2.9450	3.0410
East Ground	Min	-9.6725	-1.9986	-3.8082	-4.1097
	Max	-0.9508	-1.3356	-1.3860	-1.2711
	Average	-2.6343	-2.2151	-2.2564	-2.2987
East Upper	Min	-10.7834	-6.0804	-6.5713	-4.9410
	Max	-0.7712	-1.2190	-1.2367	-1.4249
	Average	-2.5499	-2.4167	-2.4376	-2.4079
South Ground	Min	-3.7144	-1.6734	-1.5647	-1.6933
	Max	-1.4116	-0.8316	-0.8191	-0.6714
	Average	-1.9818	-1.0744	-1.0578	-0.9123
South Upper	Min	-5.0958	-1.9766	-1.8508	-2.1808
	Max	-1.8359	-1.0140	-0.9924	-0.9626
	Average	-2.8356	-1.2962	-1.2735	-1.2741
West Ground	Min	-9.6954	-3.8960	-3.7966	-4.0248
	Max	-0.9734	-1.3917	-1.4017	-1.2496
	Average	-2.6272	-2.2196	-2.2475	-2.3038

West Upper	Min	-10.8802	-6.1009	-6.5656	-4.8095
	Max	-0.7546	-1.2231	-1.2353	-1.4299
	Average	-2.5377	-2.4226	-2.4334	-2.3994
45° Wind Approach Angle					
Facade	Pressure (Pa)	Barrel Vault	Gable	Pyramid	Shed
North Ground	Min	-1.9236	-1.6803	-1.5685	-3.7955
	Max	3.0972	3.1431	3.1389	3.8202
	Average	1.0977	1.1478	1.1922	1.0468
North Upper	Min	-1.9616	-2.1164	-2.1544	-4.4097
	Max	3.8383	3.7730	4.0031	5.0085
	Average	1.4474	1.4514	1.6325	1.9730
East Ground	Min	-2.1908	-1.8995	-1.8039	-5.2336
	Max	-1.4290	-1.0929	-0.7785	-1.2987
	Average	-1.5640	-1.3660	-1.2941	-2.7911
East Upper	Min	-2.2893	-2.1617	-2.3625	-6.5072
	Max	-1.5700	-1.2763	-1.0719	-2.0043
	Average	-1.6855	-1.5539	-1.5881	-3.5494
South Ground	Min	-2.6415	-2.3763	-2.0540	-5.2128
	Max	-1.7685	-1.3375	-0.9031	-1.2987
	Average	-1.9844	-1.9178	-1.6017	-2.8422
South Upper	Min	-3.2320	-3.0217	-2.4466	-6.3546
	Max	-1.9014	-1.6454	-1.2001	-2.0043
	Average	-2.3146	-2.1486	-1.7955	-3.6751

West Ground	Min	-2.3672	-2.0802	-1.7878	-3.7891
	Max	3.0972	3.1431	3.1389	3.8202
	Average	1.0977	1.0604	1.1260	0.8860
West Upper	Min	-2.6602	-2.5434	-2.4466	-4.1976
	Max	4.0147	3.7730	4.0031	5.0085
	Average	1.5793	1.5394	1.5837	1.6143
90° Wind Approach Angle					
Facade	Pressure (Pa)	Barrel Vault	Gable	Pyramid	Shed
North Ground	Min	-3.9077	-3.3841	2.9450	-3.8888
	Max	-1.5023	-1.3083	-3.8082	-1.1689
	Average	-2.1684	-2.0685	-1.3860	-2.0705
North Upper	Min	-6.1235	-5.8184	-2.2564	-5.0060
	Max	-1.1826	-1.0471	-6.5713	-1.1536
	Average	-2.4343	-2.2223	-1.2367	-2.2218
East Ground	Min	-1.9441	-1.6435	-2.4376	-1.5386
	Max	-0.7046	-0.6273	-1.5647	-0.6376
	Average	-0.9376	-0.8605	-0.8191	-0.8619
East Upper	Min	-1.5780	-1.4573	-1.0578	-1.5532
	Max	-0.9791	-0.9077	-1.8508	-0.9048
	Average	-1.2093	-1.1140	-0.9924	-1.1067
South Ground	Min	-3.8234	-3.6542	-1.2735	-3.5715
	Max	-1.4450	-1.3392	-3.7966	-1.3309
	Average	-2.1516	-2.0387	-1.4017	-2.0547
	Min	-6.2027	-5.8773	-2.2475	-5.7908

South Upper	Max	-1.1834	-1.0555	-6.5656	-1.0204
	Average	-2.4305	-2.2429	-1.2353	-2.2396
West Ground	Min	-2.9845	-2.4188	-2.7856	-2.7640
	Max	2.9166	2.8655	2.8977	2.8794
	Average	1.9142	1.8367	1.7897	1.8295
West Upper	Min	-3.5882	-3.5734	-4.6673	-3.1208
	Max	3.7486	3.7268	3.6479	3.7000
	Average	2.8945	2.9480	2.9450	2.9454
135° Wind Approach Angle					
Facade	Pressure (Pa)	Barrel Vault	Gable	Pyramid	Shed
North Ground	Min	-2.7165	-2.3574	-1.8039	-5.7510
	Max	-0.9382	-1.4175	-0.7785	-1.3282
	Average	-1.8634	-1.9230	-1.2941	-3.0603
North Upper	Min	-3.4261	-3.0160	-2.3625	-7.2022
	Max	-1.4327	-1.6847	-1.0719	-1.7958
	Average	-2.2620	-2.1411	-1.5881	-3.6823
East Ground	Min	-2.5351	-1.8766	-2.0540	-5.8661
	Max	-0.9382	-1.1156	-0.9031	-1.3282
	Average	-1.6951	-1.3815	-1.6017	-3.1404
East Upper	Min	-2.8387	-2.1885	-2.4466	-8.7613
	Max	-1.3654	-1.2740	-1.2001	-1.7958
	Average	-1.9896	-1.5510	-1.7955	-3.7930

South Ground	Min	-2.1195	-1.7155	-1.7878	-4.2183
	Max	3.0729	3.0597	3.1389	4.0771
	Average	1.0627	1.1211	1.1260	0.9851
South Upper	Min	-2.3249	-2.1355	-2.4466	-4.8039
	Max	3.8668	3.8401	4.0031	5.1769
	Average	1.4316	1.4626	1.5837	1.9409
West Ground	Min	-2.2687	-2.1081	-1.5685	-4.1867
	Max	3.0729	3.0597	3.1389	4.0771
	Average	1.0851	1.0171	1.1922	1.1283
West Upper	Min	-2.7801	-2.6283	-2.1544	-4.8711
	Max	3.9683	3.8401	4.0031	5.1769
	Average	1.5987	1.5443	1.6325	2.1839
180° Wind Approach Angle					
Facade	Pressure (Pa)	Barrel Vault	Gable	Pyramid	Shed
North Ground	Min	-3.7144	-1.6734	-1.5647	-1.7324
	Max	-1.4116	-0.8316	-0.8191	-0.8732
	Average	-1.9818	-1.0744	-1.0578	-1.1242
North Upper	Min	-5.0958	-1.9766	-1.8508	-1.7026
	Max	-1.8359	-1.0140	-0.9924	-1.0283
	Average	-2.8356	-1.2962	-1.2735	-1.3025
East Ground	Min	-9.6954	-3.8960	-3.7966	-4.3161
	Max	-0.9734	-1.3917	-1.4017	-1.3480
	Average	-2.6272	-2.2196	-2.2475	-2.2135

East Upper	Min	-10.8802	-6.1009	-6.5656	-5.5842
	Max	-0.7546	-1.2231	-1.2353	-1.1987
	Average	-2.5377	-2.4226	-2.4334	-2.3926
South Ground	Min	-6.6099	-2.6901	-2.7856	-2.8904
	Max	3.1408	2.8524	2.8977	2.7999
	Average	1.8849	1.7591	1.7897	1.7400
South Upper	Min	-7.4777	-3.9290	-4.6673	-5.2527
	Max	5.3388	3.4631	3.6479	3.3165
	Average	3.7286	2.7922	2.9450	2.6356
West Ground	Min	-9.6725	-1.9986	-3.8082	-4.2741
	Max	-0.9508	-1.3356	-1.3860	-1.3513
	Average	-2.6343	-2.2151	-2.2564	-2.2204
West Upper	Min	-10.7834	-6.0804	-6.5713	-5.6347
	Max	-0.7712	-1.2190	-1.2367	-1.1984
	Average	-2.5499	-2.4167	-2.4376	-2.3999
225° Wind Approach Angle					
Facade	Pressure (Pa)	Barrel Vault	Gable	Pyramid	Shed
North Ground	Min	-2.6415	-2.3763	-2.0540	-5.7170
	Max	-1.7685	-1.3375	-0.9031	-1.3145
	Average	-1.9844	-1.9178	-1.6017	-3.0468
North Upper	Min	-3.2320	-3.0217	-2.4466	-7.2488
	Max	-1.9014	-1.6454	-1.2001	-1.6917
	Average	-2.3146	-2.1486	-1.7955	-3.6818

East Ground	Min	-2.3672	-2.0802	-1.7878	-4.1263
	Max	3.0972	3.1431	3.1389	4.0929
	Average	1.0977	1.0604	1.1260	1.0771
East Upper	Min	-2.6602	-2.5434	-2.4466	-4.9937
	Max	4.0147	3.7730	4.0031	5.2496
	Average	1.5793	1.5394	1.5837	2.1507
South Ground	Min	-1.9236	-1.6803	-1.5685	-4.4213
	Max	3.0972	3.1431	3.1389	4.0929
	Average	1.0977	1.1478	1.1922	0.9712
South Upper	Min	-1.9616	-2.1164	-2.1544	-5.5368
	Max	3.8383	3.7730	4.0031	5.2496
	Average	1.4474	1.4514	1.6325	1.9042
West Ground	Min	-2.1908	-1.8995	-1.8039	-6.0146
	Max	-1.4290	-1.0929	-0.7785	-1.3145
	Average	-1.5640	-1.3660	-1.2941	-3.1616
West Upper	Min	-2.2893	-2.1617	-2.3625	-8.6213
	Max	-1.5700	-1.2763	-1.0719	-1.6917
	Average	-1.6855	-1.5539	-1.5881	-3.8339
270° Wind Approach Angle					
Facade	Pressure (Pa)	Barrel Vault	Gable	Pyramid	Shed
North Ground	Min	-3.8234	-3.6542	-3.7966	-4.6241
	Max	-1.4450	-1.3392	-1.4017	-1.2055
	Average	-2.1516	-2.0387	-2.2475	-2.0806

North Upper	Min	-6.2027	-5.8773	-6.5656	-6.7265
	Max	-1.1834	-1.0555	-1.2353	-1.1035
	Average	-2.4305	-2.2429	-2.4334	-2.3309
East Ground	Min	-2.9845	-2.4188	-2.7856	-3.7278
	Max	2.9166	2.8655	2.8977	2.8076
	Average	1.9142	1.8367	1.7897	1.7772
East Upper	Min	-3.5882	-3.5734	-4.6673	-4.9224
	Max	3.7486	3.7268	3.6479	3.7011
	Average	2.8945	2.9480	2.9450	2.8633
South Ground	Min	-3.9077	-3.3841	-3.8082	-4.9337
	Max	-1.5023	-1.3083	-1.3860	-1.2708
	Average	-2.1684	-2.0685	-2.2564	-2.0996
South Upper	Min	-6.1235	-5.8184	-6.5713	-7.2719
	Max	-1.1826	-1.0471	-1.2367	-0.9533
	Average	-2.4343	-2.2223	-2.4376	-2.3648
West Ground	Min	-1.9441	-1.6435	-1.5647	-1.7341
	Max	-0.7046	-0.6273	-0.8191	-0.6378
	Average	-0.9376	-0.8605	-1.0578	-0.8700
West Upper	Min	-1.5780	-1.4573	-1.8508	-1.9920
	Max	-0.9791	-0.9077	-0.9924	-0.8957
	Average	-1.2093	-1.1140	-1.2735	-1.1108

315° Wind Approach Angle					
Facade	Pressure (Pa)	Barrel Vault	Gable	Pyramid	Shed
North Ground	Min	-2.1195	-1.7155	-1.7878	-2.3481
	Max	3.0729	3.0597	3.1389	3.1881
	Average	1.0627	1.1211	1.1260	1.1084
North Upper	Min	-2.3249	-2.1355	-2.4466	-2.6276
	Max	3.8668	3.8401	4.0031	4.1691
	Average	1.4316	1.4626	1.5837	1.6519
East Ground	Min	-2.2687	-2.1081	-1.5685	-1.9407
	Max	3.0729	3.0597	3.1389	3.1881
	Average	1.0851	1.0171	1.1922	1.0741
East Upper	Min	-2.7801	-2.6283	-2.1544	-2.2011
	Max	3.9683	3.8401	4.0031	4.1691
	Average	1.5987	1.5443	1.6325	1.4899
South Ground	Min	-2.7165	-2.3574	-1.8039	-2.2863
	Max	-0.9382	-1.4175	-0.7785	-0.7574
	Average	-1.8634	-1.9230	-1.2941	-1.5424
South Upper	Min	-3.4261	-3.0160	-2.3625	-2.9431
	Max	-1.4327	-1.6847	-1.0719	-1.0253
	Average	-2.2620	-2.1411	-1.5881	-1.8300
West Ground	Min	-2.5351	-1.8766	-2.0540	-2.8015
	Max	-0.9382	-1.1156	-0.9031	-0.9014
	Average	-1.6951	-1.3815	-1.6017	-1.9780

West Upper	Min	-2.8387	-2.1885	-2.4466	-3.2894
	Max	-1.3654	-1.2740	-1.2001	-1.3366
	Average	-1.9896	-1.5510	-1.7955	-2.3366
Average Wind Approach Angle					
Facade	Pressure (Pa)	Barrel Vault	Gable	Pyramid	Shed
North Ground	Min	-3.4321	-2.4414	-1.5520	-3.8444
	Max	0.2807	0.3526	0.1831	0.5054
	Average	-0.7630	-0.6243	-0.4349	-0.9173
North Upper	Min	-4.4805	-3.4864	-3.0938	-4.7216
	Max	0.6885	0.5787	0.0729	0.8007
	Average	-0.7087	-0.5431	-0.2708	-0.8192
East Ground	Min	-4.2073	-2.2402	-2.5053	-3.8574
	Max	0.5113	0.4382	0.3927	0.5256
	Average	-0.6702	-0.5161	-0.5139	-0.9222
East Upper	Min	-4.6748	-3.3417	-3.5340	-4.9330
	Max	0.7864	0.6800	0.6324	0.7239
	Average	-0.4874	-0.3783	-0.3857	-0.8432
South Ground	Min	-3.4321	-2.4414	-2.0808	-3.6535
	Max	0.2807	0.3526	0.1865	0.7051
	Average	-0.7630	-0.6243	-0.4380	-0.7194
South Upper	Min	-4.4805	-3.4864	-3.0934	-5.0168
	Max	0.6885	0.5787	0.0734	0.9721
	Average	-0.7087	-0.5431	-0.2711	-0.6129

West Ground	Min	-4.2073	-2.2402	-2.3962	-3.6986
	Max	0.5113	0.4382	0.4859	0.6653
	Average	-0.6702	-0.5161	-0.5437	-0.8363
West Upper	Min	-4.6748	-3.3417	-3.6331	-4.5671
	Max	0.7864	0.6800	0.7397	0.9166
	Average	-0.4874	-0.3783	-0.4209	-0.6671



Table D2: Coefficient of Wind Pressure Data for Each Roof Shapes

0° Wind Approach Angle					
Facade	C _p	Barrel Vault	Gable	Pyramid	Shed
North Ground	Min	-2.5964	-1.6497	-1.6728	-1.7000
	Max	-0.2414	-0.3111	-0.3002	-0.2936
	Average	-0.5448	-0.5751	-0.5678	-0.5438
North Upper	Min	-2.8060	-1.9489	-2.1272	-1.6882
	Max	0.2894	-0.1636	-0.1190	-0.0337
	Average	-0.0995	-0.3256	-0.2887	-0.2655
East Ground	Min	-3.3361	-1.4827	-1.9197	-1.9926
	Max	-1.2296	-1.3226	-1.3347	-1.3070
	Average	-1.6362	-1.5350	-1.5450	-1.5552
East Upper	Min	-3.6044	-2.4685	-2.5871	-2.1933
	Max	-1.1863	-1.2944	-1.2987	-1.3441
	Average	-1.6158	-1.5837	-1.5887	-1.5815
South Ground	Min	-1.8971	-1.4042	-1.3779	-1.4090
	Max	-1.3409	-1.2008	-1.1978	-1.1622
	Average	-1.4786	-1.2595	-1.2555	-1.2203
South Upper	Min	-2.2307	-1.4774	-1.4470	-1.5267
	Max	-1.4434	-1.2449	-1.2397	-1.2325
	Average	-1.6848	-1.3131	-1.3076	-1.3077
West Ground	Min	-3.3416	-1.9409	-1.9169	-1.9721
	Max	-1.2351	-1.3361	-1.3385	-1.3018
	Average	-1.6345	-1.5361	-1.5428	-1.5564

West Upper	Min	-3.6278	-2.4735	-2.5857	-2.1616
	Max	-1.1822	-1.2954	-1.2983	-1.3453
	Average	-1.6129	-1.5851	-1.5877	-1.5795
45° Wind Approach Angle					
Facade	C_p	Barrel Vault	Gable	Pyramid	Shed
North Ground	Min	-1.4646	-1.4058	-1.3788	-1.9167
	Max	-0.2520	-0.2409	-0.2419	-0.0774
	Average	-0.7349	-0.7228	-0.7121	-0.7472
North Upper	Min	-1.4738	-1.5111	-1.5203	-2.0650
	Max	-0.0730	-0.0888	-0.0332	0.2096
	Average	-0.6504	-0.6495	-0.6057	-0.5235
East Ground	Min	-1.5291	-1.4588	-1.4357	-2.2640
	Max	-1.3451	-1.2640	-1.1880	-1.3137
	Average	-1.3777	-1.3299	-1.3125	-1.6741
East Upper	Min	-1.5529	-1.5221	-1.5706	-2.5716
	Max	-1.3792	-1.3082	-1.2589	-1.4841
	Average	-1.4071	-1.3753	-1.3836	-1.8572
South Ground	Min	-1.6380	-1.5739	-1.4961	-2.2590
	Max	-1.4271	-1.3230	-1.2181	-1.3137
	Average	-1.4793	-1.4632	-1.3868	-1.6864
South Upper	Min	-1.7806	-1.7298	-1.5909	-2.5347
	Max	-1.4592	-1.3974	-1.2898	-1.4841
	Average	-1.5590	-1.5189	-1.4336	-1.8876

West Ground	Min	-1.5717	-1.5024	-1.4318	-1.9151
	Max	-0.2520	-0.2409	-0.2419	-0.0774
	Average	-0.7349	-0.7439	-0.7281	-0.7860
West Upper	Min	-1.6425	-1.6143	-1.5909	-2.0138
	Max	-0.0304	-0.0888	-0.0332	0.2096
	Average	-0.6186	-0.6282	-0.6175	-0.6101
90° Wind Approach Angle					
Facade	C_p	Barrel Vault	Gable	Pyramid	Shed
North Ground	Min	-1.9438	-1.8173	-1.9197	-1.9392
	Max	-1.3628	-1.3160	-1.3347	-1.2823
	Average	-1.5237	-1.4996	-1.5450	-1.5001
North Upper	Min	-2.4789	-2.4052	-2.5871	-2.2090
	Max	-1.2856	-1.2529	-1.2987	-1.2786
	Average	-1.5879	-1.5367	-1.5887	-1.5366
East Ground	Min	-1.4695	-1.3969	-1.3779	-1.3716
	Max	-1.1702	-1.1515	-1.1978	-1.1540
	Average	-1.2264	-1.2078	-1.2555	-1.2082
East Upper	Min	-1.3811	-1.3520	-1.4470	-1.3751
	Max	-1.2365	-1.2192	-1.2397	-1.2185
	Average	-1.2921	-1.2690	-1.3076	-1.2673
South Ground	Min	-1.9234	-1.8826	-1.9169	-1.8626
	Max	-1.3490	-1.3234	-1.3385	-1.3214
	Average	-1.5196	-1.4924	-1.5428	-1.4962

South Upper	Min	-2.4981	-2.4195	-2.5857	-2.3986
	Max	-1.2858	-1.2549	-1.2983	-1.2464
	Average	-1.5870	-1.5417	-1.5877	-1.5409
West Ground	Min	-1.7208	-1.5842	-1.6728	-1.6676
	Max	-0.2956	-0.3079	-0.3002	-0.3046
	Average	-0.5377	-0.5564	-0.5678	-0.5581
West Upper	Min	-1.8666	-1.8630	-2.1272	-1.7537
	Max	-0.0947	-0.0999	-0.1190	-0.1064
	Average	-0.3009	-0.2880	-0.2887	-0.2886
135° Wind Approach Angle					
Facade	C_p	Barrel Vault	Gable	Pyramid	Shed
North Ground	Min	-1.6561	-1.5694	-1.4357	-2.3890
	Max	-1.2266	-1.3423	-1.1880	-1.3208
	Average	-1.4500	-1.4644	-1.3125	-1.7391
North Upper	Min	-1.8275	-1.7284	-1.5706	-2.7395
	Max	-1.3460	-1.4069	-1.2589	-1.4337
	Average	-1.5463	-1.5171	-1.3836	-1.8893
East Ground	Min	-1.6123	-1.4532	-1.4961	-2.4168
	Max	-1.2266	-1.2694	-1.2181	-1.3208
	Average	-1.4094	-1.3337	-1.3868	-1.7585
East Upper	Min	-1.6856	-1.5286	-1.5909	-3.1160
	Max	-1.3298	-1.3077	-1.2898	-1.4337
	Average	-1.4805	-1.3746	-1.4336	-1.9161

South Ground	Min	-1.5119	-1.4143	-1.4318	-2.0188
	Max	-0.2578	-0.2610	-0.2419	-0.0153
	Average	-0.7433	-0.7292	-0.7281	-0.7621
South Upper	Min	-1.5615	-1.5158	-1.5909	-2.1602
	Max	-0.0661	-0.0726	-0.0332	0.2503
	Average	-0.6542	-0.6468	-0.6175	-0.5312
West Ground	Min	-1.5479	-1.5091	-1.3788	-2.0112
	Max	-0.2578	-0.2610	-0.2419	-0.0153
	Average	-0.7379	-0.7544	-0.7121	-0.7275
West Upper	Min	-1.6714	-1.6348	-1.5203	-2.1765
	Max	-0.0416	-0.0726	-0.0332	0.2503
	Average	-0.6139	-0.6270	-0.6057	-0.4726
180° Wind Approach Angle					
Facade	C_p	Barrel Vault	Gable	Pyramid	Shed
North Ground	Min	-1.8971	-1.4042	-1.3779	-1.4184
	Max	-1.3409	-1.2008	-1.1978	-1.2109
	Average	-1.4786	-1.2595	-1.2555	-1.2715
North Upper	Min	-2.2307	-1.4774	-1.4470	-1.4112
	Max	-1.4434	-1.2449	-1.2397	-1.2484
	Average	-1.6848	-1.3131	-1.3076	-1.3146
East Ground	Min	-3.3416	-1.9409	-1.9169	-2.0424
	Max	-1.2351	-1.3361	-1.3385	-1.3256
	Average	-1.6345	-1.5361	-1.5428	-1.5346

East Upper	Min	-3.6278	-2.4735	-2.5857	-2.3487
	Max	-1.1822	-1.2954	-1.2983	-1.2895
	Average	-1.6129	-1.5851	-1.5877	-1.5779
South Ground	Min	-2.5964	-1.6497	-1.6728	-1.6981
	Max	-0.2414	-0.3111	-0.3002	-0.3238
	Average	-0.5448	-0.5751	-0.5678	-0.5798
South Upper	Min	-2.8060	-1.9489	-2.1272	-2.2686
	Max	0.2894	-0.1636	-0.1190	-0.1990
	Average	-0.0995	-0.3256	-0.2887	-0.3635
West Ground	Min	-3.3361	-1.4827	-1.9197	-2.0323
	Max	-1.2296	-1.3226	-1.3347	-1.3264
	Average	-1.6362	-1.5350	-1.5450	-1.5363
West Upper	Min	-3.6044	-2.4685	-2.5871	-2.3609
	Max	-1.1863	-1.2944	-1.2987	-1.2894
	Average	-1.6158	-1.5837	-1.5887	-1.5796
225° Wind Approach Angle					
Facade	C_p	Barrel Vault	Gable	Pyramid	Shed
North Ground	Min	-1.6380	-1.5739	-1.4961	-2.3808
	Max	-1.4271	-1.3230	-1.2181	-1.3175
	Average	-1.4793	-1.4632	-1.3868	-1.7359
North Upper	Min	-1.7806	-1.7298	-1.5909	-2.7507
	Max	-1.4592	-1.3974	-1.2898	-1.4086
	Average	-1.5590	-1.5189	-1.4336	-1.8892

East Ground	Min	-1.5717	-1.5024	-1.4318	-1.9966
	Max	-0.2520	-0.2409	-0.2419	-0.0115
	Average	-0.7349	-0.7439	-0.7281	-0.7399
East Upper	Min	-1.6425	-1.6143	-1.5909	-2.2061
	Max	-0.0304	-0.0888	-0.0332	0.2679
	Average	-0.6186	-0.6282	-0.6175	-0.4806
South Ground	Min	-1.4646	-1.4058	-1.3788	-2.0678
	Max	-0.2520	-0.2409	-0.2419	-0.0115
	Average	-0.7349	-0.7228	-0.7121	-0.7654
South Upper	Min	-1.4738	-1.5111	-1.5203	-2.3372
	Max	-0.0730	-0.0888	-0.0332	0.2679
	Average	-0.6504	-0.6495	-0.6057	-0.5401
West Ground	Min	-1.5291	-1.4588	-1.4357	-2.4526
	Max	-1.3451	-1.2640	-1.1880	-1.3175
	Average	-1.3777	-1.3299	-1.3125	-1.7636
West Upper	Min	-1.5529	-1.5221	-1.5706	-3.0822
	Max	-1.3792	-1.3082	-1.2589	-1.4086
	Average	-1.4071	-1.3753	-1.3836	-1.9260
270° Wind Approach Angle					
Facade	C_p	Barrel Vault	Gable	Pyramid	Shed
North Ground	Min	-1.9234	-1.8826	-1.9169	-2.1168
	Max	-1.3490	-1.3234	-1.3385	-1.2911
	Average	-1.5196	-1.4924	-1.5428	-1.5025

North Upper	Min	-2.4981	-2.4195	-2.5857	-2.6246
	Max	-1.2858	-1.2549	-1.2983	-1.2665
	Average	-1.5870	-1.5417	-1.5877	-1.5630
East Ground	Min	-1.7208	-1.5842	-1.6728	-1.9003
	Max	-0.2956	-0.3079	-0.3002	-0.3219
	Average	-0.5377	-0.5564	-0.5678	-0.5708
East Upper	Min	-1.8666	-1.8630	-2.1272	-2.1888
	Max	-0.0947	-0.0999	-0.1190	-0.1061
	Average	-0.3009	-0.2880	-0.2887	-0.3085
South Ground	Min	-1.9438	-1.8173	-1.9197	-2.1916
	Max	-1.3628	-1.3160	-1.3347	-1.3069
	Average	-1.5237	-1.4996	-1.5450	-1.5071
South Upper	Min	-2.4789	-2.4052	-2.5871	-2.7563
	Max	-1.2856	-1.2529	-1.2987	-1.2302
	Average	-1.5879	-1.5367	-1.5887	-1.5711
West Ground	Min	-1.4695	-1.3969	-1.3779	-1.4188
	Max	-1.1702	-1.1515	-1.1978	-1.1540
	Average	-1.2264	-1.2078	-1.2555	-1.2101
West Upper	Min	-1.3811	-1.3520	-1.4470	-1.4811
	Max	-1.2365	-1.2192	-1.2397	-1.2163
	Average	-1.2921	-1.2690	-1.3076	-1.2683

315° Wind Approach Angle					
Facade	C _p	Barrel Vault	Gable	Pyramid	Shed
North Ground	Min	-1.5119	-1.4143	-1.4318	-1.5671
	Max	-0.2578	-0.2610	-0.2419	-0.2300
	Average	-0.7433	-0.7292	-0.7281	-0.7323
North Upper	Min	-1.5615	-1.5158	-1.5909	-1.6346
	Max	-0.0661	-0.0726	-0.0332	0.0069
	Average	-0.6542	-0.6468	-0.6175	-0.6010
East Ground	Min	-1.5479	-1.5091	-1.3788	-1.4687
	Max	-0.2578	-0.2610	-0.2419	-0.2300
	Average	-0.7379	-0.7544	-0.7121	-0.7406
East Upper	Min	-1.6714	-1.6348	-1.5203	-1.5316
	Max	-0.0416	-0.0726	-0.0332	0.0069
	Average	-0.6139	-0.6270	-0.6057	-0.6402
South Ground	Min	-1.6561	-1.5694	-1.4357	-1.5522
	Max	-1.2266	-1.3423	-1.1880	-1.1829
	Average	-1.4500	-1.4644	-1.3125	-1.3725
South Upper	Min	-1.8275	-1.7284	-1.5706	-1.7108
	Max	-1.3460	-1.4069	-1.2589	-1.2476
	Average	-1.5463	-1.5171	-1.3836	-1.4420
West Ground	Min	-1.6123	-1.4532	-1.4961	-1.6766
	Max	-1.2266	-1.2694	-1.2181	-1.2177
	Average	-1.4094	-1.3337	-1.3868	-1.4777

West Upper	Min	-1.6856	-1.5286	-1.5909	-1.7944
	Max	-1.3298	-1.3077	-1.2898	-1.3228
	Average	-1.4805	-1.3746	-1.4336	-1.5643
Average Wind Approach Angle					
Facade	C_p	Barrel Vault	Gable	Pyramid	Shed
North Ground	Min	-1.8289	-1.5897	-1.5787	-1.9285
	Max	-0.9322	-0.9148	-0.8826	-0.8780
	Average	-1.1843	-1.1508	-1.1313	-1.2216
North Upper	Min	-2.0821	-1.8420	-1.8775	-2.1404
	Max	-0.8337	-0.8603	-0.8214	-0.8066
	Average	-1.1711	-1.1312	-1.1016	-1.1978
East Ground	Min	-2.0161	-1.5410	-1.5787	-1.9316
	Max	-0.8765	-0.8942	-0.8826	-0.8731
	Average	-1.1618	-1.1247	-1.1313	-1.2227
East Upper	Min	-2.1290	-1.8071	-1.8775	-2.1914
	Max	-0.8101	-0.8358	-0.8214	-0.8252
	Average	-1.1177	-1.0914	-1.1016	-1.2037
South Ground	Min	-1.8289	-1.5897	-1.5787	-1.8824
	Max	-0.9322	-0.9148	-0.8826	-0.8297
	Average	-1.1843	-1.1508	-1.1313	-1.1737
South Upper	Min	-2.0821	-1.8420	-1.8775	-2.2116
	Max	-0.8337	-0.8603	-0.8214	-0.7652
	Average	-1.1711	-1.1312	-1.1016	-1.1480

West Ground	Min	-2.0161	-1.5410	-1.5787	-1.8933
	Max	-0.8765	-0.8942	-0.8826	-0.8393
	Average	-1.1618	-1.1247	-1.1313	-1.2020
West Upper	Min	-2.1290	-1.8071	-1.8775	-2.1030
	Max	-0.8101	-0.8358	-0.8214	-0.7786
	Average	-1.1177	-1.0914	-1.1016	-1.1611

